Investigation of Potential in-situ Polymerization Reactions for use in Lithium-ion Batteries

by

Tafara Dube

A dissertation presented to Nelson Mandela University in fulfilment of the requirement for the degree of

Master of Science

in

Chemistry (Focused on Physical and Electrochemistry)

Supervisors

Professor Ernst Ferg
Dr Xandri van Niekerk

Gqeberha (Port Elizabeth), Eastern Cape, South Africa, 2024

Author's Declaration

I, Tafara Alfred Dube, In accordance with Rule G5.6.3, hereby declare that the contents of this dissertation present my own work, and it has not been previously submitted for assessments to another university or for another qualification. The resources used have been indicated and acknowledged by means of references. I understand that my dissertation may be made electronically available to the public.

Tafara Alfred Dube

Official Use:

In accordance with Rule G5.11.4, I hereby declare that the above-mentioned treatise/ dissertation/ thesis is my own work and that it has not previously been submitted for assessment to another University or for another qualification. However, material from publications by the student may be embodied in a treatise/dissertation/ thesis

Table of Contents

Abstract

With the rise in popularity of electric vehicles and portable electronic devices, having a reliable, lightweight, and long-lasting battery is crucial. This has led to the mass commercialisation of lithium-ion batteries (LIB's) because they offer several advantages over other battery technologies. Over the years, one of the concerns was with the ease with which the batteries can burn or explode when subjected to certain extreme conditions. In order to build trust in these products and to expand the technology into more diverse applications, safety aspects of the batteries has become of widespread concern resulting in a key area of research. One aspect of improving the safety is by reducing the flammability of the battery by the addition of certain chemicals that stop or suppress the thermal runaway effect. However, this in-turn reduces the battery's capacity and life-cycle performance. Researchers have used the idea of encapsulating these chemicals thereby physically separating them within the lithium-ion battery (LIB) electrolyte system with a minimum effect on performance. This research aims to explore use of R-diols and R-amines as additives that upon a thermal trigger would react with the lithium-ion battery electrolyte to stop the effect of the thermal runaway by forming carbamate derivatives which are gel-like or form solid aggregates. The R-diols or R-amines can react with electrolyte at higher temperatures with the lithium-hexafluorophosphate acting as a catalyst. This change in the physical state of the electrolyte increases the resistance inside the battery which then hinders ion movement and forms a physical barrier to reduce the effect of short circuiting when the separator or other components are damaged due to higher temperatures.

Graphical abstract.

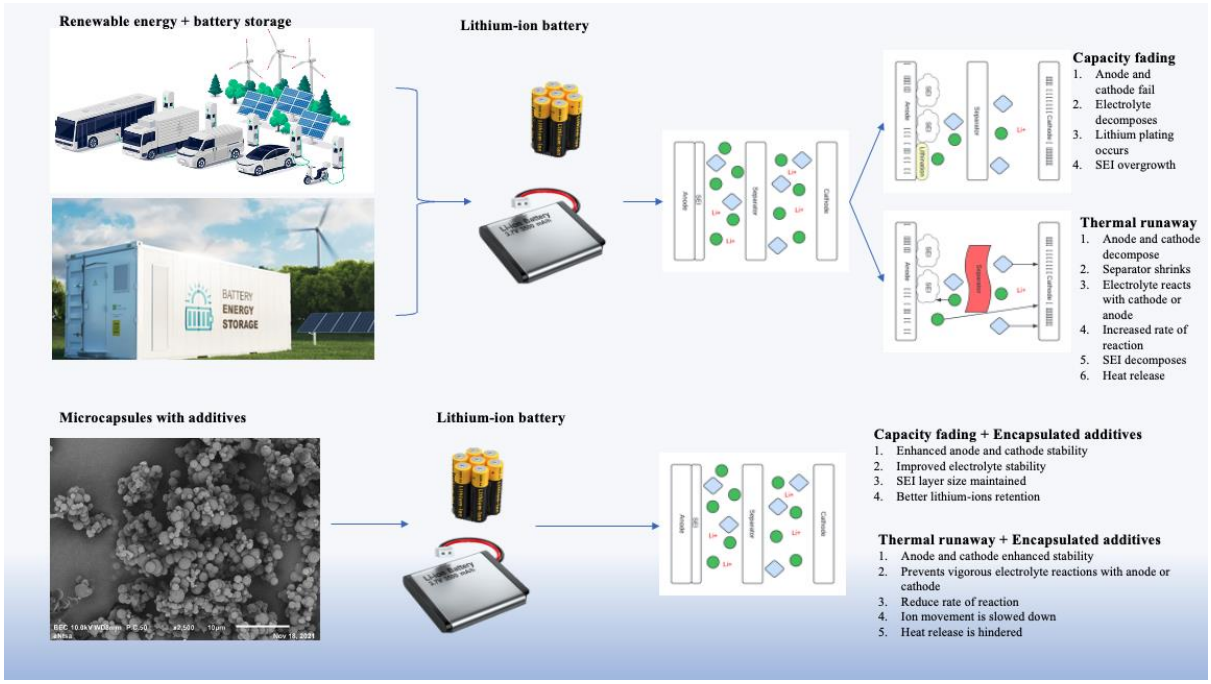

Acknowledgements

I extend my heartfelt gratitude to the individuals and organizations listed below, as this project would not have come to fruition without their invaluable contributions.

- My parents Alfred and Virginia Dube for their financial support and the sacrifices they made to be where I am right now.
- Professor Ernst Ferg, Dr. Brandon Davoren and Dr. Xandri van Niekerk for guiding me through this process and providing me with the necessary tools required to see my studies through.
- Nompilo Ntombela for teaching me to operate the equipment required to make any of this possible.
- Nelson Mandela University for their generous contribution towards funding my studies and granting me access to their research facilities.
- uYilo and eNsta for allowing me to conduct tests using some of their specialized equipment.
- Nelson Mandela University Chemistry department for providing some of the research equipment and for the assistance provided by the staff, especially Dr Rekha Neglur for putting up with my challenges over the past two years.

Related publications by the author

A part of this work was submitted to South African Journal of Chemistry.

Application of Microcapsule Technology in Lithium-ion Batteries: A Review; T. Dube, E. Ferg, X van Niekerk and B. Davoren; *S. Afr. J. Chem.*, **78** (2024) 136–146 https://hdl.handle.net/10520/ejc-chem-v78-n1-a19

List of abbreviations

LIB	Lithium-ion battery
LIB's	Lithium-ion batteries
EV	Electric vehicle
EV's	Electric vehicles
BEV	Battery electric vehicle
BEV's	Battery electric vehicles
LCO	Lithium Cobalt Oxide ($LiCoO_2$)
LMO	Lithium Manganese Oxide ($LiMn_2O_4$)
NMC	Lithium Nickel Manganese Oxide ($LiNi_xMn_yCo_{1-x-y}O_2$)
LTO	Lithium Titanate (Li_2TiO_3)
LFP	Lithium Iron Phosphate ($LiFePO_4$)
NCA	Lithium Nickel Cobalt Aluminium Oxide ($LiNi_xCo_yAl_zO_2$)
PE	Polyethylene
PP	Polypropylene
BMS	Battery Management System
PTC	Positive temperature coefficient
PNP	Triethoxyphospazen-N-phosphoryldiethylester
SET	Self-extinguishing time
CDP	Cresyl diphenyl phosphate
TPP	Triphenyl phosphate
TFP	Tris(2,2,2-trifluoroethyl) phosphate
GBL	γ-butyrolactone
LiODFB	lithium difluoro(oxalato) borate

PFN	Ethoxy-(pentafluoro)-cyclotriphosphazene
P2PFS	4,4’-(propane-2,2-diyl) bis(4,1-phenylene) disulfo-fluoridate
BA	Benzylamine
DBA	Dibenzyl amine
THA	Trihexylamine
$LiPF_6$	Lithium hexafluorophosphate
EC	Ethylene carbonate
EMC	Ethyl methyl carbonate
BMI	1’1’-(methyledi-4,1-phenylene) bismaleimide
DMC	Dimethyl carbonate
APIs	Active pharmaceutical ingredients
DMTP	1,1,1,2,2,3,4,5,5,5-decafluoro-3-methoxy-4-(trifluoromethyl)- pentane
PMMA	polymethyl methacrylate
SEI	Solid electrolyte interface
PVA	Polyvinyl alcohol
SDS	Sodium dodecyl sulphate

1: Introduction

The increasing concern about greenhouse emissions has prompted the adoption of various technologies to generate sustainable clean energy. These technologies encompass solar, wind, hydro, and tidal energy. However, a limitation of these energy sources is their inability to provide a consistent electrical energy stream, which has led to the exploration of battery solutions for storing excess energy generated during peak production periods. As a result, there has been a significant surge in adopting not only pure electrical energy storage systems to supplement the grid infrastructure but also to transform the transportation sector to low carbon emission alternatives primarily through the adoption of battery electric vehicles (BEV). With the emergence of LIB's as one of the primary energy storage systems for the portable electronic and BEVs there has been an increase in research focus on developing safer and long-lasting batteries that do not suffer from excessive capacity decay and thermal safety events. This can be seen graphically in **Figure 1.1** where the focused research that pertains specifically to safety aspects of LIB's has significantly started to increase from 2015 onwards as the uptake of larger battery packs in various applications has globally also increased. Of the approximately 13 000 journal articles published in 2022 in the field of LIB's, about 2 000 (15%) related to the specific topic of safety within the battery usage.

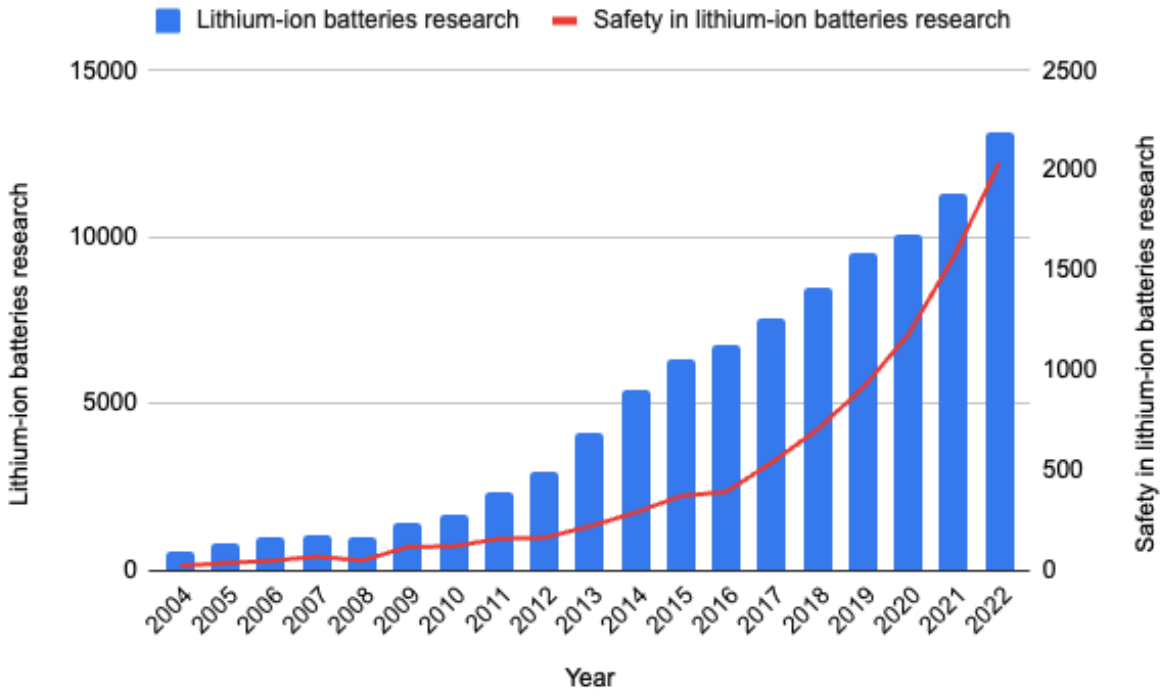

Figure 1.1: The number of articles published per year on the research that focused on LIB's and related safety aspects over the past 23 years.

The data shown in the graph was extracted from SCOPUS and WEB OF SCIENCE using search strings Lithium ion batteries OR LIB's OR LIB

Addition of preventative additives such as flame retardants directly into the LIB chemistry has been proven to hinder its electrochemical performance. Some recent studies showed that by adopting the encapsulation of such active compounds and including them into the electrolyte matrix, its effectiveness in suppressing the thermal event was shown and to some degree still maintain the electrochemical performance of the battery in application.[1–3]

The concept of encapsulation is found throughout nature and used extensively in the chemical and pharmaceutical industry. Typically, an egg can be considered as a macroscale version of a capsule, where a calcium-based shell would protect the yolk and germinal disk. Microencapsulation is often described as the process of enclosing

a substance in a fabricated shell or integrated chemical structure.[1,4] The encapsulated material is referred to as the core material and can be in the form of gas, liquid or solid. The capsule type depends on the phase that is being encapsulated and the method needed for encapsulation. It is also important to consider the reactivity of the shell material towards the material being enclosed during the encapsulation process. Generally, the microcapsules are inert and will not interfere with the normal chemical processes of its surrounding until it reaches the targeted area or condition. Microcapsules usually respond to an external stimulus to release the core material. Microencapsulation is used in a wide field of applications such as in active drug delivery in pharmaceutics, petrochemistry, food, cosmetics, civil engineering and the battery industry.[4]

In the pharmaceutical industry, microencapsulation is used to increase the stability, bioavailability and the controlled release of actives in a large variety of medical applications. This allows the shelf life, efficacy, and safety of active pharmaceutical ingredients (APIs) to be improved by encapsulating them in microcapsules.[4,5] Additionally, targeted applications of the API can be achieved to certain body tissues or organs using microencapsulation that rely on targeted drug delivery systems for the slow release of certain formulations by either oral or injectable medications. Most of the capsules fabricated for pharmaceutics, petrochemistry, food, cosmetics, civil engineering and the battery industry are meant to either increase performance [6], act as self-repair mechanisms [7,8] or to aid in the controlled release of encapsulant at a specific target or environment.[9–13] **Figure 1.2** displays the visual representation of microcapsules, illustrating both single-core and multi-core configurations. These microcapsules are applicable in the scenarios mentioned earlier.

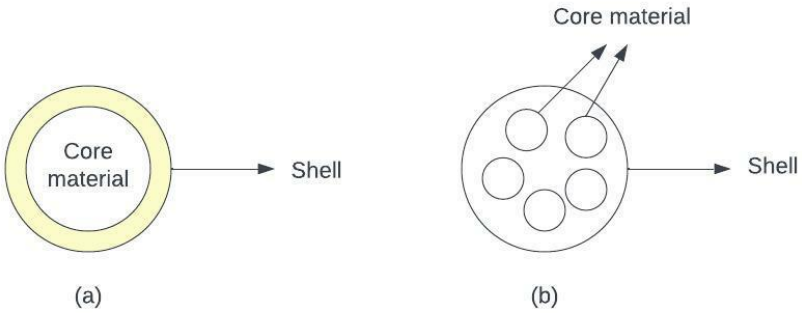

Figure 1.2: Common morphology of microcapsules: (a) single core microcapsule (b) multi core microcapsule.[14]

Problem Definition

The safety of LIB's for use in BEV's and suitable electronics is dependent on various operating and external conditions. If the battery or battery pack is exposed to harsh conditions, the aging process of the battery or pack increases and there is an increased chance of thermal runaway. To mitigate risks of thermal runaway, researchers have started adding chemical additives to LIB. These chemical additives either act as flame retardants or blocking agents (prevent ion movement between cathode and anode). One major obstacle in this field of study is the insufficient encapsulation research of several chemicals additives meant to reduce the effect of thermal runaway. Addition of unencapsulated chemical additives inside LIB often results in undesirable reactions with the battery components that reduces the effectiveness of the battery in application.

It is essential to comprehend and resolve this issue if safer and more effective lithium-ion batteries are to be developed. In order to minimize thermal runaway and preserve the long-term stability and performance of the battery system, research efforts should concentrate on improving the encapsulation methods for these additives, making sure

that they are properly integrated into the battery architecture, and assessing their usefulness.

Research Objectives and Aims

This research will focus on comparing various potential electrolyte additives as thermal shutdown agents, without affecting the electrochemical performance of the battery.

With the objective above, the aim of this research is:

- To identify possible thermal shutdown agents which can be used as electrolyte additives.
- To study and understand the possible thermal shutdown agent's activity in the most commonly used electrolytes for LIB.
- To incorporate the additives into a LIB and to evaluate its effect on the electrochemical properties as well as its ability to reduce the effects of a possible thermal event.
- To use encapsulation as a suitable mechanism to stabilize and include the additives to the electrolyte in a battery.
- To subject a built LIB coin cell to relatively high temperatures and to demonstrate the effectiveness of the encapsulation of the additive to "shutdown" the internal ionic conductivity thereby preventing a thermal event.

2: Literature Review

2.1 Lithium-ion batteries electrochemistry

Lithium-ion batteries are typically comprised of the four major battery components namely cathode, anode, separator, and electrolyte which can be simplistically depicted in **Figure 2.1**. During discharge Li^+ ions migrate from the anode to the cathode through a predominantly organic based electrolyte and vice versa upon charging. The process of the lithium-ion insertion in the anode or cathode material is referred to as intercalation and during charging the lithium-ions inserted on the anode acts as a process of energy storage.[15]

A lithium-ion battery is charged by switching the direction of the current flow, which drives the lithium ions back from the cathode to the anode. As the anode takes the lithium ions from the cathode, it transforms from an oxidized state (Li-ion deficient) to a reduced state (Li enriched).[16] The cathode, which was once reduced (Li-ion enriched), is now oxidized (Li-ion depleted) as it loses lithium ions to the anode at the same time. Because of this, while a battery is being charged, the cathode switches to becoming the anode and vice versa, and the electrochemical processes that took place during discharge are virtually reversed.[16] $LiCoO_2$ is one of the most commercialized cathode-based cell and the redox reactions that happens in the cell during discharge can be described as follows.[16]

$LiCoO_2 \leftrightarrow Li_{1-x}CoO_2 + xLi + xe^-$ $(1 < x > 0)$. Cathode eq 1

$6C + xLi + xe^- \leftrightarrow Li_xC_6$ $(1 < x > 0)$. Anode eq 2

$LiC_6 + CoO_2 \rightarrow C_6 + LiCoO_2$ $E = 3.7$ V at 25^oC eq 3

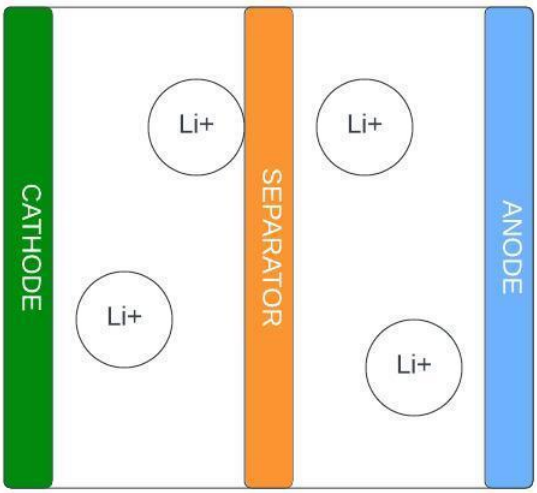

Figure 2.1: Schematic drawing of a lithium-ion battery

2.2 Cathode chemistry

The most used commercial combinations for LIB are lithium nickel manganese cobalt oxide (NMC), lithium ferro-phosphate (LFP), lithium nickel cobalt aluminium oxide (NCA), lithium cobalt oxide (LCO), and lithium manganese oxide (LMO).[16] These different cathodes have different maximum temperatures at which thermal runaway failure becomes self-propagating hence some are suitable for slightly higher operating temperatures. For example, the LMO cathode material is more stable over a wider temperature range of up to 250 ^{o}C and higher.

The use of the well-known iron phosphate olivine structure (LFP) as cathode material in lithium-ion batteries was invented by Dr John Goodenough and co-workers in the year 1997 and A123 Systems was one of the first companies to commercialize this technology.[17] Even though the overall cell's open circuit potential was lower than other types of commercial cells, it gained some traction in the late 90s in a variety of applications due to its lower manufacturing cost and inherent safer cell chemistry. As shown by the comparative study, (**Figure 2.2**) it has the lowest energy density (Wh/L)

but a significantly more stable chemistry upon heating when subjected to typical conditions of a thermal event.[16] The LFP cathode material starts to decompose at different temperatures, where at 80 °C the surface films decompose with neglectable heat production and full decomposition only happens at 250 °C.[18]

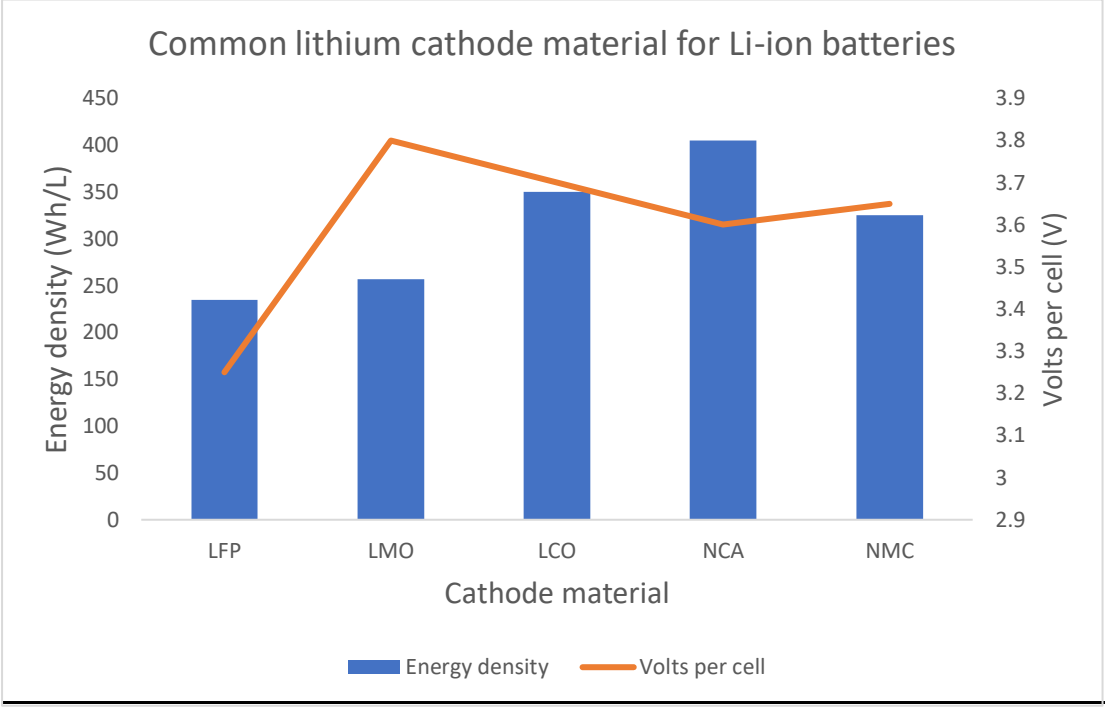

Figure 2.2: Energy density and volts per cell for the commonly used cathode material.[18,19]

The NMC cathode material is widely used in electric vehicles because of its higher energy density, higher voltage per cell, high life cycle, and high-power output.[18] NMC is relatively stable, and the thermal runaway temperature is reported in literature to be above 220 °C.[20]

Most portable electronics still make use of LCO based cathode material as the chemistry of choice for the LIB cell because of its higher energy density, higher number of capacity life cycles and higher power output. However, the cell chemistry suffers from a lower thermal runaway temperature of around 150 °C, where the decomposition

of the cathode oxide promotes the thermal self-propagation at these temperatures by fuelling the reaction with the release of oxygen.[18,19]

A cathode cell chemistry that has grown in popularity over the last few years is the NCA. It is used in the portable power storage units and electric vehicles that are manufactured by Tesla. It is their preferred choice of chemistry and has similar electrochemical properties like that of the NMC based chemistry and several reports have stated that it is stable up to 215 ^{o}C.[15,21]

2.3 Anode chemistry

The anodes of lithium-ion cells are usually made of carbonaceous materials that include graphite and graphene as being the more popular choices. The use of carbonaceous anodes in the manufacturing of cells has increased the safety of the batteries considerably when compared to the conventional use of lithium metal as the anode material. With the slow transport of lithium ions from the surface of the carbon moieties into the layered structure, this reduced the formation of dendrites on the surface of the anode thereby reducing the danger of short circuits to occur during repetitive capacity cycling. In addition, the carbon-based material has relatively high thermal stability and are reported to only decompose around 450-500^{o}C for graphitic carbon anodes and 250-350 °C for non-graphitic anodes.[22] Yu et al (2023)[23] data show that graphene oxide as a composite anode (CoO@RGO) decomposed at temperatures greater than 300^{o}C. Anode decomposition in lithium-ion batteries can lead to the formation of a solid-electrolyte interphase (SEI) layer, which can have both positive and negative effects on battery performance. On one hand, a stable SEI layer can improve battery cycling performance and prevent further electrolyte decomposition. On the other hand, an unstable SEI layer can lead to lithium-ion

depletion, dendrite growth, and ultimately, battery failure. Anode decomposition can also lead to gas formation, which can increase internal pressure and cause the battery to swell or rupture. Preferably the hard and soft carbon morphologies are mixed to get the best properties.[15] Lithium titanate (LTO) as the anode material has also shown to improve the safety aspects when compared to conventional carbon-based anode materials. These include the ability to increase the charging times, increased stability, and improved cycle life, with the only downside that the use of LTO as the anode would decrease the overall cell OCV which would typically be for a LCO/LTO combination of around 2.7 V. LTO has shown good results when being used at very low temperatures due to its unique crystal structure and lithium-ion diffusion properties. The crystal structure of LTO is spinel, which allows for lithium-ion diffusion in all three dimensions. This property allows LTO to maintain high power and capacity even at low temperatures because the lithium ions can easily move through the crystal structure to the surface of the material where they participate in the electrochemical reactions.[15,16]

Transition metals are also being looked at for use as anode materials they have high theoretical specific capacity, and high-power density. They are not widely utilized because they experience irreversible capacity loss during the initial cycling process.[25] Numerous studies on transition metals and their oxides focus on their encapsulation to mitigate capacity decay resulting from the volume expansion that occurs during lithiation and delithiation.[25–27] Other anode materials are under research and promising data have been gathered from the incorporation of silicon, carbon nanotubes, and nanocomposite materials as anode materials. Some research shows that silicon anodes have higher specific capacity compared to their carbon-based counterparts, but they are prone to volume expansion and formation of unstable SEI layers.[28]

2.4 Separators

The purpose of a separator is to physically separate the anode and cathode material and yet allow the lithium ions through for conductivity. When picking separators for lithium-ion batteries certain parameters must be met. A good separator must withstand the corrosiveness of the electrolyte components, be cost effective, be stable over long periods of time, possess wettability properties that relate to the liquid electrolyte, be relatively thin which is typically between 20-25 μm for lithium cells with small pores around 1μm and have a porosity between 40-60%.[21] The most common separators used in commercial lithium-ion cells are polyethylene (PE), polypropylene (PP), a mixture of PE and PP and a tri-layer of PP/PE/PP. PE has a low melting point of 135 ^{o}C and is usually the middle sector of a tri-layer separator of PP/PE/PP.[29] PP has a melting point of 155 ^{o}C. During a typical thermal event of a cell, when higher temperatures are reached, the PE, PP or PP/PE blends separators tend to shrink and melt in temperatures that range from 135 ^{o}C to 165 ^{o}C, followed by combustion above 165 ^{o}C[30], causing the anode and cathode to short circuit thereby accelerating the thermal event.[21,29,31] Nonwoven separators such as polyolefin, polyamide, polytetrafluoroethylene, polyvinylidene fluoride, polyvinyl chloride and polyester have been explored and were fabricated using either the papermaking, melt-blowing, or electrospinning processes. These usually have high porosity (60 - 80%) with larger pores (20 – 50 μm).[31]

2.5 Thermal runaway

Thermal runaway in LIB's refers to a condition where the internal temperature of the battery rapidly increases due to a failure in its thermal management system, leading to further temperature increases and eventually resulting in a thermal explosion or fire.[32] This phenomenon can happen in different ways that are either triggered by an

internal (within the cell) event or externally due to a mechanical, thermal, or an electrical trigger[33–35] that causes the battery to reach the self-propagating thermal runaway scenario. Feng *et al*. (2018)[35] described the penetration of the cell by a solid object as a mechanical issue where the separator is damaged that results in the anode and cathode material to cause an internal short circuit. This can lead to a rapid increase in temperature to a point where the thermal event becomes self-propagating. During thermal events like external overheating (when the environment or operational temperatures are exceeded) there is a greater chance of the separator to shrink that leads to an exothermic reaction between cathode and anode material within a volatile electrolyte that will result in a thermal event. An internal short circuit that occurs near the electrode edges of a cell can release small amounts of energy that is sufficient to achieve temperatures between 130-160 ^{o}C. These reactions would then lead to further increases in cell temperature and the degradation of the active material and combustion of the electrolyte.[35–37] According to Ren *et al* (2021)[38,39] the primary source of heat generation in LIB's thermal events occurs between the anode and cathode reactions, rather than between the anode or cathode with the electrolyte. External electrical triggers that can lead to a thermal runaway event can include overcharging, over-discharging, or an external short circuit. Externally, the control of the charging and discharging of the battery module or pack are usually done by the battery management system (BMS) that also monitors the temperature status of the battery. Advanced systems allow for the thermal monitoring at the cell level, even within a large battery pack.[36]Other internal triggers could come from contamination such as water in the electrolyte or foreign solid particles. Water would contribute to the decomposition of the electrolyte and the unwanted particles, and depending on their composition, can lead to the damaging of the separator that results in an internal short-circuit.[36] **Table**

2.1 summarises the thermal events that can occur as a cell or battery heats up and approaches the thermal runaway event where it becomes self-propagating.

Table 2.1: Events that can lead to a thermal runaway event in LIB's.

Event	**Description**	**Temperature range (°C)**	**Reference**
Increased rate of reaction	Refers to how quickly the lithium ions can move between the anode and the cathode during charge and discharge cycles.	>80	[35]
SEI decomposition	The decomposition of a thin film that forms on the surface of the anode when the battery is first charged.	60-85	[35]
Anode/cathode-electrolyte reactions	At high temperatures, the electrolyte may decompose, leading to the formation of reactive species such as free radicals, which can react with anode or cathode material.	130-160	[35]
Separator shrinkage	When the temperature within the cell rises rapidly, the separator material breaks down and can cause it to shrink.	110-150	[35]
Cathode decomposition	At high temperatures, the cathode material can decompose and release oxygen, which can react with the flammable electrolyte and cause an exothermic reaction.	>130	[40]
Heat release	Occurs when the heat generated from exothermic reactions cannot be effectively dissipated, leading to a further increase in temperature. This can result in a self-accelerating reaction, causing the battery to reach temperatures well above its normal operating range.	120-230	[40]

Ren *et al* (2021)[38] showed how the voltage of the cell would be influenced by the increase in temperature of the cell above 150 °C (**Figure 2.3**). The cell voltage drops drastically as events like cathode decay, separator shrinkage and short circuiting starts to occur.

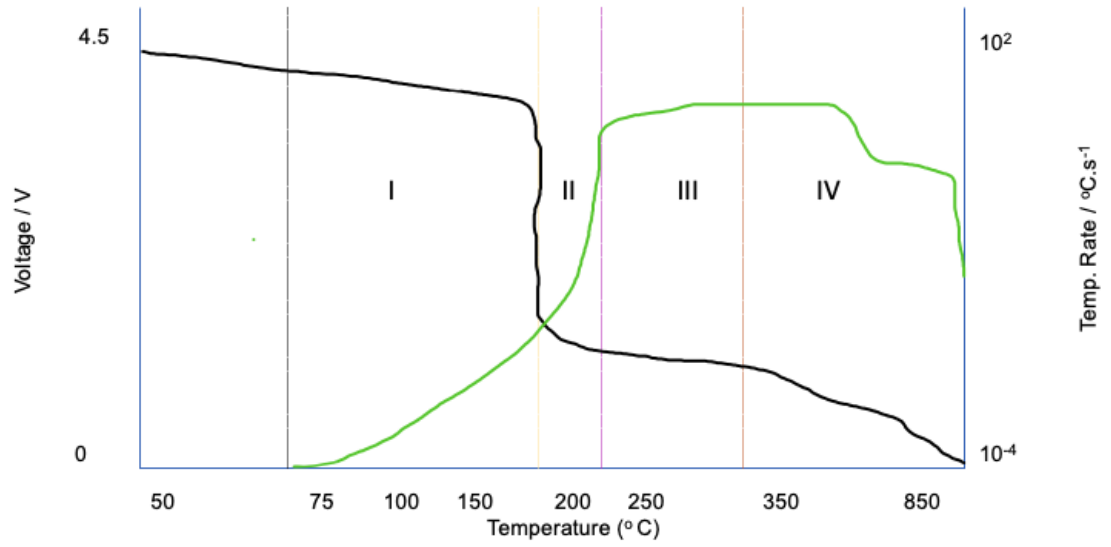

Figure 2.3: Stages of thermal runaway in batteries adapted from Ren et al (2021).[38]

Self-heating usually starts at temperatures around 75 °C and is due to the cathode and the SEI layer decomposition (first part of stage I in **Figure 2.3**). At this point there is no inherent effect on the voltage of the cell. After onset at 75 °C the second phase of stage I begins and spans from 80 °C to 170 °C (stage I in **Figure 2.3**). This is then followed by a gradual decrease in the cell voltage due to the increased occurrence of cathode/anode-electrolyte reactions and the melting of the separator material. Above 170 °C (Stage II in **Figure 2.3**), the thermal event becomes self-propagating with a significant increase in the temperature rate. Any preventative heat or flame retardancy be it internally or externally should become effective below this temperature. Stage III and IV would be considered as being completely self-propagating that often leads to enough internal pressure that can result in an explosion.

Over the last 18 years, research papers that were published specifically on the topic of thermal runaway in LIB's is summarized in **Figure 2.4**. The data shows that over

the last 5 years, there was a significant increase in publications that considered the use of flame retardants. In 2022 about 16% of the journal articles published were specific on the addition of flame retardants to reduce the effect of thermal runaway in LIB's.

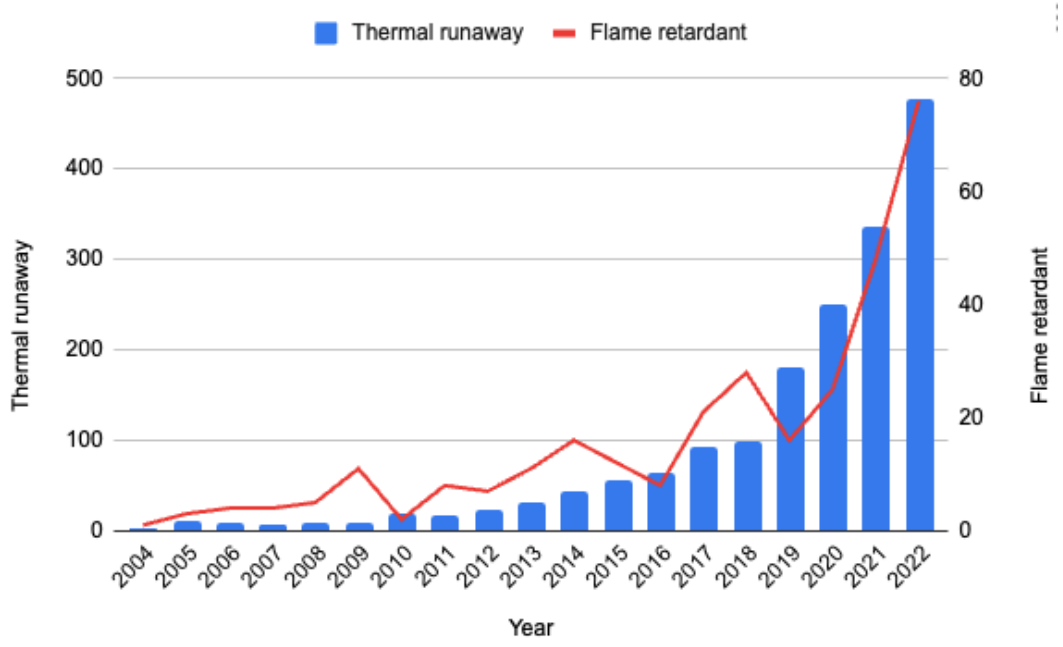

Figure 2.4: Research done on thermal runaway and the use of flame retardants to mitigate its effect

The data shown in the graph was extracted from SCOPUS and WEB OF SCIENCE using search strings Lithium ion batteries OR LIB's OR LIB AND thermal runaway/ flame retardants

2.5.1 Physical methods of preventing thermal runaway.

Over the years several safety mechanisms have been developed for lithium-ion batteries amid safety concerns. Some types of lithium-ion batteries come coupled with internal fuses that are triggered during overload conditions.[41] Currently, the use of current limiting devices such as positive-temperature-coefficient (PTC) devices that provide current limiting capabilities over a wide range of temperatures are being

implemented in some designs.[42] Pressure release mechanisms are also used as a secondary backup mechanism to reduce the effects of excessive increases in internal pressures within the lithium-ion battery due to gas formations or other types of mechanical stress.[43]

In a thermal event, there are external systems that can suppress the propagation of the heat to adjacent cells or battery components. These include the use of compressible polyurethane foams that are typically combined with flame-retardant compounds that are released at a certain temperature.[44] The use of firewall barrier designs between cells and modules that are typically designed with intumescent coatings and can mitigate cell to cell thermal propagation. These are most used in large pack designs that are used in applications that require a large degree of safety such as a road vehicle or airplane. These external barriers notably increase the overall mass of the battery that needs to be factored in when designing an energy storage system that is confined to limited space.

A battery management system (BMS) is a system that manages the performance, safety, and reliability of a rechargeable battery pack. It monitors and regulates several battery characteristics, including voltage, temperature, current flow, and state of charge. A BMS's primary job is to safeguard the battery against overcharging, over discharging, and overheating, which can shorten its lifespan and jeopardize its safety by balancing the cells and managing the charging and discharging processes. It also helps to enhance the performance of the battery.[45,46]

Another approach would be to build a thermal suppression system internally into the cell that can be chemically triggered when the cell reaches a certain temperature.

2.5.2 Internal chemistry to reduce the risk of thermal runaway

The internal lithium-ion cell chemical shutdown would refer to a method in which certain additives in the cell's electrolyte or solid component would prevent or reduce the thermal event by absorbing heat that is released, slowing down the reaction, or by inhibiting the propagation of the oxidation reaction. Most of the chemicals inside a lithium-ion cell are easily oxidizable and certain additives reduce this effect. Over the past few years, numerous investigations have been conducted to identify suitable chemicals that are endothermic reactions propagators to counter the rapid exothermic reactions that happen during thermal runaway. These also act as barriers that can form between the anode and cathode materials to reduce the propagation of the shortening between the electrodes. These include phosphate-based flame retardants, diols and amines.[38-42]

The use of flame retardants in lithium-ion cells have gained popularity due to their ability to have endothermic decay properties at high temperatures to counter the ever-increasing temperature. Flame retardants are extensively used in other applications such as fabrics, polymers, and the paper industry. Different types of flame retardants have been examined in terms of their compatibility with the cell's electrode and electrolyte. These can be classified based on their main chemical constituents, that include phosphorous-based compounds, fluorine-doped compounds, amines, and diols.

2.5.2.1 Phosphorous based flame retardants

Most known phosphorous based flame retardants are added directly to the electrolyte or mixed with the cathode material. Wang *et al* (2019)[47] have shown that the electrochemical performance of such cells is negatively influenced when higher weight

percentages of up to 20% of retardant are added. The higher amounts of retardants improve the self-extinguishing times (SET) that are typically measured in seconds per gram (sg^{-1}) of flame retardant added or just in seconds (s) only. The main reason for the reduction in the electrochemical performance is their high affinity towards lithium-ions which are produced at the anode during the SEI layer formation. This then obstructs the progression of the SEI layer formation and reduces the amount of lithium ions that can pass through the layer during the charge and discharge processes.[48]

Wang et al (2019)[47] explored the option of using triethyl phosphate and triethyl phosphite as flame retardants. The results showed when higher weight percentages of triethyl phosphate up to 20 wt% do not have any significant effect on the cell's performance when compared to similar amounts of triethyl phosphite. It was shown that triethyl phosphate tends to stabilize the electrolyte and retains about 99% of the capacity after 100 cycles.[47] However, the use of triethyl phosphite decreases the cell performance with time, this is because of the oxidation decomposition of trivalent phosphorus contained in triethyl phosphite during cycling.

Dimethyl methyl phosphate (DMMP) is another phosphate-based retardant that has been studied under different parameters such as amount of DMMP used and its effect on conductivity and viscosity of electrolytes. From the studies it was found that an increase in the amount of DMMP used reduced ionic conductivity and increased viscosity of the electrolyte.[49] Xiang et al (2007)[49] used the material in a cell with $LiCoO_2$ as the cathode material and with $LiPF_6$/EC:DEC as the electrolyte. The results showed that there was an improvement of the SET from 140 sg^{-1} (base electrolyte) to 0 sg^{-1} (with 50% DMMP doped). This however severely affected electrochemical

performance where it was shown that a small percentage 5% (v/v) of vinylene ethylene carbonate that was added to the electrolyte would boost the cell performance by improving the capacity and cycle life.[49] When a flame retardant was used in a cell that used $LiNi_{0.8}Co_{0.2}O_2$ as the cathode, cells with 15 wt% and 20 wt% DMMP showed 1.8 s and 0.8 s SET times respectively. Their results showed that the addition of 20 wt% DMMP to the electrolyte had a comparatively similar cycling performance to cells with the base electrolyte after 16 cycles.[50] According to Jiang et al[1] the addition 10, 20 and 30 wt% of DMMP to the electrolyte had better capacity retention when compared to base electrolyte.

Triethoxyphospazen-N-phosphoryldiethylester (PNP) was another phosphate-based compound that was investigated as a flame-retardant additive with $LiMn_2O_4$ as the cathode material in Li-ion cells.[51] The research showed that up to 10 wt% of PNP would reduce the SET times relative to the base electrolyte while keeping the cycling performance close to the base electrolyte. Further increase of PNP inside the lithium cell affected the cell performance but improved SET times.[51]

Jiang et al (2022)[1] reported the use of cresyl diphenyl phosphate (CDP) and triphenyl phosphate (TPP) as flame retardants in cells that significantly reduced the cell performance in terms of its capacity. The addition of up to 20 wt% of each to the cell electrolyte would reduce the capacity retention up to 46% and 54% respectively and would not be ideal for use in commercial products. The authors showed that the TPP addition would cause poor cell performance because of the continuous destruction of the cathode/electrolyte interface. The advantage of wanting to use TPP or CDP is because they are low cost effective flame-retardants. Different approaches for the use of TPP were investigated by Ye et al (2020)[2] that fabricated a polyimide (PI)-TPP-Cu

current collector with flame retardancy capabilities. Their results showed that the flame retardancy was dependent on the current collector's thickness, with the 9μm thick collector outperforming the thinner counterparts. Jiang et al (2022)[1] reported that 20 wt% of TPP embedded on a polyimide separator had a SET of between 25 - 30 sg^{-1} when compared to the SET time of 90 sg^{-1} by when TPP was not embedded in anything.

At high temperatures, the electrolyte can generate a flammable vapor, such as a gaseous carbonate solvent (RH), which can decompose in a flame and produce H* radicals. These radicals react with the oxygen from the cathode to create HO* radicals. The HO* radicals can be regenerated and accumulate by reacting with hydrogen (likely from the decomposition of the electrolyte and trace water), resulting in a sequence of free radical reactions that support combustion. In general, phosphorous based flame retardants can be described to follow the reaction mechanism described below after combustion of alkyl esters:[52]

$[P]\bullet \rightarrow$ gaseous phosphorous free radicals

$RH \rightarrow R\bullet + H\bullet$

$ROOH \rightarrow RO\bullet + HO\bullet$

$[P]\bullet + H\bullet \rightarrow H[P]$

$[P]\bullet + HO\bullet \rightarrow H[P] + O\bullet$

2.5.2.2 Fluorine based retardants

Fluorinated electrolytes function with antioxidants properties which are essential for reducing the shuttle system. A shuttle reaction refers to a process in which an intermediate molecule or ion are shuttled between two different locations or environments, usually within a larger chemical system. This intermediate can often act as a carrier of energy or charge, allowing it to transfer from one location to another which can contribute to thermal runaways. [53] Tris(2,2,2-trifluoroethyl) phosphate (TFP), is a fluorine and phosphate -based flame retardant and its use in LIB was reported by Gu et al (2021),[53] whom in their work also pointed out that mixing it with γ-butyrolactone (GBL) formed a non-flammable electrolyte. Its performance was studied in a graphite/$LiNi_{0.5}Co_{0.2}Mn_{0.3}O_2$ cell that made use of a LB 301 electrolyte ($LiFP_6$ DMC:EC (1:1)) and showed a 90.8% capacity retention at room temperature and pressure.

Ethoxy-(pentafluoro)-cyclotriphosphazene (PFN) was used as a performance enhancer and to improve the safety in lithium-ion batteries. Li et al (2018)[54] tested its performance in LIBs made with $LiNi_{0.5}Mn_{1.5}O_4$ cathode material. The addition of more PFN promoted the electrolyte to degrade or oxidise to a denser material like Li_3PO_4 and to form a film on the cathode layer which aided in its cycling stability. The study showed that cells with 5 wt % of PFN in the electrolyte would result in the cell to have a higher specific capacity and a better coulombic efficiency. Their study also showed that the addition of 5 wt% PFN resulted in a SET time of 3s at the same time keeping the conductivity as high as 11.5 $mS.cm^{-1}$. The conductivity was similar to the cells with the baseline electrolyte which has a conductivity around 11.8 $mS.cm^{-1}$ that would report a SET time value of 5 s.

Oh, et al (2022)[55] investigated the use of 4,4'-(propane-2,2-diyl) bis(4,1-phenylene) disulfo-fluoridate (P2PFS) as a flame retardant in cells made with $LiNi_{0.9}Co_{0.05}Mn_{0.05}O_2$ cathode material. Their results showed that the SET times for a P2PFS with a 10 wt% was 0.2 s, this SET is comparatively low because the effect of the flourosulfate groups in the additive would significantly suppress the flammability of the electrolyte material. The additive also improved the capacity cycling performance of the cell when compared to the cells made with the base electrolyte. They showed that the capacity retention was 94% after 70 cycles.[55]

Fluorine based flame retardants follow the following reaction mechanism after combustion of alkyl esters:[52]

$[F]\bullet \rightarrow$ gaseous fluorine free radicals

$RH \rightarrow R\bullet + H\bullet$

$ROOH \rightarrow RO\bullet + HO\bullet$

$[F]\bullet + H\bullet \rightarrow H[F]$

$[P]\bullet + HO\bullet \rightarrow H[P] + O\bullet$

2.5.3 In-situ polymerization reactions involving electrolyte components.

In-situ polymerization reactions involving electrolyte components refer to the chemical reactions that occur within the lithium-ion battery's electrolyte solution during the battery's operation. These reactions can lead to the formation of polymer materials that can impact the battery's performance, including its cycling stability and safety.

2.5.3.1 Amine based retardants.

Benzylamine (BA), dibenzyl amine (DBA), and trihexylamine (THA) have been studied in their use as flame retardants in lithium-ion batteries.[56] They were used in electrolytes that contained 1M $LiPF_6$ in ethylene carbonate (EC) and ethyl methyl carbonate (EMC), with a EC to EMC mass ratio of 1:1. Benzylamine and dibenzyl amine were found to be miscible with the electrolyte to, and in turn reduced the ionic conductivity of the electrolyte and thereby increased the internal cell resistance. THA was found to be immiscible with the electrolyte mixture and blocked the ionic transport within the cell by blocking the movement of ions at the cathode due to the low solvation properties [56]. The amines can react with ethyl carbonate to form derivatives of benzyl carbamate which then further reacts with ethyl carbonate in a $LiPF_6$ catalysed polymerization reaction that can be summarized in the following reaction mechanism **(Figure 2.5).**[56]

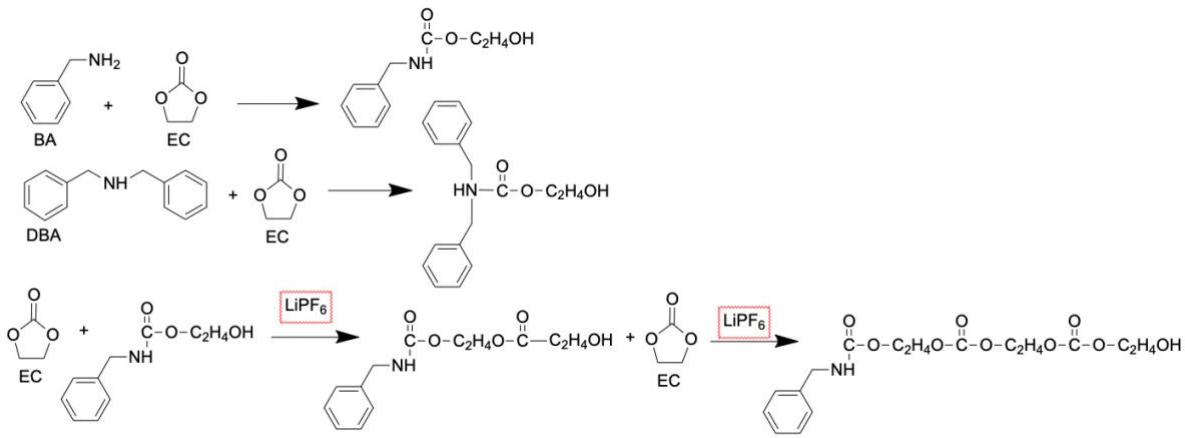

Figure 2.5: Reactions of BA and DBA with EC and $LiPF_6$ catalysed polymerization reaction

Xia et al (2012)[57] looked at the potential of in-situ polymerization by studying the reaction of 1'1'-(methyledi-4,1-phenylene) bismaleimide (BMI) in lithium-ion battery

electrolyte composed of 1M $LiPF_6$ in EC/DMC/EMC at 1:1:1 by volume. Their work revealed that the chemical reacts with the double bonds in the maleimide rings to form a homopolymer that was shown at temperatures above 116°C to solidify instantly with aid of a thermal initiator 2,2'-aze-bis-iso-bytonitrile as shown in **Figure 2.6**. The test cells studied showed little differences in their capacity cycling performance when compared to the cells made with the base electrolyte only.[57]

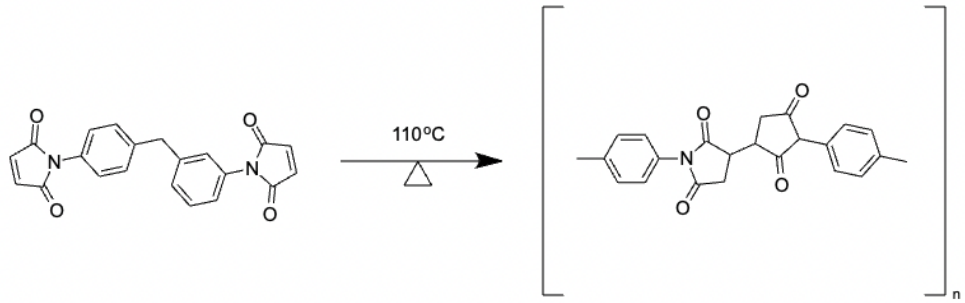

Figure 2.6: BMI polymerization reaction at 110°C to form polyBMI.[57]

Compunds 1,2-ethanediamine and 1,3 propanediamine as additives to the electrolyte were also found to have the ability to react with the ethyl carbonate thereby decreasing its dielectric constant that results in a more compact and homogeneous electrode-electrolyte interface, which in turn can improve the distribution and effectiveness of flame retardant additives.[58] The reaction rate between either of the additives and ethyl carbonate increased with an increase in cell temperature that promoted the increase in the viscosity of the electrolyte until a final solid product was formed.[58] This can be seen in the following reaction mechanism where the resultant product formed would be carbamide.

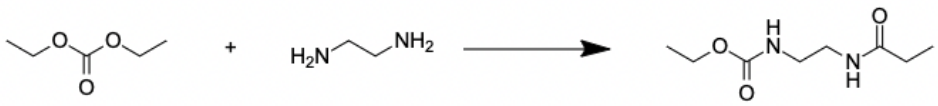

Figure 2.7 : Reactions of diamines and diethyl carbonate.[44]

2.5.3.2 Diol based retardants

Compunds 1,2-ethanediol, 1,3-propanediol and 1,5-pentanediol can act in the same manner as 1,2-ethanediamine as an inhibitor within a cell. It was found that when added directly to the electrolyte mixture they instantly increased the viscosity of the electrolyte mixture thereby reducing the ionic conductivity. At higher temperatures the viscosity increases significantly thereby reducing the effect of a short circuit failure that effectively reduces the amount of heat emitted.[58] Selvas et al (2014)[59] reported that diols can react with both dimethyl carbonate and diethyl carbonate in the presence of phosphonium salts to form cyclic carbonates and linear bicarbonate products as shown in **Figure 2.8**. Unsymmetrical dialkyl carbonates are gels and these gels prevent ease of movement of ions involved in the shuttle reactions that lead to thermal runaway.

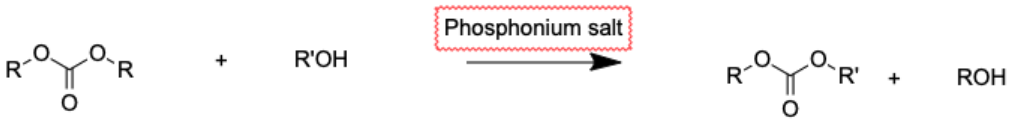

Figure 2.8: Synthesis of unsymmetrical dialkyl carbonates via transesterifications catalyzed by phosphonium salts.

2.6. Microencapsulation and Lithium-ion batteries

2.6.1. Microcapsules

There are five major categories that are applied to encapsulate specific active materials. These include chemical, physical, physiochemical, electrostatic, and mechanical methods.[60] In battery material related processes, the most common ones are the chemical and physiochemical techniques. Chemical batch methods tend to produce microcapsules with a wide size distribution and have lower encapsulation efficiency. Encapsulation efficiency would relate the amount of active material (mass) found inside the shell and the mass of the shell. It is important to produce capsules with a relative uniform size in order allow similar amounts of active core material to be present in most capsules to allow for maximum effectiveness.[61]

2.6.2. Encapsulation techniques

2.6.2.1 Coacervate encapsulation

This is a type of encapsulation that involves separation of two phases, namely the coacervate phase (dense phase that forms capsules) and a continuous phase that forms the surrounding boundary. Coacervate microcapsules can either be simple or complex coacervates.[14] Complex coacervation is a type of microencapsulation that involves neutralization of two oppositely charged polyelectrolytes.[14] This type of encapsulation is normally used in the food and drug industry to prevent oxidation of bioactive molecules where different types of cores can be formed using this type of encapsulation. Glomm *et al*. (2023)[15] reported on the encapsulation of salmon oil to prevent oxidation. This was achieved using bovine serum albumin and acacia gums to form a coacervate.

Simple coacervation allows for the formation of hydrophobic shells on top of hydrophilic substances with a low interfacial energy and has been reported by Wang *et al*. (2023).[62] They showed the formation of a zein coacervate, a type of simple coacervate to adhere to cherry tomatoes to lengthen their shelf life. During the process of encapsulation, the hydrophilic regions interact with the water while the hydrophobic regions form coacervates on the surface of the tomatoes.[62]

2.6.2.2 Interfacial polymerization

This is a type of encapsulation which involves polymerization of monomers around the core material and requires an interface of two immiscible phases. There are 4 main types of polymeric shells used for interfacial polymerization. These include polyurea, polyurethane, polyester and polyamide where the polymer selected depends on the function of the microcapsule needed in application and the type of material being encapsulated. Yan *et al*. (2023)[63] demonstrated the formation of a polyurea shell by interfacial polymerization in order to encapsulate n-eicosane which was used for high thermal energy storage applications. The polyurea shell showed good stability during electrochemical cycling with no reported morphological changes. Zhao *et al*. (2023)[64] discussed the use of both interfacial polymerization and free radical copolymerization to form double shell lignin microcapsules which are a type of polyurethane shell microcapsules. The outer layer lignin-polyurethane shell was formed by biomass lignin as a chain extender and the inner layer was formed by polymerization of styrene and N-isopropylacrylamide. **Figure 2.9** depicts the use of two reactive monomers to form a polymer shell around the core material at an interface between two immiscible liquids.

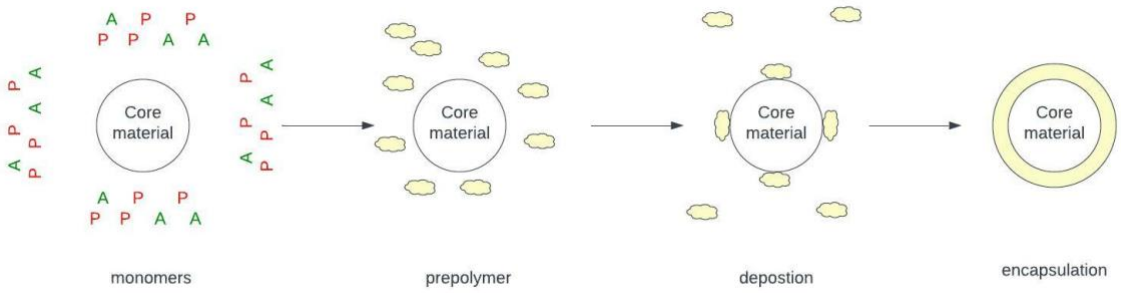

Figure 2.9: Interfacial polymerization process

2.6.2.3 Sol-Gel microencapsulation

This is a type of encapsulation that involves the formation of an emulsion of immiscible phases. In sol-gel encapsulation, a sol (colloidal dispersion of solid particles in a liquid) is transformed into a gel network which creates a solid shell. Park and Jo (2023)[65] demonstrated the encapsulation of molten salt using a TiO_2 shell in a surfactant free environment. The surfactant free microcapsules that formed were used in an energy storage application that showed better thermal reliability because the surfactants usually have a lower decomposition temperature than the shell and core material which will lead to early failure in the structural integrity of the capsule.[65] Silica based sol-gel microencapsulation have become a popular choice to make sol-gel microcapsules. Zheng *et al*. (2023)[66] fabricated phase change materials using paraffin as the core and SiO_2 as the shell. Sodium silicate was used as a precursor and their results showed that the sol-silica system stability was dependent on pH and slight shifts in pH by about 0.5 can affect the final shell formation.[66]

2.6.2.4 Spray-drying

Spray drying is a type of microencapsulation process that involves the use of a liquid solution that is atomized into droplets and then dried either by hot air or freeze drying containing the substance of interest. This type of technique allows the formation of

soft- or hard-shell microcapsules depending on the type of shell material used. Two primary forms of atomization are employed in these processes and are referred to as monoaxial spray-drying, which takes place when a single liquid is present in a two-fluid nozzle, or coaxial spray-drying, where two concentric liquid solutions are utilized within a three-fluid nozzle. This type of encapsulation process is commonly used for biochemical active materials. Berraquero-Garcia *et al* (2023)[67] reported on the encapsulation of polysaccharides, proteins and peptides using monoaxial spray-drying.

2.6.2.5 Electro-spraying

This type of encapsulation requires the application of an electric field to dry the formed nano or microcapsules. During formation, the feed solution passes an electrostatically charged nozzle which then causes the meniscus of the droplet to be polarized to form a Taylor cone. When the feed solution passes through the nozzle, the voltage increases thereby prompting an increase in surface tension of the solution which in-turn breaks the droplet that is then deposited onto a collector where it can evaporate. Bakola *et al*. (2019)[68] reported on the encapsulation of dipyridamole, an antithrombotic drug, by means of electrospray encapsulation using a poly (L-lactic acid) capsule. The study reported on the successful encapsulation of dipyridamole, but the capsules that formed would be double in size relative to the average size of poly (L-lactic acid) blanks.[69] Shlyaphikov *et al*. (2016)[69] explored the option of electro spraying DNA fragments. Their study showed that DNA fragments shorter than 5 kilo-base pairs were not damaged during the electro-spraying process. However, those longer than 5 kilo-base pairs were damaged upon formation of the Taylor cone.[69]

2.6.2.6 Flow focused encapsulation.

Flow encapsulation has become a more popular synthesis technique due to its ability to control the capsule sizes with a relatively narrow size distribution. The size of the capsules can be controlled using flow rates and related weight percentages of the mobile and dispersed phases.[10,70–74] The most traditional method used for encapsulation is the emulsion process and depends predominately on the agitation speeds for size control. Xu *et al*. (2020)[75] showed that higher rotation speeds yielded a narrower size distribution compared to lower rotation speeds. With a lower effective amount of the core material in each capsule. This in-turn would affect the amount required in the final release process in application. Size uniformity is also important to ensure higher rupture efficiency with an even distribution of the core materials during the rupture process.[9]

Multiple emulsions flow chemistry refers to the use of microfluidic systems to generate multiple emulsions, where two immiscible liquids are dispersed within another immiscible liquid to form droplets of one liquid within the droplets of another. When fabricating a single-phase emulsion, the mobile and dispersed phase must be immiscible. For double emulsions, the inner and outer drops must remain immiscible, whereas for multiphase emulsions the compartments next to each other must remain immiscible. This is summarized in **Figure 2.10** where emulsions are produced using a water phase (W) and an oil phase (O). The multiphase liquid micro-emulsions process is used in the pharmaceutical and food industry as delivery shuttles of the active ingrediencies for a variety of applications. [11,12,76]

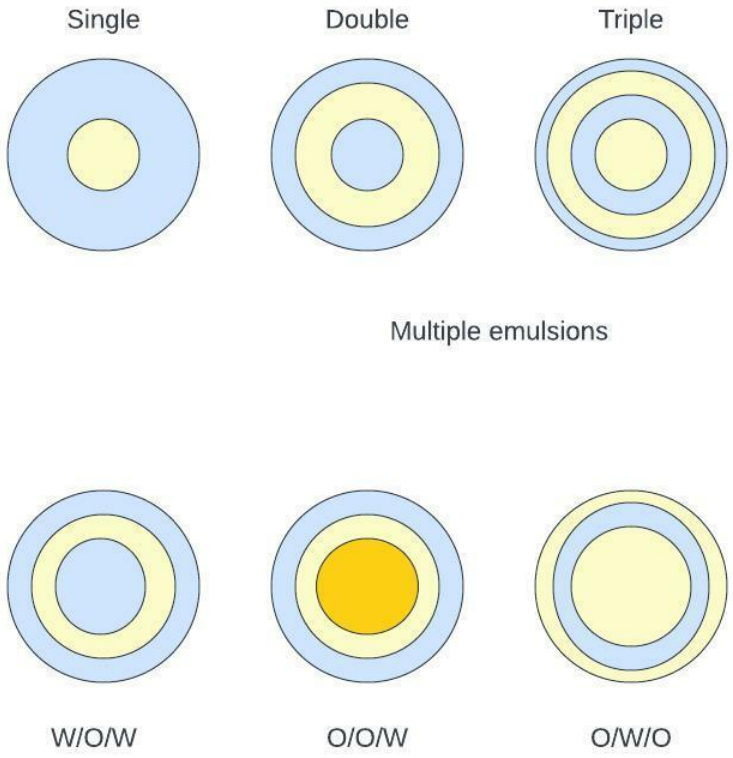

Figure 2.10: Types of emulsions and emulsions phases.[11,13]

Watanabe *et al*. (2021)[13] showed the use of a biopolymer composed of hexadecane and cellulose acetate to fabricate a microencapsulated paraffin-based material. Their studies revealed that when the weight % of the core material was increased, the shell thickness would decrease, and the corresponding shell diameter would then increase because of an increased volume. The work also revealed the negative effects of using a nucleating agent on the shell porosity, instead of using crosslinking agents to decrease the shell's porosity.[13] Souza *et al*. (2018)[8] showed that by using a double emulsion technique, it would improve the shell properties such as the effective payload, the permeability and its rigidity in efforts to encapsulate an aqueous core. This was done by making use of a flow focused device for a monodisperse w/o/w emulsion.[8] When fabricating microcapsules with microfluidic devices, the correct

surfactants should be used to prevent channel blockages. Surfactants can also affect the permeability of the shells due to hydrophile-lipophile in-balances that are present in the selected surfactant.[77,78]

2.6.3 Microcapsules for thermal runaway

Yim *et al*. (2015)[79] demonstrated the use of (1,1,1,2,2,3,4,5,5,5-decafluoro-3-methoxy-4-(trifluoromethyl)-pentane) (DMTP) as a flame retardant that was encapsulated in a polymethyl methacrylate shell (PMMA) suspended and placed in the cell separator. The results showed that the flame retardant in a LIB which is highly endothermic can easily suppress the exponential temperature increases during thermal runaway processes.[79] With the aid of a cross-linking agent, an oil-in-water emulsion-based polymerization reaction was used to safely enclose a fire-extinguishing agent inside a hard-polymeric shell. Direct contact between the extinguishing agent and the electrolyte was avoided by the capping of DMTP with a cross-linked PMMA shell, which also provided the electrolyte with high structural stability. A typical nail penetration test revealed that there was a reduction in the increase in cell temperature rate in the LIB that was tested with the encapsulated additive.

Lou *et al*. (2022)[80] reported the use of a N-H microcapsule embedded on the separator material to aid in the increased electrolyte uptake due to the presence of the N-H groups. The reported microcapsule contained a mixture of perfluoro(2-methyl-3-pentanone) and heptafluoro-cyclopentane as core materials which showed good endothermic activity at high temperatures. This would then suppress the exponential temperature increases during the thermal runaway event. Bagniska *et al*. (2018)[81] studied the effect of directly placing a flame-retardant tri(2-chloroethyl-phoshate) into

the LIB electrolyte chemistry versus the use of the same encapsulated flame-retardant. They showed that the un-encapsulated flame retardant reduced the ionic conductivity of the electrolyte while the encapsulated additive had little effect on the battery electrochemistry.[81]

Ammonium phosphate is another flame retardant that is used in LIB's due to its ability to undergo endothermic decomposition when exposed to high temperatures. Xu *et al* (2023)[82] reported on experiments that involved the incorporation of a flame retardant (ammonium phosphate) into a solid-solid phase change material (normally used for thermal management) made up of polyethylene glycol and N',N'-Methylenebisacrylamide. Melamine-formaldehyde was the capsule shell of choice for this experiment and further electrochemical studies showed that 19% w/w of microcapsules in the phase change material was enough to provide good thermomechanical properties without compromising its flame retardancy.

Ma *et al* (2022)[83] explored the option of coating ammonium phosphate with ammonium hydroxide followed by their encapsulation using a polyurea formaldehyde shell. The capsules were applied onto the electrode of a LIB cell and the results showed that the addition of the capsules improved the thermal stability and that all additions with less than 20% w/w ratio still had cell capacity retention of not less than 94% after 100 cycles.[83]

Lui *et al* (2021)[84] coated a polyolefin separator with some ceramic based silica microcapsules. These microcapsules contained a phase change material (molten steric acid) and a flame retardant (triethyl phosphate). The molten steric acid provided an early release of the triethyl phosphate due to its low melting point.[84]

2.6.4 Capacity decay and microcapsules

Capacity decay or the change in the state of health (SoH) of a battery is influenced by several factors that can occur in the battery or its system over the lifetime in application. In a simplistic way, the life expectancy of a battery relates to the number of capacity cycles that can be obtained at a specified depth of discharge (DoD) which is the battery's capacity that has been dissipated over that specific DoD. This is usually done under controlled conditions of a specific current rate and set temperature, which often differs from the battery in application. Some of the more common factors which lead to capacity decay include the changes in the surface area and porosity of the electrodes over time. These include the growth of the solid electrolyte interphase (SEI) primarily at the anode, loss of the active material to current collector interphase, mechanical stresses, lithium plating and electrolyte decay. Watanabe *et al*. (2014)[85] reported on some of the main factors that contribute to capacity fading in batteries and are strongly dependent on the temperature, the current rates, and the change in DoD. In their study they reported on the formation of microcracks that formed on the lithium cobalt aluminium oxide (NCA) electrode which affects the amount of surface area available for lithium-ion intercalation to take place. The most common anode material is activated carbon (AC) and Eleri *et al*. (2023)[86] showed in their work the effects of electrolyte degradation on the AC material and how it related to the capacity fading of the cell. Different electrochemical states of AC were studied, and it was shown that the PF_6 anion in the electrolyte would deposit onto the electrode surface which in turn reduces the available surface area, increasing the internal resistance and hence reduces the lithium-ion intercalation ability and its availability.

Different types of encapsulated materials have been researched to improve the capacity retention of the LIB. For these purposes it is important that the capsules are highly porous to allow for the migration of lithium ions in and out of the shell and to interact with encapsulated active material. Yu et al. (2000)[87] explored the idea of encapsulating graphite with Nickel composites to prevent irreversible capacity loss during the first few capacity cycling after formation. The results showed that up to 10 wt% of the encapsulated active material improved the initial charge and discharge efficiency from 59% to 84% respectively. Tin as a potential anode additive was investigated by Han et al. (2020)[88] and they showed that if tin is directly incorporated into the anode material, the cell's discharge and charge capability decreases significantly due to increased volume expansion during the lithiation and de-lithiation reaction process. Their work explored the encapsulation of tin as "nanoflowers" using nanotubes as the shell material. This resulted in a decrease of the capacity decay during cycling where the voids of the microcapsules provided enough space for the volume expansion to occur without damaging the anode active material.[88]

The use of transition metals as possible anode materials in LIB's have shown to have significantly higher theoretical capacities relative to the use of carbonaceous anodes. However, the main issue with most transition metal anodes is their large volume expansion that occurs during the lithiation and de-lithiation reaction during the charging and discharging reaction thereby resulting in significant capacity loss during cycling.[25] Also, most of the transition materials have poorer conductivity when compared to carbonaceous anodes. Alternative synthesis schemes of the active material have been proposed to include some form of novel encapsulation techniques. Liu *et al*. (2021)[26] discussed the fabrication of SnS_2 quantum dots as shell material to

encapsulate Cu_9S_5 “nanoflowers” using a flow focusing device. The shells produced were highly porous to allow for high electrolyte penetration and the voids were big enough to allow for significant volume expansion without faulting or damaging the anode material. The use of the capsules improved utilization of active material and improved conductivity with an increase in electrochemical capacity. Fe_2O_3 has also been explored as potential anode material but suffers from capacity decay during cycling. Wu *et al* (2021)[89] in their research found that encapsulating Fe_2O_3 using zinc “nanoflowers” allowed the active material to deal with the charge induced stressors due to the porous nature and availability of free space in the capsules. Encapsulating Fe_2O_3 improved both the cycling performance and the conductivity of the active material. The use of phosphorous and nitrogen dual doped nano carbon capsules (PNCCs) have also been shown to improve electrochemical properties of iron-based anodes as they create more active sites for lithium intercalation.[90] The formed Fe (PNCCs) has a comparatively higher charge and discharge capacity when compared to graphite anodes.[90] A Ga-Sn liquid encapsulated alloy was shown to improve the self-healing capabilities of the active material in a cell.[27] Similarly, urea capsules were used to encapsulate Ga-Sn liquid alloy material that accommodated the volume expansion without altering the anode material properties and exhibited a capacity of 711.6 $mAhg^{-1}$ after 500 cycles.[27] Silicon, like the transition metals, has a high theoretical capacity when used in LIB’s. However, it suffers from poor electrical conductivity, short life-cycling and capacity decay because of the large volume expansion during lithiation and de-lithiation reactions.[91] The material can be effectively used as an anode material with the aid of encapsulation to optimise its performance. Yang *et al* (2015)[91] explored the option of encapsulating silicon with carbon to counter the volume expansion problem. The capsules formed were porous enough to allow

the free transport of lithium ions in and out of the shell and showed that after 400 cycles the cells still had 78.6% capacity retention. Similar to the carbon encapsulated silicon, Si-Al/Al-MOF was used where MOF was a molecular organic framework of aluminium capsules that reduced the effects of volume expansion during lithiation and de-lithiation reactions. The work by Wang *et al* (2019)[92] showed that these capsules also increased the conductivity of the active material and showed a capacity retention of 79% after 500 cycles. In other studies, zeolitic imidazolate frameworks 90 with a coating of a covalent-organic framework were explored to encapsulate silicon. The porous cages that formed improved the electrical conductivity on the surface of the microcapsules and showed a coulombic efficiency of more than 99%.[93] Yang *et al*. (2018)[6] reported a 92.4% capacity retention after 200 cycles while Ma *et al* (2018)[75] and Lou *et al* (2022)[66] reported 93% and 95% capacity retention after 200 and 100 cycles respectively.

3: Experimental

3.1 Materials and Reagents

This is the list of all the chemicals used for microencapsulation, preparation of cathode material and coin cells. No further purification was done for all the chemicals used.

Table 3.1: List of materials used in the study.

Reaction or Process	Reagent	Specifications	Role	Supplier
PUF synthesis	Urea	99.5%	PUF shell monomer	MINEMA laboratories
	Formaldehyde	37-41%	PUF shell monomer	Sigma Aldrich
	Ammonium chloride	99%	Initiator	Associated chemicals
	Resorcinol	99%	Initiator	ExtraPore AR, Exiplus
	Triethanolamine	98.9%	pH adjustment	Merck
	Hydrochloric Acid	37% (w/v)	pH adjustment	Sigma Aldrich
	Acetone	99.5%	Rinsing solvent	Sigma Aldrich
PMMA synthesis	PMMA	99.9%	PMMA shell	Sigma Aldrich
	Acetone	99.5%	Solvent	Sigma Aldrich
	PVA	87-97% 30000-70000 mol wt	Stabilizer	Sigma Aldrich
	SDS		Emulsifier	FunwithSoap
Additives	Cyclohexylamine	99%	Additive	Acros Organics
	Dicyclohexylamine	98%	Additive	Fluka
	Benzylamine	99%	Additive	Merck
	Diphenylamine	99%	Additive	Merck
	Diethylamine		Additive	RadChem
	Ethanediol	99.5%	Additive	AnalaR
	1,5-Pentanediol	97%	Additive	Sigma Aldrich
	1,2-Propanediol	99%	Additive	SRL Chemicals
			Additive	
Cathode material fabrication	Commercial LFP	99%	Cathode	Shandong Gelon LIB Co
	Carbon Black	N110	Supporting matrix	Orion Engineering
	Polyvinylidene fluoride	99%	Binder	Sigma Aldrich
	N-methyl pyrrolidinone, anhydrous	99.5%	Liquid phase	Sigma aldrich
	Aluminum sheet	Battery grade	Current collector	Shandong Gelon LIB Co
Coin cell assembly	$LiPF_6$ salt	99.9%	Electrolyte	Sigma Aldrich
	Lithium	99.9%	Anode	Sigma Aldrich
	Diethylene carbonate	99%	Electrolyte	Sigma Aldrich
	Dimethylene carbonate	99%	Electrolyte	Sigma aldrich
	$LiPF_6$ electrolyte (1:1:1) (DMC:EC: DEC)	99.9%	Electrolyte	Sigma aldrich
	C220 coin cells	-	Cover	Shandong Gelon LIB Co
	Polyethylene sheet	-	Separator	-

3.2 Methodology

3.2.1 Feasibility tests

This experimental section was split into 3 major areas:

I. All possible additives (10% v/v) mentioned in **Figure 3.1** were added to the electrolyte (1M $LiPF_6$ in DMC: EC: DEC (1:1:1) and were subjected to 10 minutes of heating at 200 ^oC and thereafter physical appearances were captured.

II. The resistance of the electrolyte was measured at room temperature and pressure, thereafter the solution was heated at 200 ^oC for 10 minutes and allowed to cool, then the resistance value was noted. The resistance values of the solutions made after addition of each respective additives were also noted before and after heating up.

III. The additives which in turn produced the highest resistance values upon the heat-cool cycle were then encapsulated for use in LIB coin cell as shown in **Figure 3.1.**

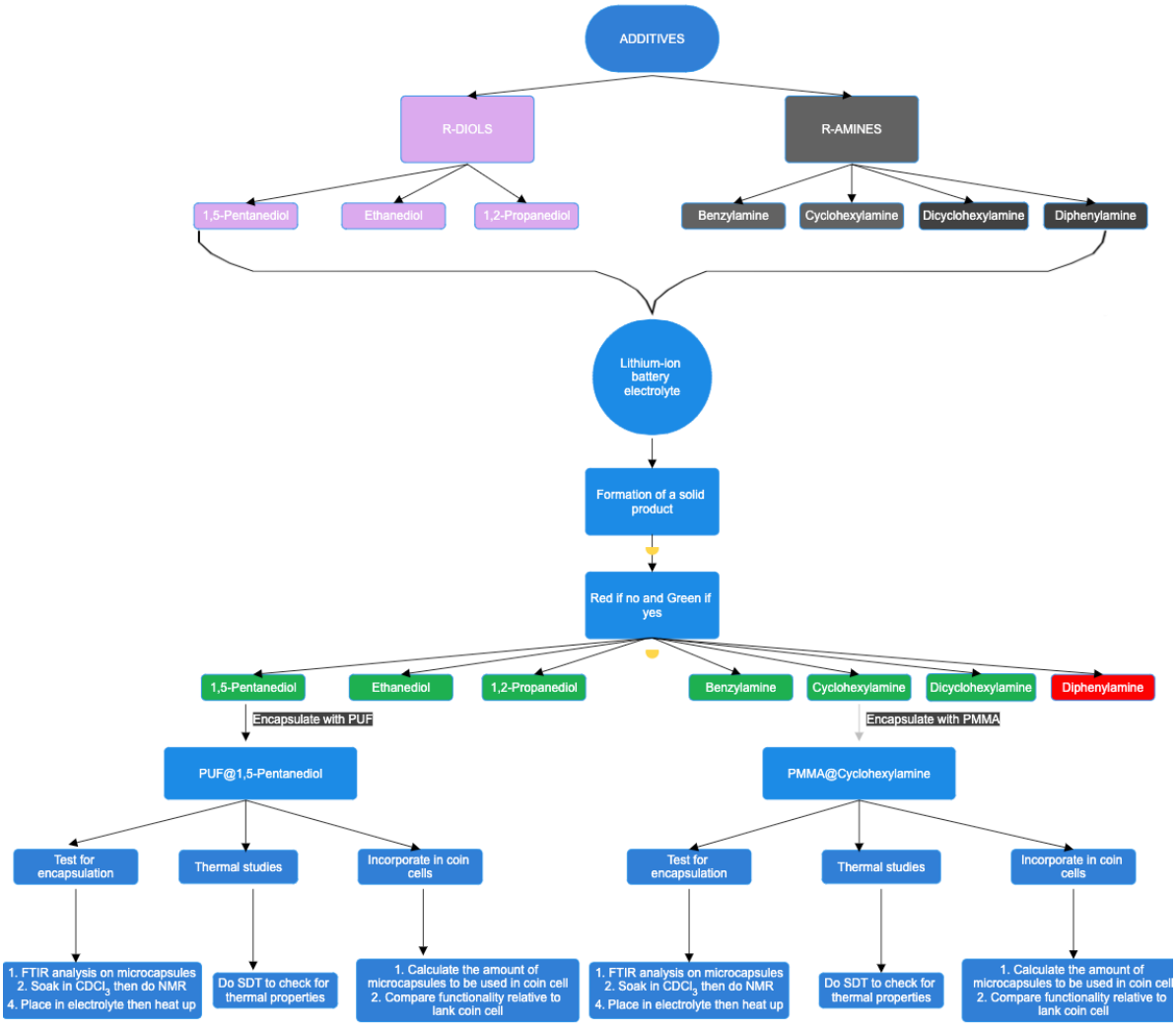

Figure 3.1: Overview of steps carried from feasibility studies to coin cell fabrication.

3.2.2 Impendence spectroscopy (EIS) to monitor the change in ionic conductivity.

All the shown additives in **Figure 3.1** are meant to react with the electrolyte to form a gel like barrier to stop ion transfer from anode to cathode. This was done by using two platinum wires as the counter and working electrode respectively. All the electrochemical cells were connected to a BioLogic SP-150 potentiostat. EIS measurements were performed before the reaction began and after the reagents were subjected to 200 ^{o}C heat for 10 minutes, cooled thereafter, with

an AC voltage of 40 mV and the frequencies between 20 kHz to 50 Hz (**Figure 3.2**).

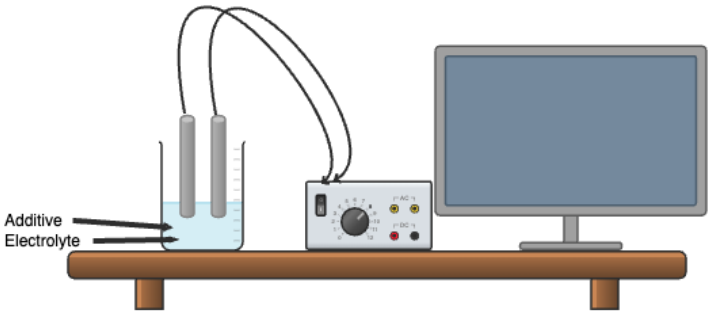

Figure 3.2: Set-up used to measure ionic conductivity using an EIS method before the reaction commenced and after reaction was complete.

3.2.3 Encapsulation of additives using either PMMA or PUF as the polymeric shell.

Due to the performance of cyclohexylamine and 1,5-pentanediol when EIS measurements were performed, both were encapsulated using PMMA and PUF respectively. Cyclohexylamine was encapsulated using PMMA only since the PUF encapsulation led to production of fumes and incomplete encapsulation due to its reactivity towards the urea-formaldehyde prepolymer. 1,5-Pentanediol was encapsulated using PUF.

PMMA – Only R-amines (cyclohexylamine) were encapsulated using a PMMA shell using a solvent evaporation method. PMMA (25 g) pellets were dissolved in acetone (1000 mL) and were mixed overnight until the PMMA pellets were completely dissolved. Aqueous solution of 1% wt. polyvinyl alcohol (PVA) was added as a stabilizer using a constant volume of 10 mL and 1 g of sodium dodecyl sulphate (SDS) was used to precoat cyclohexylamine. To various ratios

of PMMA: cyclohexylamine (material to be encapsulated) were studied. These were 1:1, 2:1 and 3:1 (g) respectively. **Figure 3.3** depicts the method graphically and different sized microcapsules were synthesized at various stirring rates of 200 rpms, 400 rpms, 600 rpms, 800 rpms and 1000 rpms respectively. In order to check the effectiveness of the SDS precoating, 2 samples were prepared (Blank SDS and SDS coated cyclohexylamine) and were added to LIB electrolyte and subjected to 200 ^{o}C for ten minutes. The gelling effect was still observed in the sample with the cyclohexylamine. This concludes that the cyclohexylamine with the SDS was still effective.

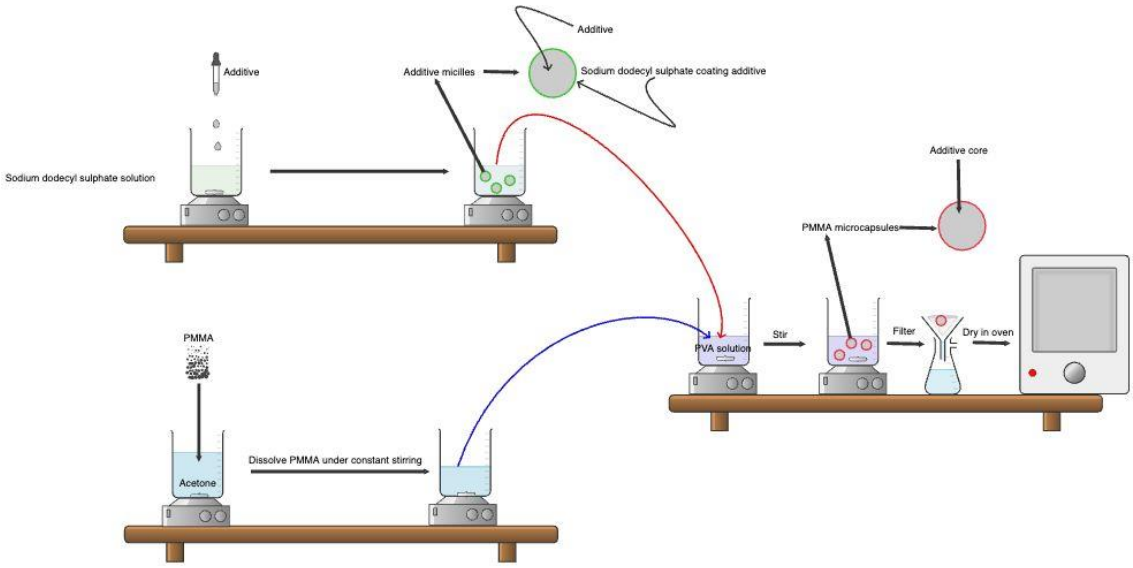

Figure 3.3: Encapsulation of cyclohexylamine using PMMA.

PUF - Microcapsules were prepared by *in situ* polymerization in an oil-in-water emulsion. 1,5-Pentanediol precoated in 1 g of sodium dodecyl sulphate was microencapsulated, **Figure 3.4** schematically shows the process of microencapsulation. Initially, urea (0.5 g, 0.08325 mol) and formaldehyde (1.12 g, 0.3363 mol) were dissolved in 10 mL of de-ionized water. The pH of the solution was adjusted to 9 by the addition of triethanolamine. Alkaline pH prevents crosslinking of

the urea-formaldehyde prepolymer before the addition of 1,5-pentanediol. Once the 1,5-pentanediol was added, after about 30 minutes, the activators of resorcinol (0.05 g) and ammonium chloride (0.05 g) were introduced sequentially. The pH was then adjusted to 3 to promote crosslinking to form the microcapsules. An initial study was done to make microcapsules of different sizes by varying the stirring rates range from 200 rpms, 400 rpms, 600 rpms, 800 rpms and 1000 rpms respectively. This was done in order to obtain an ideal inner volume to size ratio that will allow the active ingredient to be encapsulated. Similar to the previous sample, the effect of the SDS precoat on the 1,5 pentanediol was done by preparing 2 samples (Blank SDS and SDS coated 1,5-pentanediol). These were added to LIB electrolyte and were subjected to 200 ^{o}C for 10 minutes. Gelling was again observed for the sample with the 1,5-pentanediol showing that the SDS had limited effect on the effect.

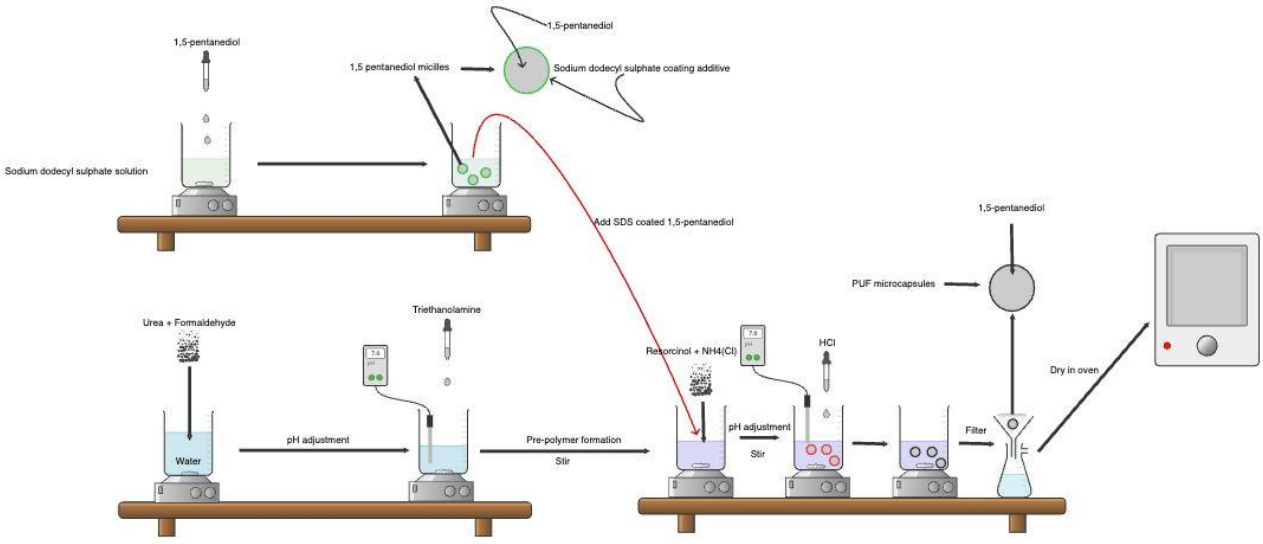

Figure 3.4: Encapsulation of 1,5-pentanediol using PUF.

3.2.4 Fourier transform infrared spectroscopy (FTIR)

FTIR is an analysis technique that determines infrared shifts that are emitted or absorbed when a solid, liquid, or gaseous sample is subjected to a wide variety of wavelengths in the infrared spectrum. This can act as a “fingerprint” identification

technique were all chemicals have a unique absorption and emission spectra, due to their vibrational and rotational motions of their constituent atoms and bonds. The analysis was carried out using a Bruker Tensor 27 FTIR spectrophotometer that was fitted with a platinum Attenuated Total Reflectance (ATR). Samples were placed on diamond reflectance screen and the scan range was 400 cm^{-1} to 4000 cm^{-1}.

3.2.5 Simultaneous DSC-TGA-FTIR (SDT-FTIR)

Simultaneous DSC-TGA-FTIR refers to thermal analysis where differential scanning calorimetry (DSC), thermal gravimetric analysis (TGA) and Fourier transform infrared spectroscopy (FTIR) are measured simultaneously as a sample is subjected to a heating procedure. TGA determines a sample's weight changes in response to an increase in temperature over time. TGA is useful for measuring a wide range of material characteristics that include volatile contents, moisture content, multi-component composition, thermal and oxidative stability, and decomposition rates. DSC is a technique that measures the temperature differential between the sample and reference as a function of the change in temperature over time. It can be used when assessing material properties such as glass transition (Tg) temperature, melting points, crystallization, desorption, polymorphism, polymerization, vaporization, curing, and decomposition. A Perkin Elmer SDT was utilized in this investigation to gauge the melting and decomposition points of PUF and PMMA microcapsules.

3.2.6 Lithium-ion battery coin cell fabrication

A graphical representation of the procedure used to make the cathode electrode for coin cells is shown in **Figure 3.5**.

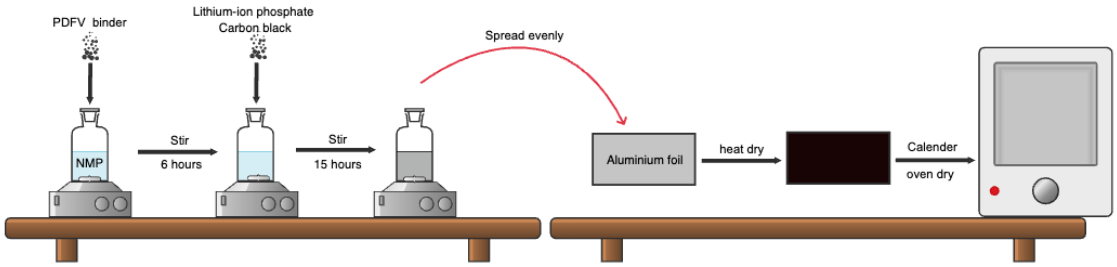

Figure 3.5: Schematic showing the procedure to make the LFP cathode.

Commercial Lithium Iron Phosphate (LFP) material was used as a cathode material. The cathode material (85% w/w) was pre-mixed with carbon black (7.5% w/w) using a stirrer bar for 90 minutes. The PVDF binder (7.5%) was pre-dissolved in n-methyl pyrrolidinone (NMP) by stirring at 1000rpms for 6 hours. LFP and carbon black powder mixture was then added to the PVDF solution and mixed at 1000rpms for 15 hours. Battery grade aluminium foil was placed onto a clean glass surface that was pre-cleaned using acetone and NMP. Two pieces of tape on each side of the foil were used to hold it in position and control the amount of paste being cast on the aluminium foil using a razor blade to achieve an average of 120 µm coating thickness. The coated foil was dried on the hotplate (90 °C) to evaporate the NMP solvent. Final drying was done in the oven overnight (105 °C) before being kept in a desiccator for further processing. The 16 mm diameter coated disks (Al_{co}) were punched using a hollow puncher and were subsequently weighed. Referenced uncoated disk (Al_{ref}) were also punched out and weighed. These weights are used to calculate the final mass of the coated material (M_{co}). The weight of active electrode material was 85% of the cathode material (M_{active}), and by using the theoretical specific capacity (C_{ts}), the current (C_{Am}) used for charging and discharging was obtained. The typical calculation procedure used is shown below.

Calculations:

a) Mass of coating $M_{co}(g) = Al_{co} - Al_{ref}$

b) Mass of active material $M_{active}(g) = M_{co}(g) \times 0.85$

c) Capacity $M_{active}(g) \times C_{ts}\left(\frac{mAh}{g}\right) = \text{capacity } (mAh)$

d) C rate $\text{capacity } (mAh) \div t(h) = C_{Am}(mA)$

I. The anode was prepared as shown in **Figure 3.6**

Figure 3.6: Compression of lithium metal onto a stainless steel spacer

In the Argon filled glove box, the lithium metal was rolled onto a stainless-steel spacer using a cylindrical Al roller. This was to ensure that the lithium metal adheres properly to the current collector and any surface impurities or discolouration of the lithium foil was removed prior to assembling into the coin cell holder.

II. The coin cell assembling procedure in the glove box can be summarized as shown in **Figure 3.7**.

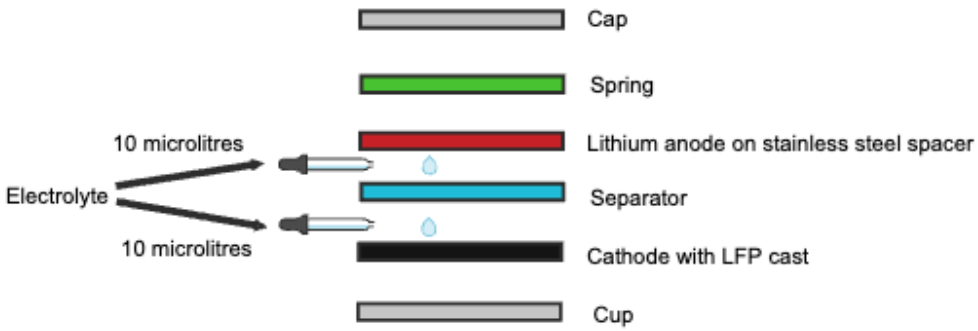

Figure 3.7: Li-Coin cell building sequence.

The cathode material was cut using a 16 mm puncher and was placed into the cup (top cap) (aluminium side down) thereafter 10 µL of electrolyte was spritz on top of the cathode. A separator (polyethylene sheet) was then placed on top and another 10 microlitres of electrolyte was spritzed on top followed by lithium on spacer (lithium side down), spring and cap with O-ring attached. Lastly the coin cell was cramped using a hydraulic crimper. For coin cells that were made with microcapsules, 0.001g which was approximately 10% (w/w) of the microcapsules with the respective active were pre-mixed with the electrolyte before their addition to the coin cell.

3.2.7 Lithium-ion battery coin cell discharge-charge cycling

The discharge-charge of the assembled coin cell was done by applying a constant current rate while observing the specified potential limits of 4.2 V for the charge and 3.0 V for the discharge respectively. For this study, an Arbin battery tester BT1000 multichannel coin cell tester was utilized to conduct charge and discharge cycles at different current rates (0.1 C, 0.2 C, 0.5 C, 1 C, 2 C, and 5 C) respectively. The rate used was based on the theoretical capacity of 170 mAh/g of the active cathode material.

3.2.8 Lithium-ion battery coin cell voltage test to determine effectiveness of additives

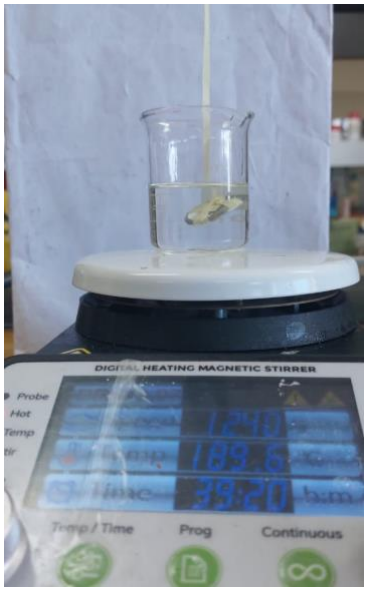

Figure 3.8: Additive effectiveness test.

Coin cells were submerged in mineral oil and heated up to 300 ^{o}C for about 10 minutes and thereafter the voltage of each cell was measured. All coin cells had a starting voltage of 3.3 ± 0.9 V.

3.2.9 EIS on Lithium-ion battery coin cell before and after discharge-charge cycling

The Electrochemical Impedance Spectroscopy (EIS) technique stands as a crucial method for characterizing electrochemical systems by assessing their impedance and conductivity. This method involves subjecting the electrochemically active sample to an alternating current (AC) potential covering a wide frequency range.[94] Recordings of voltage or current are made corresponding to the system's response. To interpret the gathered data effectively, an equivalent circuit model is used to model the response accordingly, **Figure 3.9 (a)**. EIS assessments typically employ an AC current of 10 mA across frequencies spanning from 0.1 Hz to 1 MHz. The outcome obtained from these tests is referred to as impedance (Z) and represented as Bode or Nyquist plots respectively. In the Nyquist plot, the y-axis represents the negative of the imaginary impedance component, while the x-axis displays the real component at varying

frequencies.[95] This plot is well described in literature and typically comprises one or more semi-circles at the high frequencies and is graphically shown **Figure 3.9 (b)** with a typical single Randel's model.[94] In this study a Biologic Science VMPS potentiostat was used in conjunction with the EC-Lab Express software.

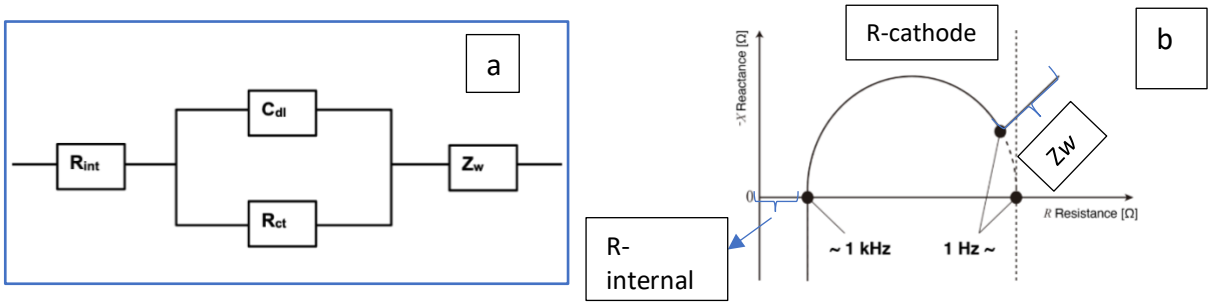

Figure 3.9: (a) Electrical Equivalent Circuit (EEC) used to fit the EIS data; **(b)** An ideal EIS Nyquist spectrum for a typical Li-ion battery system.

The R-internal (Rint) denotes the internal resistance, encompassing elements like the separator, electrolyte, and additives. R-cathode (Rct) signifies the resistance stemming from charge transfer within the cathode electrode. In typical Li-ion cells with graphite anodes, the semi-circle often represents both cathode and anode. However, in this study, a single semicircle was observed at high frequencies.[96] This occurrence was due to the use of lithium metal—an anode with excess lithium—resulting in minimal resistance influence from the anode compared to the cathode part of the cell electrode.[96]

4: Results and Discussion

Different R-amines and R-diols were reacted at 200 °C with lithium-ion battery electrolyte (1M $LiPF_6$ in DMC:EC:EMC (1:1:1)) for 10 minutes to see if any solid product was formed. Literature reported that these additives would hamper the ionic conductivity within the electrolyte and increase their resistivity.[58] Noelle *et al* (2018)[58] showed that R-amines predominantly react with EMC in a ring opening fashion to form carbamate derivatives as shown in **Figure 4.1**.

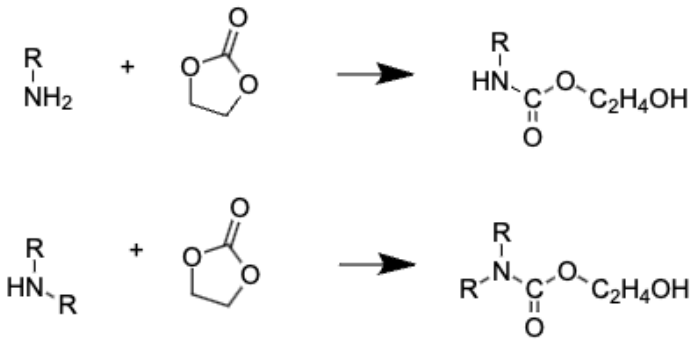

Figure 4.1: EMC ring opening reaction with R-amines to form carbamate derivatives.[58,97,98]

The best performing R-amines and R-diols were then encapsulated and added to the electrolyte in a lithium-ion coin cell to evaluate their influence on the cell's electrochemical performance and to observe its effectiveness in a high temperature application. This chapter summarizes the characterization and analysis done before and after either R-amines or R-diols were microencapsulated.

4.1 Range of R-amines and R-diols and their feasibility

The R-amines and R-diols chosen in the study are summarized in **Table 4.1.** They were chosen based in their reactivity already described in literature and availability.

Table 4.1: Chemical structures of chemicals used in the experiment.

Compound	Structure	Comment
Cyclohexylamine	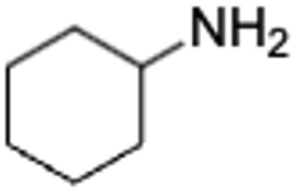	No literature on its use as an additive has been reported. Reasoning is based on experiments done by Shi *et al* (2016),[97] Noelle *et al* (2018),[58] Shi *et al* (2016).[98]
Dicyclohexylamine	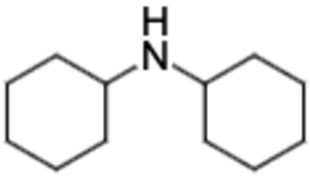	No literature on its use as an additive has been reported. Reasoning is based on experiments done by Shi *et al* (2016),[97] Noelle *et al* (2018),[58] Shi *et al* (2016).[98]
Benzylamine	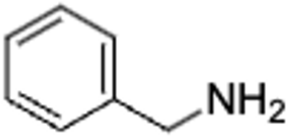	Its use as an additive is based of experiments done by Shi *et al* (2016).[98]
Ethanediol	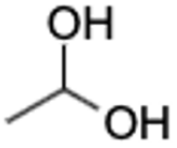	Its use as an additive is based on experiments done by Noelle et al (2018). [58]
1,2-Propanediol	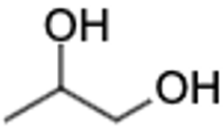	Its use as an additive is based on experiments done by Noelle et al (2018). [58]
1,5-Pentanediol		Its use as an additive is based on experiments done by Noelle et al (2018). [58]

A flow diagram to describe the process of selecting the most suitable additive for encapsulation is shown Figure **4.2.** All six additives named in **Table 4.1** were reacted with LIB electrolyte containing EC, EMC, and DMC in a 1:1:1 ratio. Literature states that these additives only react with EMC with $LiPF_6$ acting as a catalyst.[58,97,98]

The results showed that only the dicyclohexylamine failed to produce a gel or solid-like product over the exposure time and reaction temperature. For this study, the most

suitable active additive was the one that showed the quickest reaction to form a stable barrier to prevent the ion conductivity and internal short circuit within the cell.

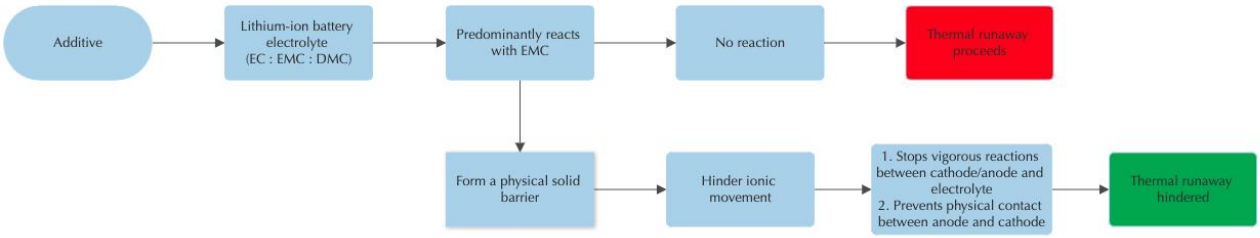

Figure 4.2: R-diols and R-amines reaction pathways to prevent ionic movement (all experiments involved use of 10% v/v additive to electrolyte).

To ensure that no additional external factors affected the reaction of the electrolyte and R-amine or R-diol used, the mixture was prepared in a closed vial in the glove box and then taken outside for further heating. Out of all the reagents used, cyclohexylamine showed to have the fastest time to turn from a liquid to a uniform gel in less than 3 minutes. Compound 1,5-Pentadiol showed to be the second-best performing reagent with the electrolyte to form an initial heavy gelling type substance around the reaction vial walls within the first 5 minutes. The other reagents showed little, or no reaction products formed that remained predominantly in a liquid state within the vial. A visual representation of the various liquid forms of the reagents before and after the solution was exposed to 200^{o}C for more than 5 minutes is summarized in **Table 4.2** respectively.

Table 4.2: Physical appearance of reaction products formed after each additive was added to some lithium-ion battery electrolyte, followed by heating the mixture to 200°C. *All vials to the left have unreacted lithium-ion battery electrolyte in them

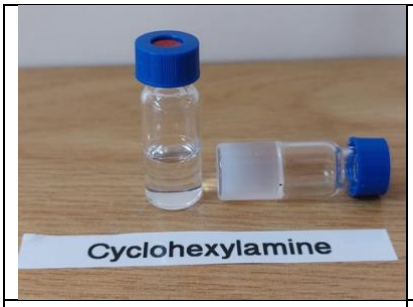		
Cyclohexylamine formed a completely gel like product which suggests it might have reacted with all three electrolyte components (EC, EMC and DMC)	Dicyclohexylamine produced a semi-solid aggregates within the electrolyte implying that it might only have reacted with EMC based on mode of action of amines. [58,98]	Benzylamine produced a semi-solid aggregate within the electrolyte implying that it only reacted with the the EMC based on mode of action of amines. [58,98]
		
1,2-Pentanediol produced a gel coating around the inside walls of the reaction vial with some liquid from on the electrolyte still remaining. This implies that it only reacted with some of the components such as EMC as suggested in literature.[58,97,98]	1,2-Propanediol produced a gel coating around the inside walls of the reaction vial with some liquid from the electrolyte in the middle still remaining. This implies that some components such as EMC.[58,97,98]	Ethanediol formed a thin film around the inside walls of the reaction vial with some liquid from the electrolyte still remaining. This implies that it possibly only reacted with EMC as suggested in literature.[58,97,98]

4.1.2 Ionic conductivity of electrolytes with or without additive before and after the reaction

The amount of electrolyte that was available for experiments was little so a conductivity measurement was done only on blank electrolyte with an average of 6.71 mS/cm, which is in the range of previously reported conductivity values ranging from 4.00-11

mS/cm.[54] In order to study to which the extent the additive reaction with the electrolyte has on the ion conductivity of the solutions before and after reaction were done, EIS was used to measure the change in the resistance of each of the additives added to the electrolyte that then relates to the ion conductivity of the final solution and the results are summarized in **Figure 4.3** and **Table 4.3**. In general, the addition of non-conducting chemicals to the electrolyte would result in a decrease of ionic movement. A decrease in the ionic movement should be directly proportional to amount of non-conducting chemicals added. However, the study showed that some of the additives resulted in an increase in the ionic conductivity upon addition to the electrolyte. A 10% v/v of additive was added to the electrolyte and EIS was performed. The 10% v/v of additive was then reacted with the electrolyte at 200 °C, and the reaction product was allowed to cool down and then EIS was performed. To measure conductivity using EIS, the resistance of the electrolyte and electrolyte + additive systems were measured, and data obtained was used to convert resistance values to specific conductivity given that blank electrolyte had an average conductivity of 6.71 mS/cm:

$$Conductance(G) = \frac{1}{Resistance} \quad \text{Eq 4.1}$$

$$Specific\ Conductivity = Conductance \times Ionic\ conductivity \quad \text{Eq 4.2}$$

Figure 4.3 fitting model chosen because it explains interference behavior where the capacitance shows how the platinum electrodes interact with the electrolyte and frequency-dependent behavior where the properties of the electrolyte are studied over a wide frequency range.

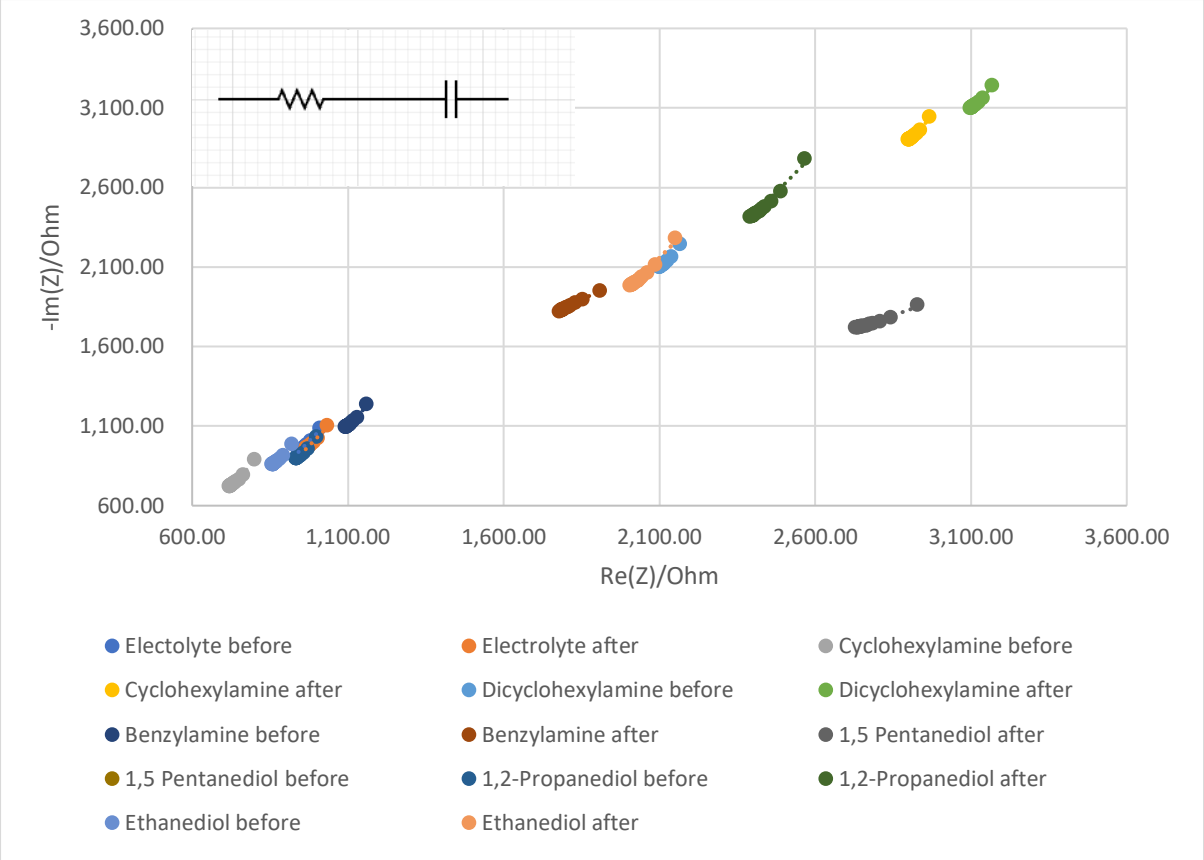

Figure 4.3: Nyquist plots for 10% v/v additives in electrolyte before and after reacting with the equivalent circuit fit.

Table 4.3: EIS data for 10% v/v additives in electrolyte before and after reacting.

Sample	R before (Ω)	R after (Ω)	G before (S) x 10^{-3}	G after (S) x 10^{-3}	Absolute conductivity before (mS/cm)	Absolute conductivity after (mS/cm)
Electrolyte	941	949	1.062	1.054	7.13	7.07
Cyclohexylamine	744	2900	1.344	0.345	9.02	2.32
Dicyclohexylamine	2001	3100	0.499	0.323	3.35	2.17
Benzylamine	1094	1807	0.914	0.553	6.14	3.71
1,5-Pentanediol	1700	2600	0.588	0.385	3.94	2.58
1,2-Pentanediol	935	2430	1.070	0.411	7.18	2.76
Ethanediol	860	2230	1.163	0.448	7.80	3.00

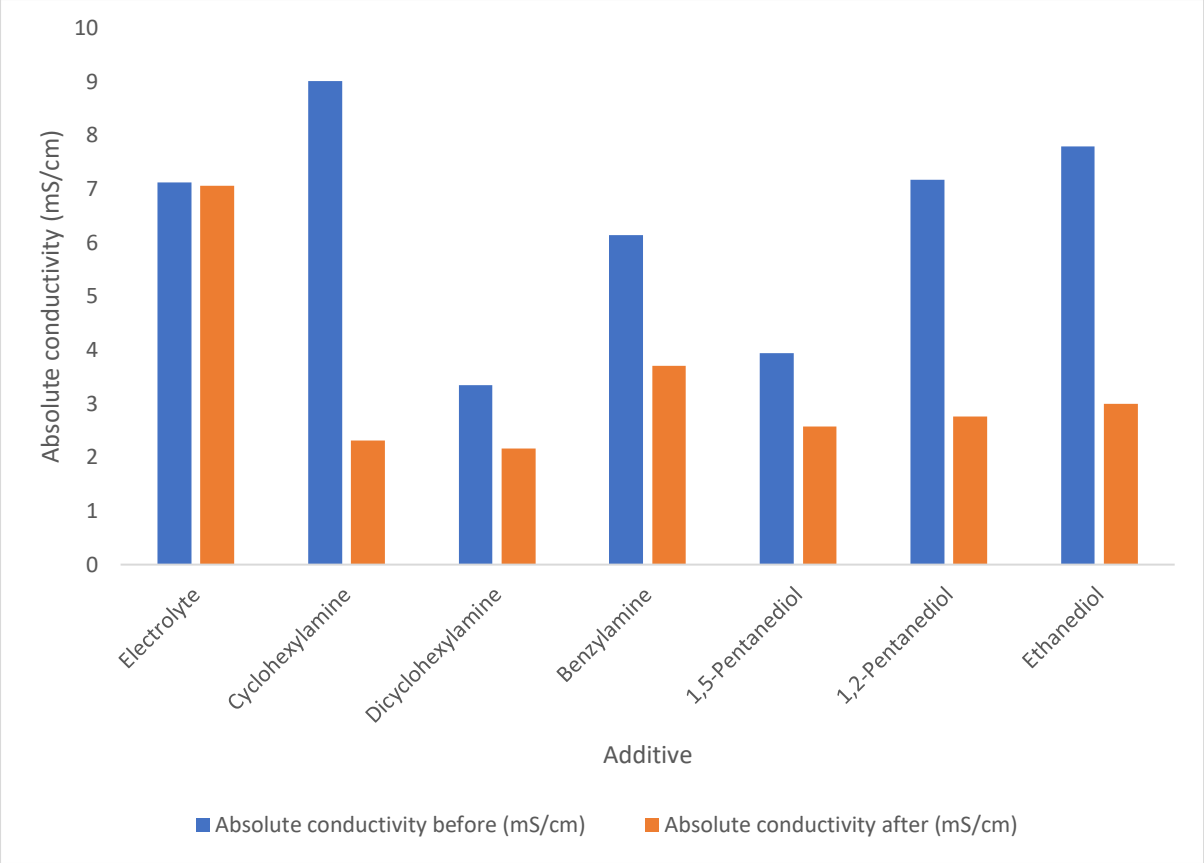

Figure 4.4: Effects of heat on the conductivity of each electrolyte system.

Using the $R_{internal}$ data obtained from AC EIS resistance measurements, the specific conductivity was obtained (**Figure 4.4**). The electrolyte only solution showed a slight decrease in absolute conductivity from 7.31 to 7.07 mS/cm after heating to 200°C for 10 minutes respectively. The slight difference is insignificant to deduce that heat had an effect on the conductivity of the electrolyte solution.

Cyclohexylamine when added to the electrolyte before heating showed an initial increase in conductivity within the system from 7.13 mS/cm (blank electrolyte) to 9.02 mS/cm (electrolyte + cyclohexylamine before heating) meaning that cyclohexylamine might improve ionic movement in the electrolyte. After heating the specific conductivity dropped to 2.23 mS/cm, and the significant drop in specific conductivity after heating

suggests that cyclohexylamine might undergo chemical changes or decomposition when exposed to heat. This alteration in its molecular structure could lead to reduced conductivity or increased impedance.

Similar to cyclohexylamine, di-cyclohexylamine also shows drop in specific conductivity after heating, though not as dramatic. This indicates that it might be less affected by heat compared to cyclohexylamine. Effects of di-cyclohexylamine on specific conductivity were seen as soon as it was added to the electrolyte solution, comparing it to the blank electrolyte with a conductivity of 7.13 mS/cm.

Benzylamine exhibits a moderate increase in resistance after heating, suggesting that its conductivity might be slightly affected by thermal stress, but not to the same extent seen in cyclohexylamine. The addition of benzylamine affected the conductivity of the electrolyte system dropping the conductivity from 7.13 mS/cm to 6.14 mS/cm before reaction and to 3.71 mS/cm after reaction.

Similar to di-cyclohexylamine, 1,5-pentanediol shows a notable increase in resistance after heating, indicating that its electrical properties are also impacted by thermal stress, dropping the ionic conductivity to a mere 2.58 mS/cm. Compound 1,2-Propanediol displayed a substantial increase in resistance after heating, implying significant changes in its conductivity or molecular structure due to thermal effects. Ethanediol, like other additives, experienced a substantial increase in resistance after heating, indicating significant alterations in its electrical properties under thermal stress. Among the additives, cyclohexylamine and 1,5-pentanediol exhibited the most pronounced increase in resistance after heating, suggesting that these additives might be more susceptible to thermal degradation or structural changes, which coincides with the fact that both additives showed the most dramatic physical changes as seen

in **Table 4.1**. Di-cyclohexylamine, benzylamine, and ethanediol also showed notable increases in resistance, though comparatively less pronounced hence only cyclohexylamine and 1,5-pentanediol were selected for encapsulation.

4.2 Cyclohexylamine encapsulation

Encapsulation of cyclohexylamine with a PMMA shell was done by using a solvent evaporation method. Firstly, blank PMMA microcapsules were synthesized at different stirring rates to determine the most suitable size for the encapsulating of cyclohexylamine. In general, the microcapsule sizes reduced in size with increasing stirring rates. However, in some cases if the stirring rate is too low, irregular shaped spheres would form. At higher stirring rates some very small microcapsules would then form clusters. To study the physiological properties of microcapsules formed, SEM was used to measure the diameter of the microcapsules, assess their morphology, and determine successful formation.

Table 4.4: Summary of results showing relationship between stirring rates and microcapsules diameter

PMMA Samples	Stirring rate (rpms)	Capsule size range (μm)	Capsules formed
PMMA@200	200	No formation	None
PMMA@400	400	30.55 – 2.98	Spherical
PMMA@600	600	10.91 – 1.75	Spherical
PMMA@800	800	6.34 – 2.74	Spherical
PMMA@1000	1000	< 2.20	Spherical
Cyclohexylamine@PMMA	800	8.34 – 2.51	Spherical

Table 4.4 shows that PMMA@400 had a size distribution ranging from 30.55 – 2.98 µm. This supports the literature data which points out that low stirring rates forms uneven size distributions, and although the microcapsules had a wide array of sizes, most of the capsules were predominantly less than 10 µm in size. The results shown in **Figure 4.8** summarize the above-mentioned data by showing the mean size of the capsules for each stirring rate. [81]

4.2.1 Morphology of microcapsules using SEM

SEM is usually used to determine the sizes of very small particles and was used to analyze the morphology of synthesized microcapsules. The PMMA microcapsules were synthesized using the following stirring rates: 200, 400, 600, 800 and 1000 rpms and were named PMMA@200, PMMA@400, PMMA@600, PMMA@800 and PMMA@1000 respectively. **Figure 4.5** shows the appearance of the PMMA microcapsules when viewed using SEM.

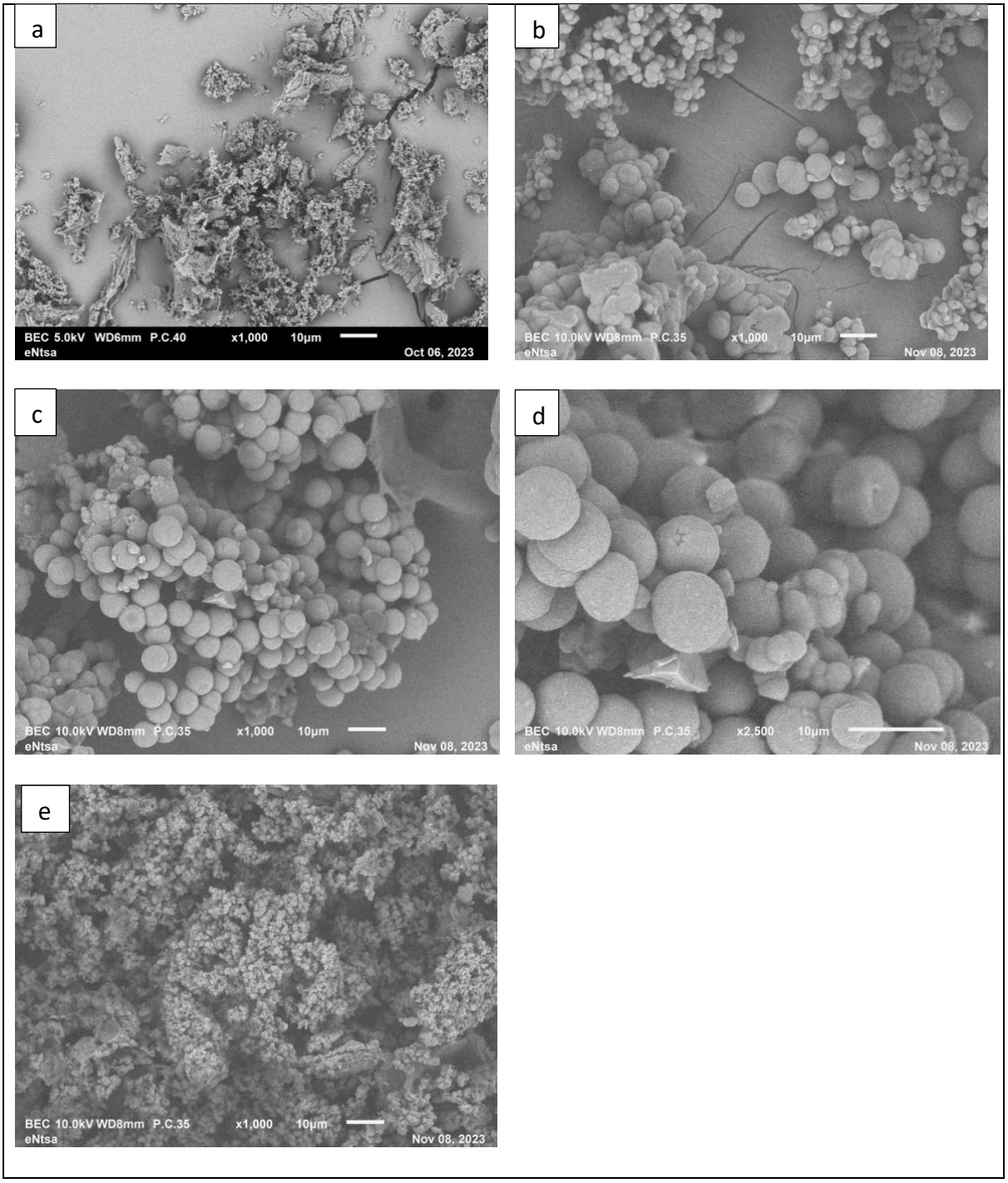

Figure 4.5: Capsules formed at different stirring rates.

* a, b, c, d and e represent PMMA@200, PMMA@400, PMMA@600, PMMA@800 and PMMA@1000 respectively.

4.2.2 Formation failure at low stirring rates

Cyclohexylamine microcapsules were synthesized at a stirring rate of 800 because capsules formed at that stirring rate showed a narrower size distribution range

compared to other stirring rates and named Cyclohexylamine@PMMA. Also, different parameters were used to synthesize Cyclohexylamine@PMMA microcapsules. Two different approaches were taken, the first approach included using the same amount of core (cyclohexylamine) and shell (PMMA) using a 1:1 ratio, and the second approach included using the same amount of core (cyclohexylamine) and shell (PMMA) using a 1:1 ratio but coating the core with sodium dodecyl sulphate first to prevent the core from interacting with the shell. **Figure 4.5a** showed that at low stirring rates (200rpms) no microcapsules were formed as there wasn't enough shear force to allow formation of droplets and poor stirring strength to allow even distribution of reagents which lead to formation of spherical shells hence the film like aggregates.

4.2.3 Clustering at high stirring rates

Figure 4.6 shows the clusters that are formed when making microcapsules at stirring rates =/> 1000rpms. Literature refers to some of the following factors that can attribute to this. These include: excessive shear force can lead to aggregation of microcapsules; high agitation can lead to droplet collisions and unstable emulsions can be formed due to excessive energy the droplets cannot handle[99–101].

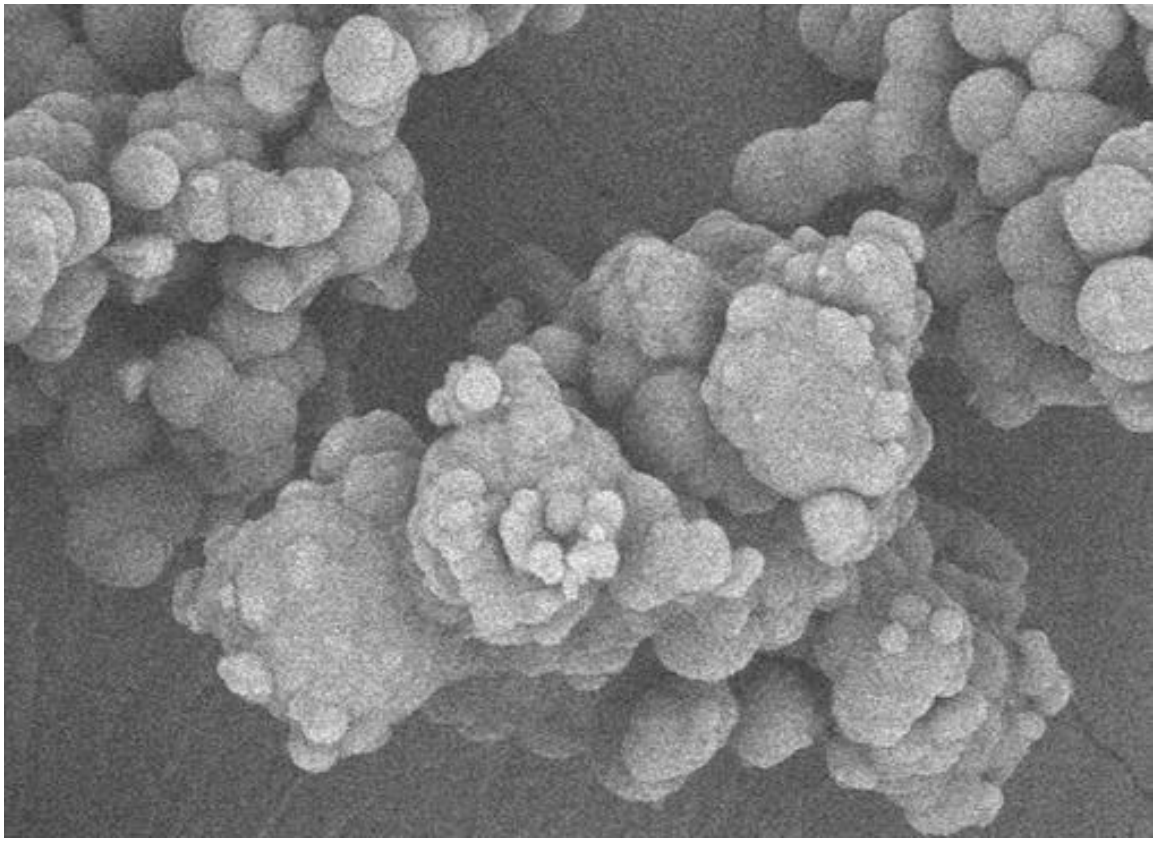

Figure 4.6: Clusters formed at high stirring rates (1000rpms)

4.2.4 Size distribution of blank microcapsules

When making microcapsules, stirring rates are important and directly correlate to the size distribution of the microcapsules formed. Low stirring promotes formation of capsules of different sizes due to the uneven distribution of the shear force while higher stirring rates allow a narrower size distribution due to the even distribution of the shear force required to form droplets. SEM was used to measure the size distribution of the microcapsules.

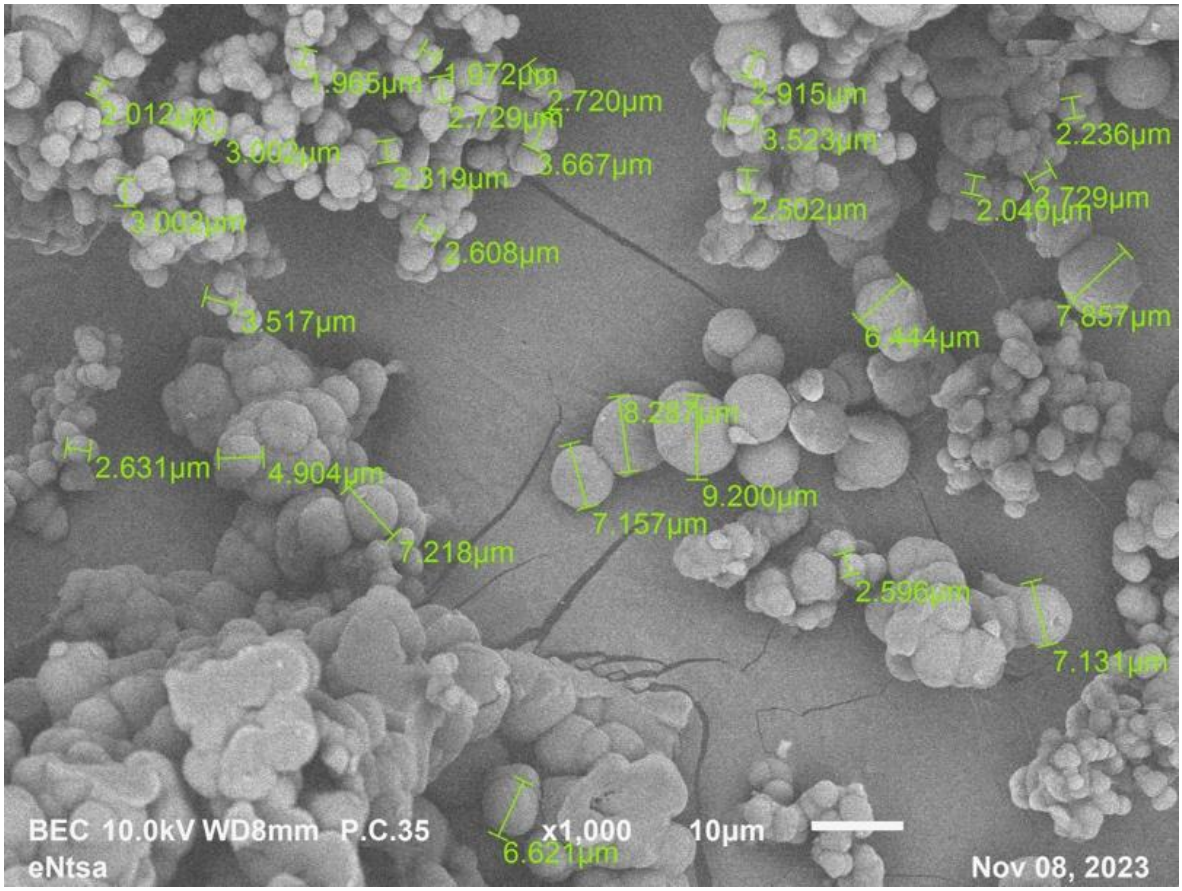

Figure 4.7: SEM image showing how microcapsules diameter size is measured (PMMA@400).

Figure 4.7 depicts the typical measurements taken to determine the average microcapsule diameters. This was done for all samples where multiple zones were imaged for each sample to get enough data to do statistical analysis as shown in **Figure 4.8.**

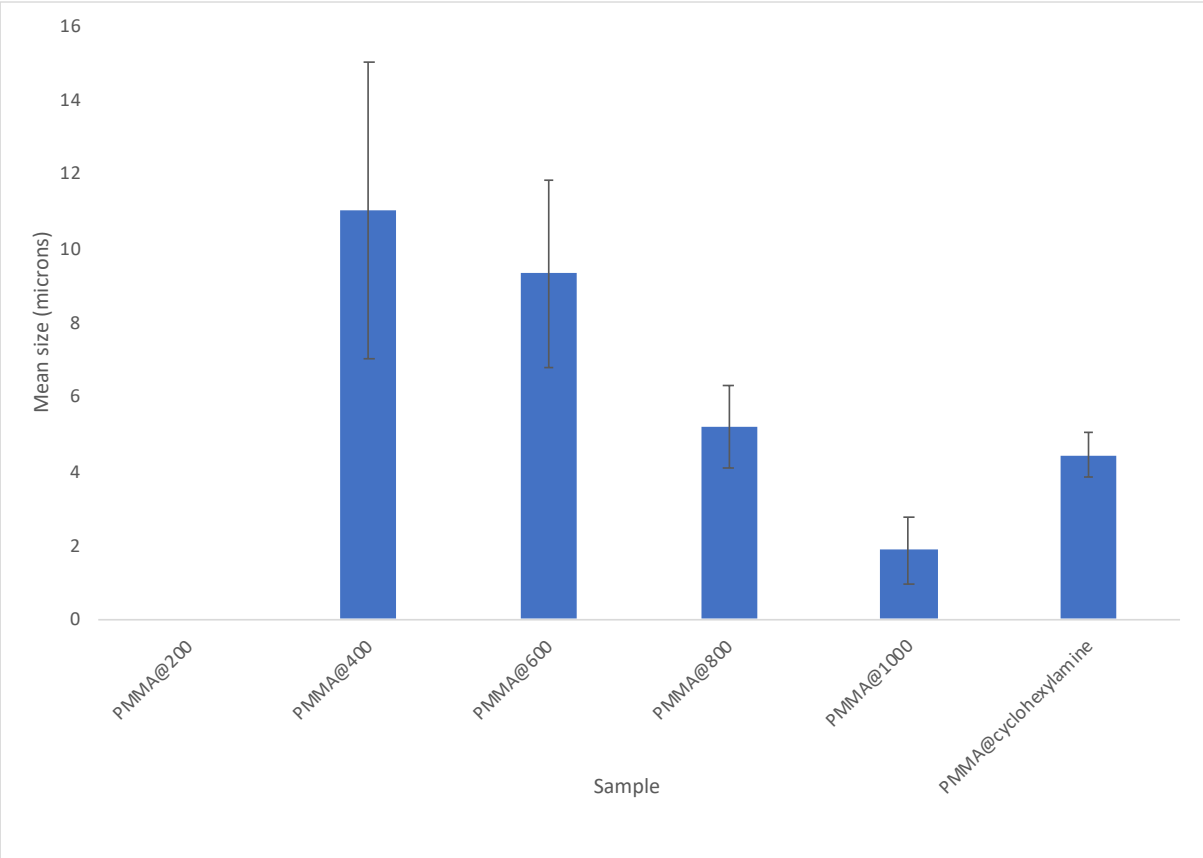

Figure 4.8: Mean microcapsule size obtained for each stirring rate.

4.2.5 Determination of the stirring rate for cyclohexylamine encapsulation.

Synthesis was done at 800 rpms because stirring rates below 200 rpms do not form microcapsules. Lower stirring rates also lead to uneven size distribution of microcapsules, and stirring rates above 1000 rpms will lead to microcapsules forming clusters, which is further summarized in **Figure 4.9.**

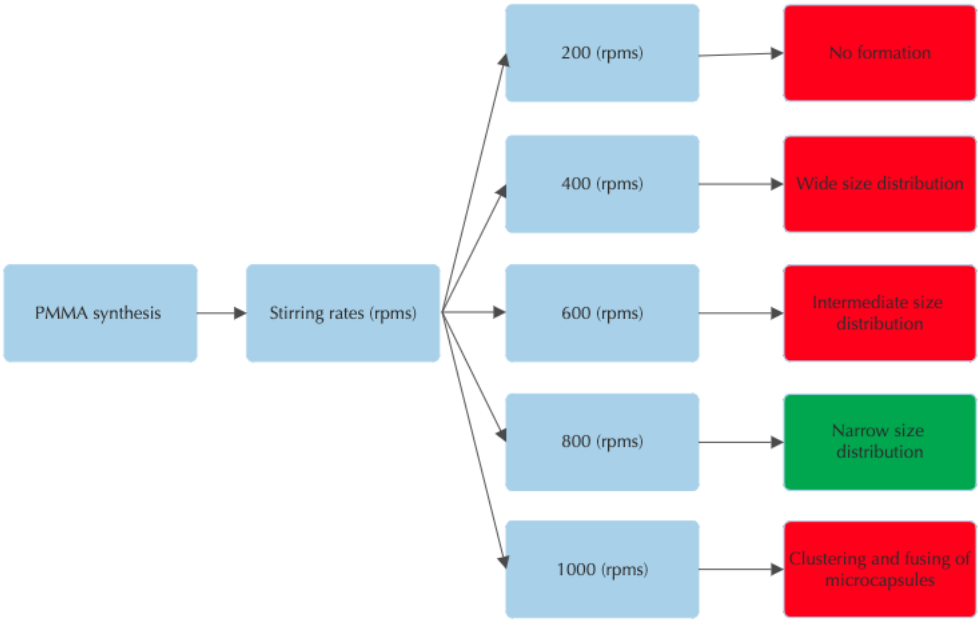

Figure 4.9: Summary of the limitations of each stirring rate compared to all synthesis done at 800 rpms.

4.2.6 SEM analysis of encapsulated cyclohexylamine

Figure 4.10 shows the Cyclohexylamine@PMMA microcapsules within a certain size range. Blank microcapsules Cyclohexylamine@PMMA had a mean size of 4.44 ± 0.59 µm while PMMA@800 microcapsules which were synthesized at the same stirring rate had a comparatively higher mean size of 5.21 ± 1.1 µm. Literature suggests this phenomenon happens because when there is no core material available there the shell expands due to lack or constraint provided by the core material.

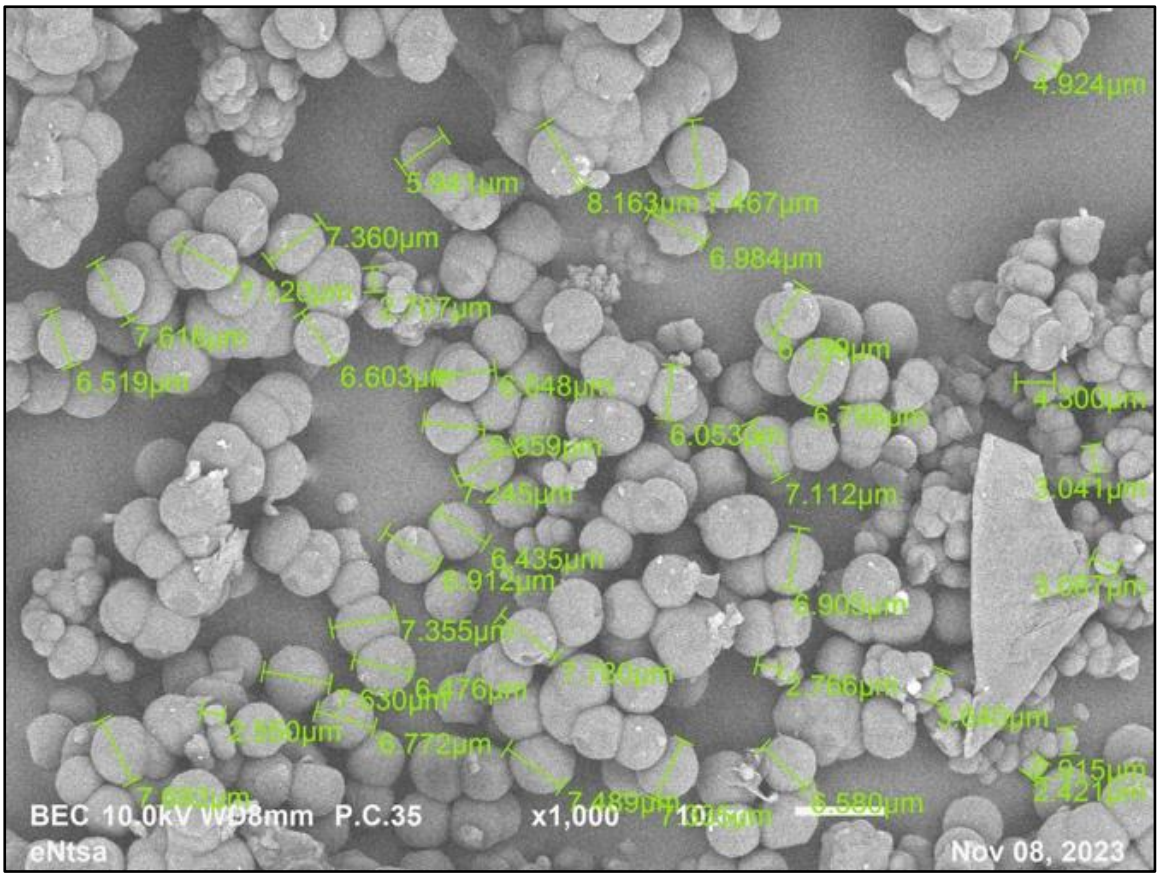

Figure 4.10: SEM images showing morphology of cyclohexylamine microcapsules (Cyclohexylamine@PMMA). A range of capsule sizes are shown.

4.2.7 Volume of cyclohexylamine relative to microcapsule volume

SEM analysis was used to measure the shell diameters and shell thickness in order to determine the capsule volume that would be filled with the active material. The average diameter of the microcapsules obtained was 4.44 ± 0.59 µm and the average wall thickness was 1.22 ± 0.28 µm.

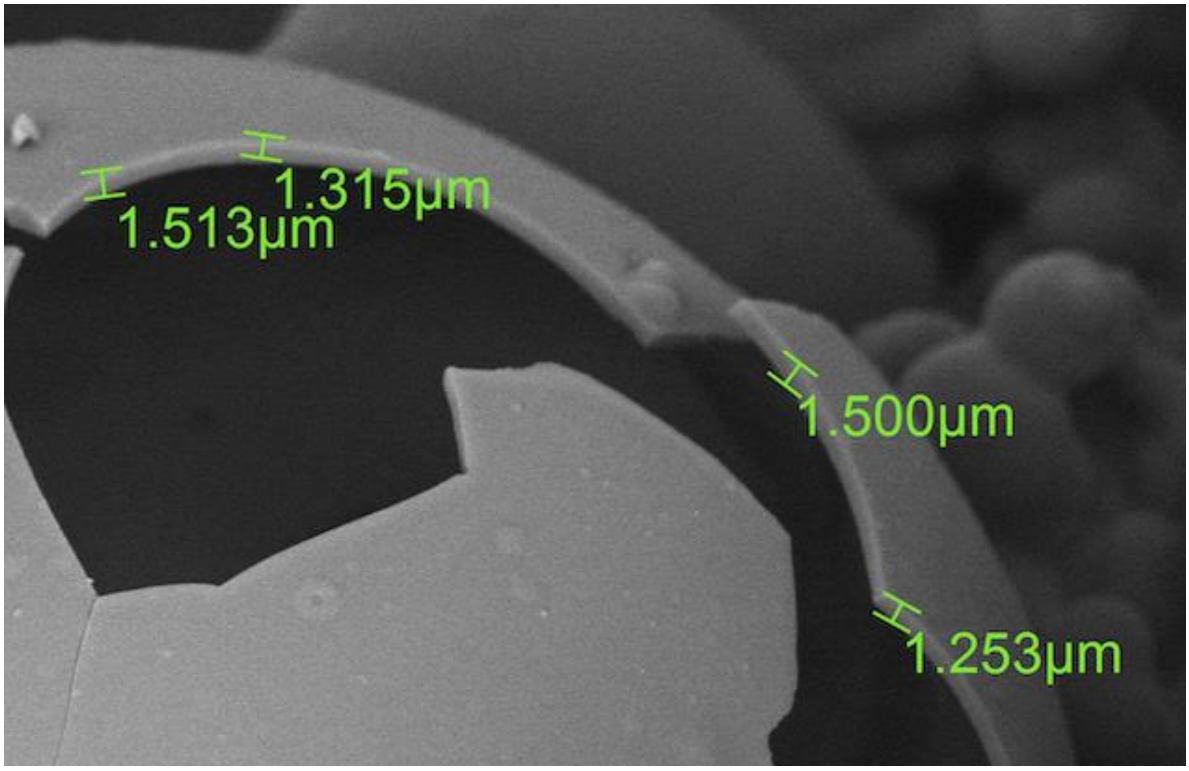

Figure 4.11: SEM images showing the morphology of a broken cyclohexylamine microcapsule. *Other measurements were taken in different areas and statistical calculations were obtained from that data.

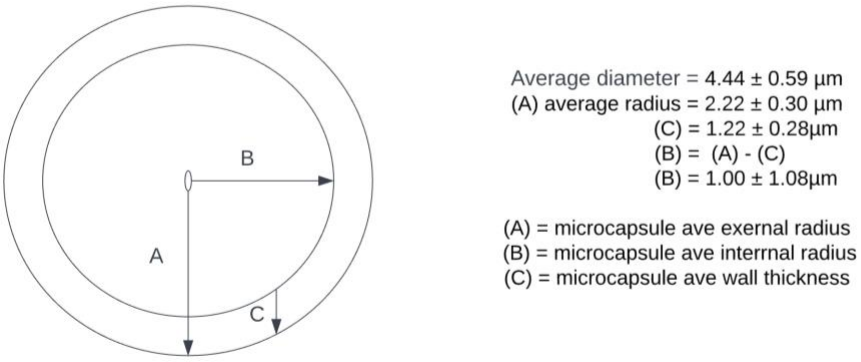

Figure 4.12: Microcapsule volume calculations.

Equations 4.3 was used to calculate the average volume of the whole sphere (single microcapsule) which was 45.82 μm^3.

$$V = \frac{4}{3}\pi r^3 \qquad \text{Eq. 4.3}$$

Where *V*, is the volume of the sphere, and *r* is the radius. The size of the microcapsules are reported in terms of their diameter and hence, the difference between the externally measured diameter of the sphere and the shell thickness would allow one to determine the volume that would be occupied by the additive (internal volume) (Equation 4.4).

$$Ave\ Internal\ radius = \frac{Ave\ exernal\ diameter}{2} - Ave\ shell\ thickness \qquad \text{Eq. 4.4}$$

Considering that the average thickness of the capsules were 1.22 ± 0.28 μm (**Figure 4.11**), the average internal volume was determined to be 4.19 μm^3.

Considering the average internal volume was 4.19 μm^3 and the average external volume was 45.82 μm^3 the amount of cyclohexylamine present in the capsules can be considered to be approximately 9.14% by v/v. based on equation 4.5

$$Percentage\ volume\ of\ cyclohexylamine\ per\ microcapsule = \frac{\text{average internal volume}}{\text{average external volume}} \times 100 \qquad \text{Eq. 4.5}$$

To determine the amount of additive present in microcapsules using other physical methods, Cyclohexylamine@PMMA microcapsules were ground using a pestle and mortar followed by rinsing methanol which effectively dissolved the cyclohexylamine and not the PMMA. The solvent was filtered off and the weight differences were then used to deduce the amount of cyclohexylamine present. Using this method 0.0120 ± 0.0004 g of Cyclohexylamine@PMMA was crushed and drenched in methanol, and after filtering and drying the mass of the residue was found to lie in the range 0.0045 ± 0.0005 g (Equation 4.7).

$$Percentage\ mass\ of\ shell\ per\ microcapsule = \frac{\text{mass after and crushing filtering}}{\text{mass before filtering}} \times 100 \qquad \text{Eq 4.7}$$

The calculations showed that approximately 62.5 ± 4.54% m/m of cyclohexylamine filled the capsules. This value differs from the 9.14 ± 7.90% obtained when using SEM capsule size analysis to determine the volume occupied by the active cyclohexylamine. There could be several factors that would contribute to this that includes the fact that there is a high chance of bubble entrapment during the emulsification process and that during shell formation process not all the PMMA materials is used to form complete shells. This has also been reported in literature where incompletely formed capsules would contribute to the loss of encapsulated material.[102] Hence, when adding the active filled capsules to the electrolyte in the coin cells, a factor of about 27% can be assumed to be inert and not contribute to the activation process during heating.

4.2.8 FTIR analysis of cyclohexylamine and PMMA microcapsules

In order to confirm that the cyclohexylamine was in the entrapped capsules, FTIR was done to notice the differences between blank microcapsules and microcapsules containing cyclohexylamine.

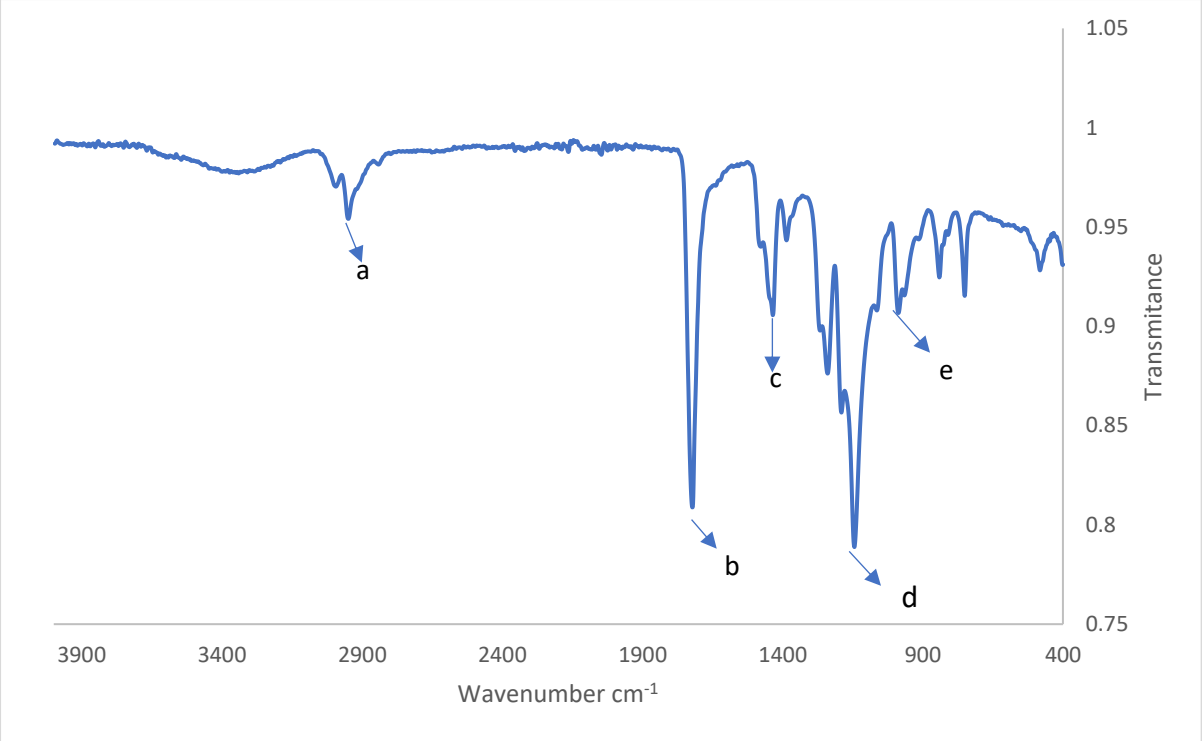

Figure 4.13: FTIR spectroscopy of PMMA capsules only.

The FTIR spectra of the PMMA capsules only indicated the typical functional groups one would expect of the material (**Figure 4.13**). Peak **a** represents the methyl and methylene group, while the sharp intense peak at **b** would relate to the presence of ester carbonyl group stretching vibration. The peak **c** that ranged from 1450-1000 cm^{-1} can be explained by the presence of the C-O (ester bond) stretching vibration. The band **d** and **e** from 1000-850 cm^{-1} would be due to the bending of C-H respectively.

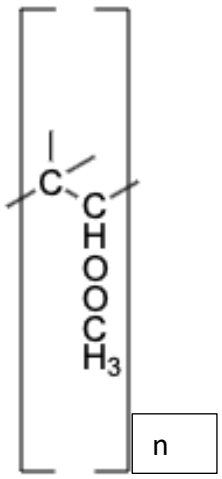

Figure 4.14: Chemical structure of PMMA.

The FTIR spectra of cyclohexylamine only is shown in **Figure 4.15.**

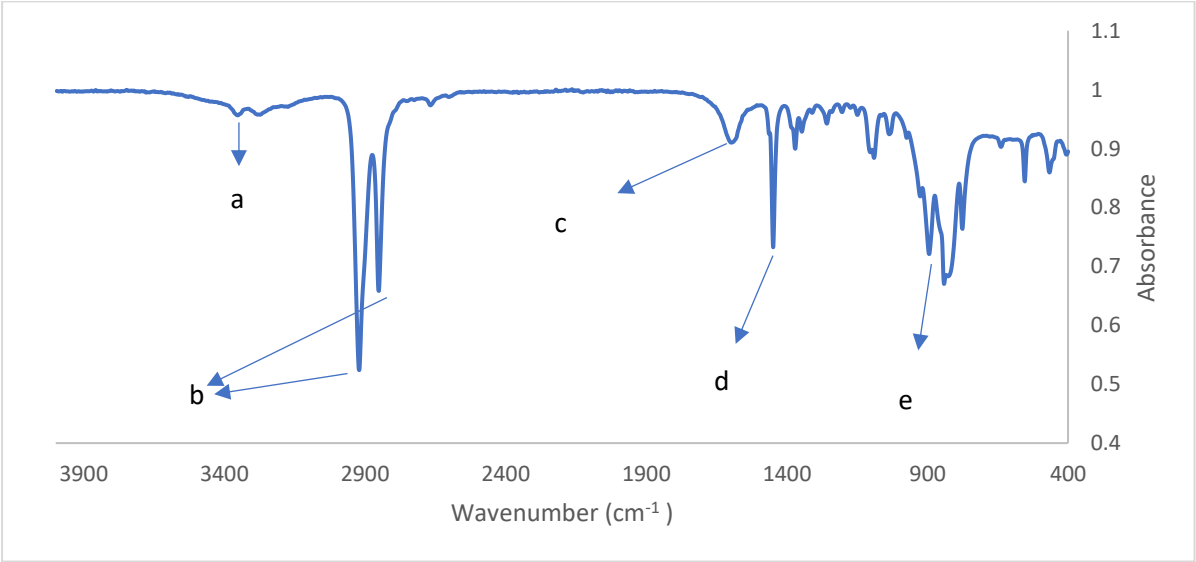

Figure 4.15: FTIR spectroscopy of Cyclohexylamine.

Peak **a** represents the N-H stretching from the primary amines, while peaks labelled **b** are representative of the C-H stretching caused by the aliphatic CH_2 and CH_3 groups. C-C vibrations of the aromatic groups in cyclohexylamine are represented by peak **c**, while peak **d** represents the C-N stretching vibration. Peaks in the area close to **e** are due to out of plane vibrations of C-H groups.

The FTIR spectrum of Cyclohexlamine@PMMA was similar to the spectrum of PMMA only (**Figure 4.16**).

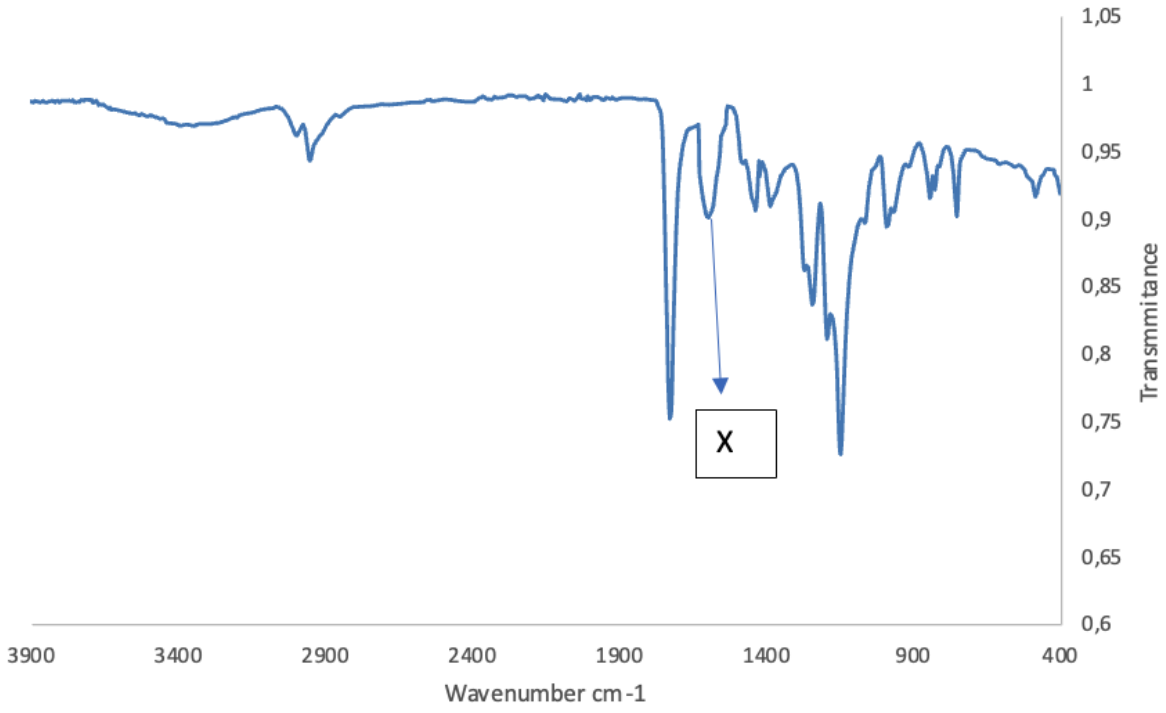

Figure 4.16: FTIR spectroscopy of Cyclohexylamine@PMMA

The peak observed in the 1600 cm^{-1} region labelled **X** in this spectrum would be due to the C-C vibrations found in the aromatic ring of cyclohexylamine.

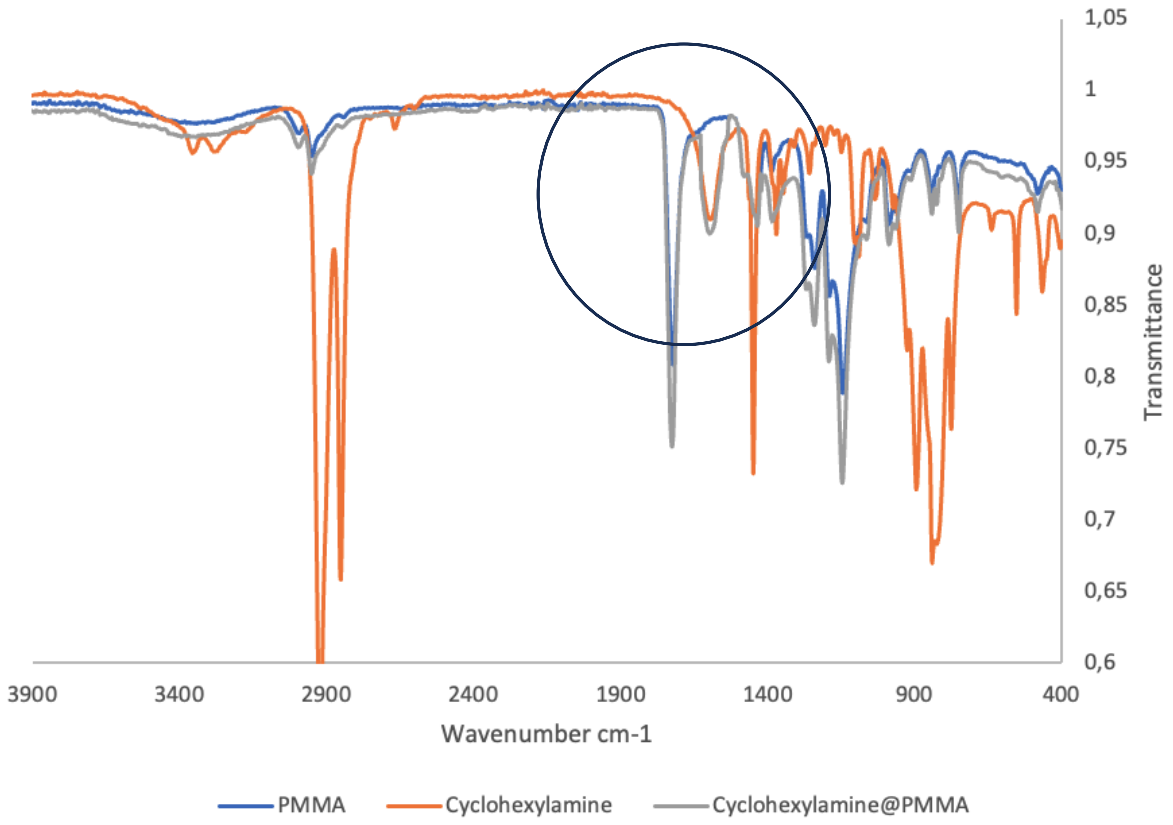

Figure 4.17: FTIR spectroscopy comparing PMMA, Cyclohexylamine and Cyclohexylamine@PMMA

The region marked by a circle in the above figure shows an area where Cyclohexylamine@PMMA and Cyclohexylamine overlap meaning that there is cyclohexylamine present in PMMA shells.

4.2.9 DSC-TGA Cyclohexylamine@PMMA

Wilkie et al [103] report that upon heating PMMA degrades using 2 main mechanisms. These are the cleavage of the main carbon branch and the cleavage of the side branches to produce R-ketones depending on chain length, methane, and methanol. Cyclohexylamine's main degradation product is ammonia which cannot be distinctively marked in **Figure 4.18** because it shows vibrations in the same regions as the methane product. Other decomposition products such as cyclohexane and other R-

ketones cannot be seen as individual peaks in this region because their characteristic peaks are like those found in the degradation products of PMMA. Topological peaks in **Figure 4.18** show that onset begins at 1200 s which corresponds to 198°C meaning there is ongoing decomposition.

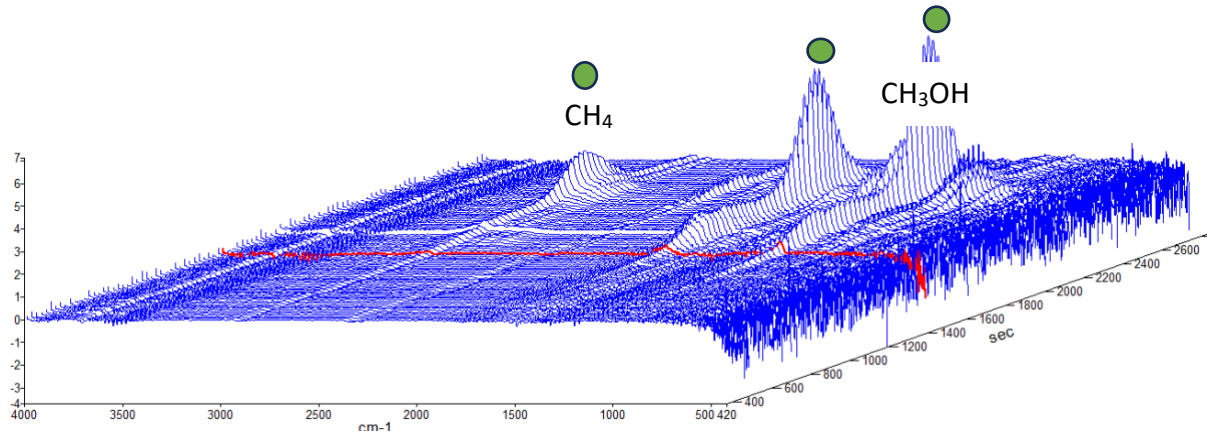

Figure 4.18: TGA-FTIR spectra of PMMA. A time of 2600 seconds corresponds to a temperature of 430 °C, and the ramp rate was 10 °C/min.

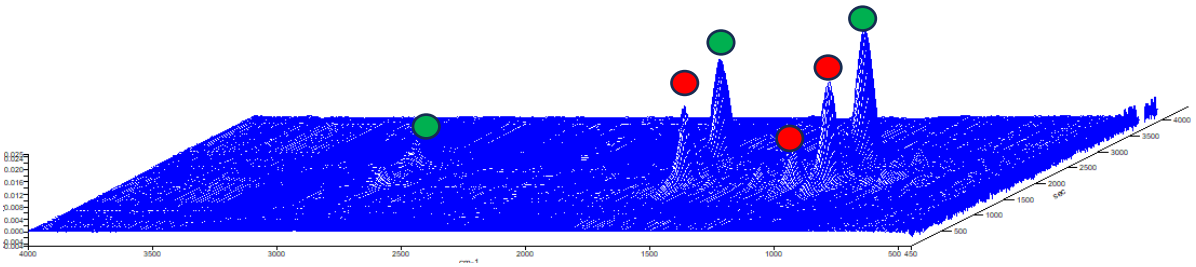

Figure 4.19: TGA-FTIR spectra of Cyclohexylamine@PMMA. A time of 2600 seconds corresponds to a temperature of 430 °C, and the ramp rate was 10 °C/min.

The above figure shows the emergence of PMMA peaks as shown in **Figures 4.18 and 4.19** shown by the green markers. New peaks (red markers) likely represent cyclohexylamine and it decomposes before PMMA due to its lower decomposition

temperature, which means cyclohexylamine is not thermally stable inside the PMMA shells.

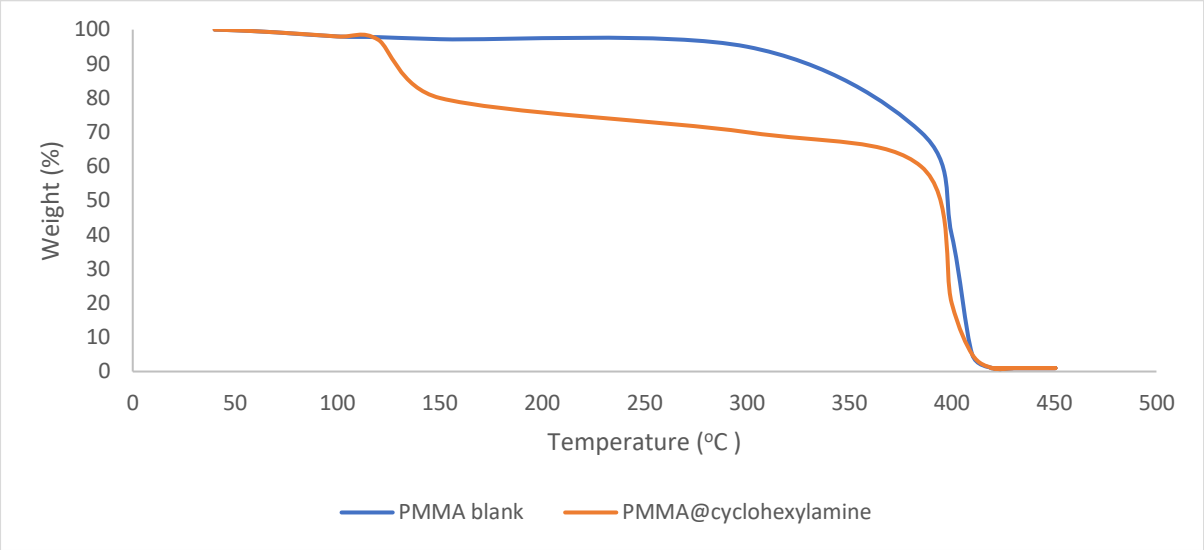

Figure 4.20: TGA thermograms of pure PMMA and Cyclohexylamine@PMMA capsules

The above figure showed that PMMA blank decomposed in 1 stage where >90% of its weight was lost at temperatures above 300 °C, while Cyclohexylamine@PMMA decomposed in 2 stages were the 1st stage started around 126 °C which might be due to cyclohexylamine decomposition. Around <30% of weight was lost, while the 2nd decomposition due to PMMA started at temperature >350 °C and around >65% of weight was lost. This data implies that cyclohexylamine is unstable in the PMMA shells as the TGA thermogram of PMMA only shows a single stage decomposition while Cyclohexylamine@PMMA shows a 2-stage decomposition.

4.3 1,5-Pentadiol encapsulation

Encapsulation of 1,5-pentanediol was done using the PUF shell only, using a o/w emulsion technique. After the synthesis, a fine powder was produced, and the resulting capsules obtained were analyzed by scanning electron microscope (SEM).

4.3.1 Morphology of microcapsules using SEM

The PUF microcapsules were synthesized using the following stirring rates: 200, 400, 600, 800 and 1000 rpms and were named PUF@200, PUF@400, PUF@600, PUF@800 and PUF@1000 respectively. The 1,5-pentanediol microcapsules were synthesized at a stirring rate of 800 and named 1,5-Pentanediol@PUF. The results are summarized in **Table 4.5** and some of the SEM images are shown in **Figure 4.21.**

Table 4.5: Summary of results showing relationship between stirring rates and microcapsules diameter.

PUF Samples	Stirring rate (rpms)	Capsule size range (μm)	Capsules formed
PUF@200	200	20.95 – 2.87	Clustered spheroids
PUF@400	400	17.99 – 2.98	Spherical
PUF@600	600	6.59 – 3.11	Spherical
PUF@800	800	4.34 – 2.74	Spherical
PUF@1000	1000	< 4.20	Spherical
1,5-Pentanediol@PUF	800	5.98 – 2.09	Spherical

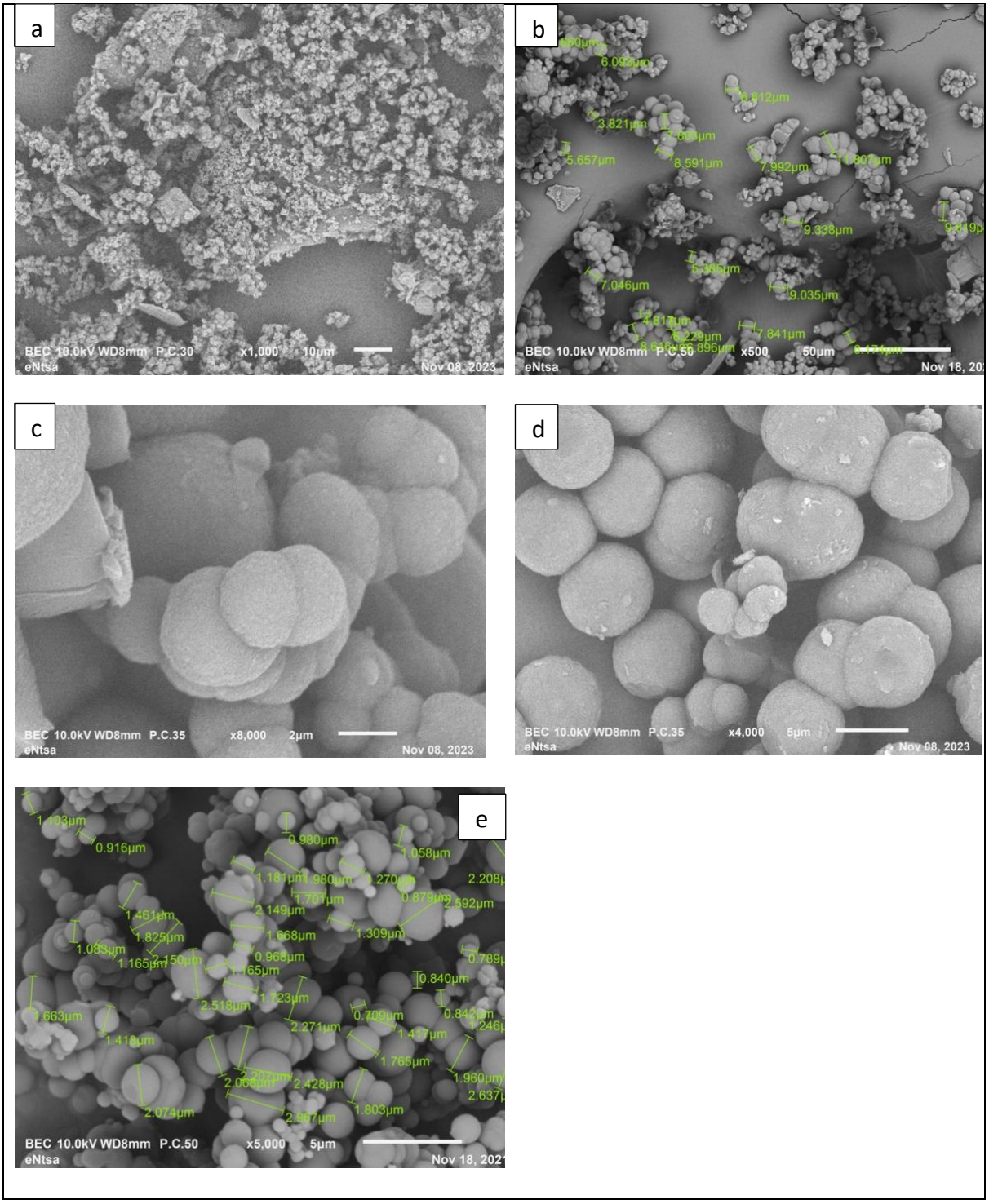

Figure 4.21: Capsules formed at different stirring rates.

* a, b, c, d and e represent PUF@200, PUF@400, PUF@600, PUF@800 and PUF@1000 respectively.

Figure 4.21 a show that at low stirring rates (200 rpms) microcapsules that formed seemed like a cluster but did not look as rigid as the others formed at higher stirring rates.

4.3.2 Size distribution

When making microcapsules, stirring rates are important and directly correlate to the size distribution of the microcapsules formed. Low stirring promotes formation of capsules of different sizes due to the uneven distribution of the shear force while higher stirring rates allow a narrower size distribution due to the even distribution of the shear force required to form droplets. SEM was used to measure the size distribution of the microcapsules. **Figure 4.22** depicts the measurements to determine the microcapsule diameters, and this was done for all samples. Multiple zones were imaged for each sample to get enough data to do statistical analysis as shown in **Table 4.5.**

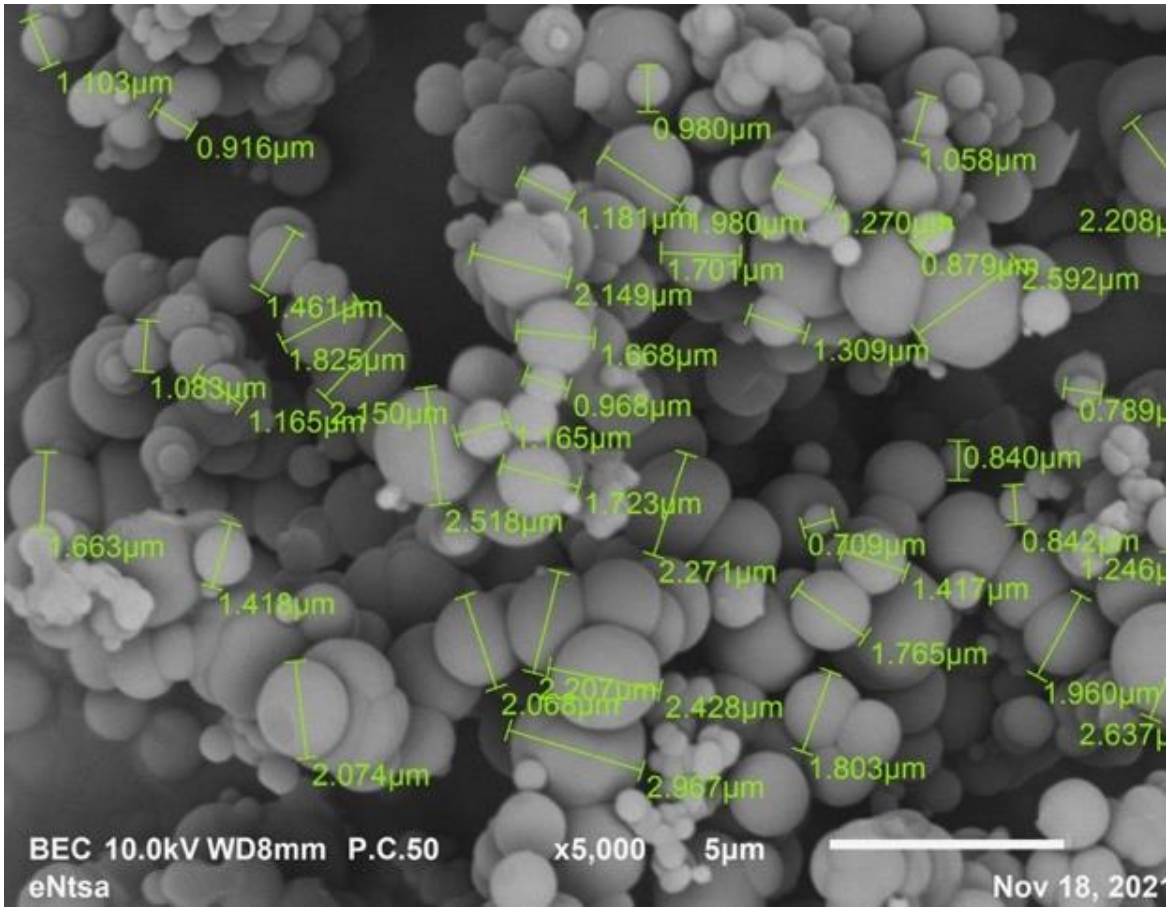

Figure 4.22: SEM image showing how microcapsules diameter size measured (PUF@1000).

Table 4.5 shows that PUF@200 had a size distribution ranging from 20.95 – 2.87 µm. This supports the literature data which points out that low stirring rates forms uneven size distributions, even though the microcapsules had a wide array of sizes, most of the capsules were on average 12.67 ± 4.38 µm.[104] **Figure 4.23** summarizes the results showing the average shell size with their respective standard deviations.

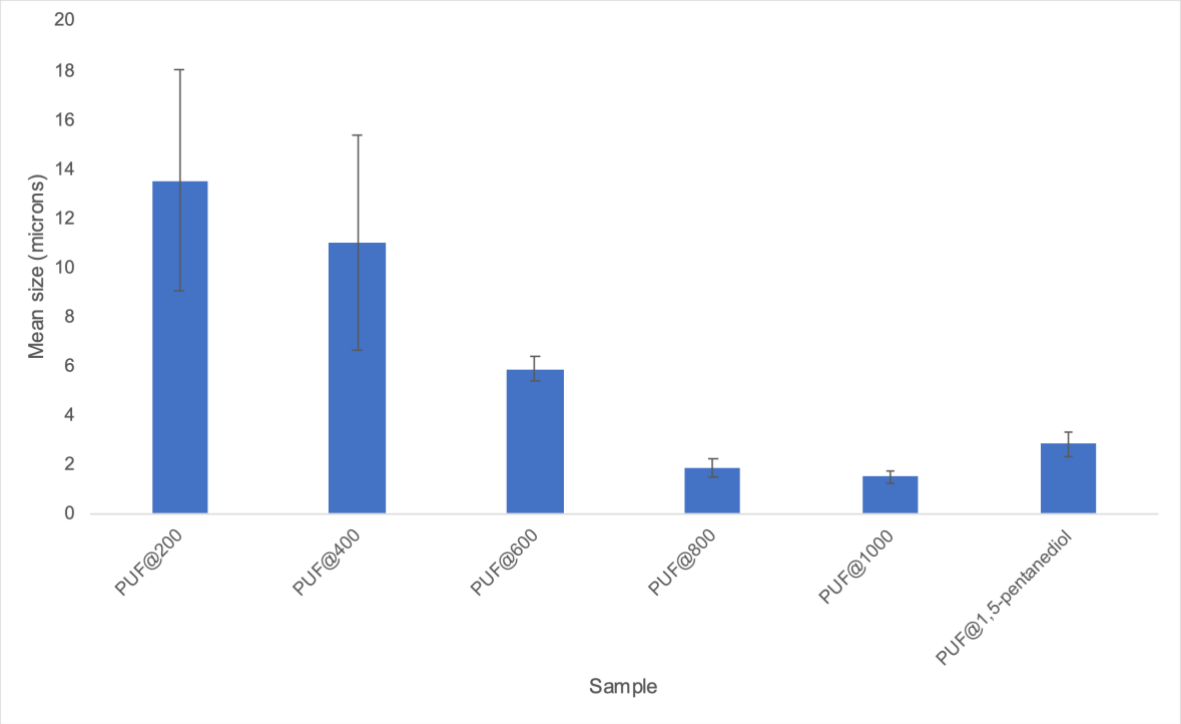

Figure 4.23: Mean microcapsule size obtained for each stirring rate.

4.3.3 SEM analysis of encapsulated 1,5-Pentanediol.

Figure 4.24 shows one of the images used to measure the size distribution of the 1,5-Pentanediol@PUF microcapsules. Blank microcapsules PUF@800 had a mean size of 1.89 ± 0.37 µm while 1,5-Pentanediol@PUF microcapsules which were synthesized

at the same stirring rate had a slightly comparatively higher mean size of 2.56 ± 0.50 µm. All microcapsules were synthesized at 800 rpm because this stirring rate gave a narrower size distribution.

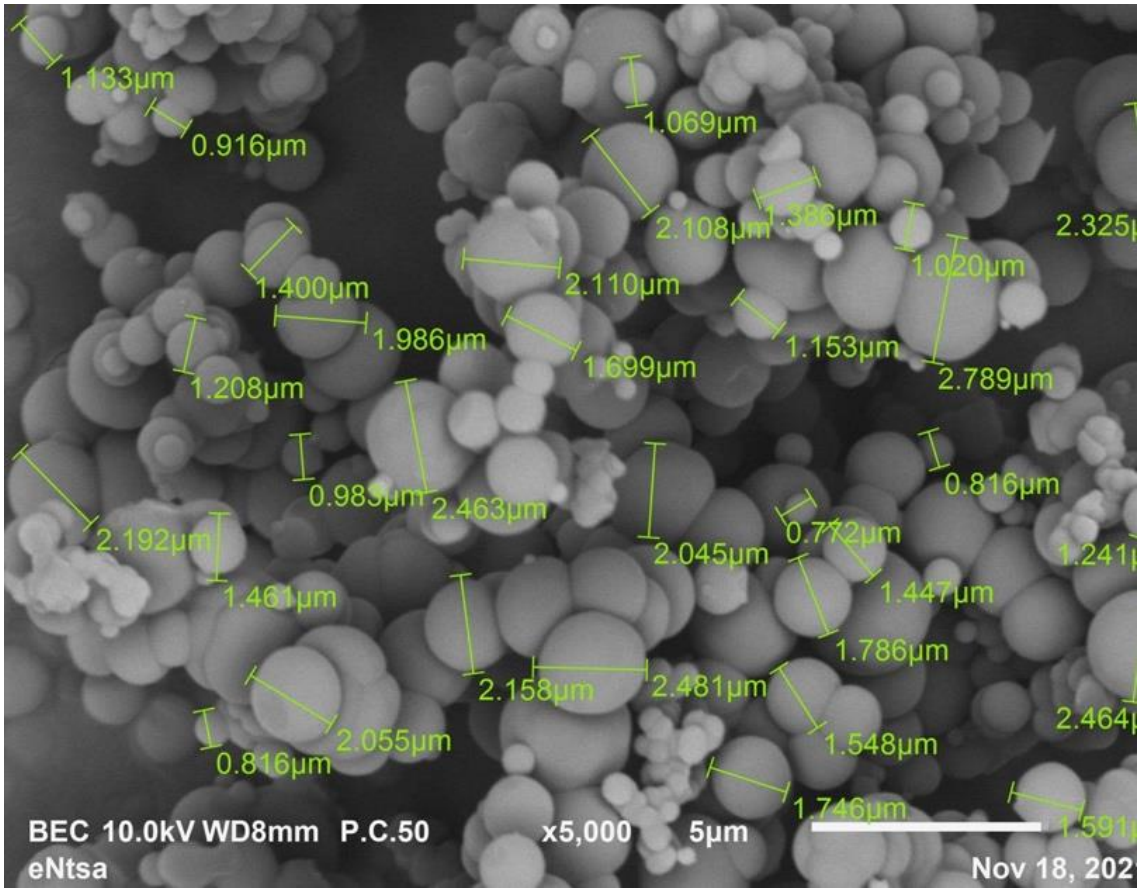

Figure 4.24: SEM images showing morphology of 1,5-Pentanediol microcapsules.

4.3.4 Volume of 1,5-Pentanediol relative to microcapsule volume

SEM was used to measure the shell diameters and shell thickness respectively. The average diameter of the microcapsules obtained was 2.56 ± 0.50 µm and the average wall thickness was 1.01 ± 0.47 µm. This in turn was used to calculate the volume that the capsules can hold. The average diameter (2.56 ± 0.50 µm) for the microcapsules was used to calculate the average volume held by an individual microcapsule.

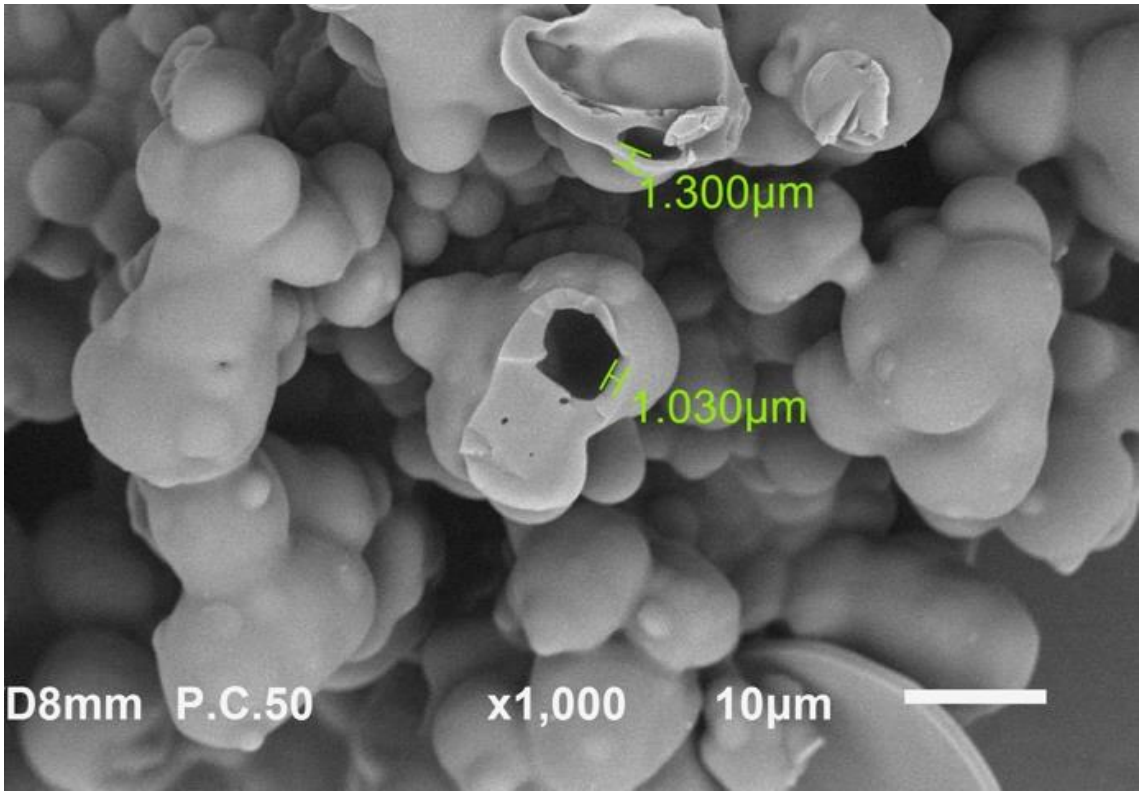

Figure 4.25: SEM images showing morphology of heat treated 1,5-pentanediol microcapsules. *Other measurements were taken in different areas and statistical calculations were obtained.

Equations 4.3 was used to calculate the average volume of the whole sphere (single microcapsule) which was 70.28 μm^3.

$$V = \frac{4}{3}\pi r^3 \qquad \text{Eq. 4.3}$$

Where *V*, is the volume of the sphere, and *r* is the radius. The size of the microcapsules are reported in terms of their diameter and hence, the difference between the externally measured diameter of the sphere and the shell thickness would allow one to determine the volume that would be occupied by the additive (internal volume) (Equation 4.4).

$$Ave\ Internal\ radius = \frac{Ave\ exernal\ diameter}{2} - Ave\ shell\ thickness \qquad \text{Eq. 4.4}$$

Considering that the average thickness of the capsules was 2.56 ± 0.50 µm µm (**Figure 4.24**), the average internal volume was determined to be 15.61 μm^3.

Considering the average internal volume was 15.61 μm^3 and the average external volume was 70.28 μm^3 the amount of cyclohexylamine present in the capsules can be considered to be approximately 22.21% by v/v. based on equation 4.5

$$Percentage\ volume\ of\ cyclohexylamine\ per\ microcapsule = \frac{\text{average internal volume}}{\text{average external volume}} \times 100 \qquad \text{Eq. 4.5}$$

To determine mass of 1,5-Pentanediol in microcapsules using physical methods, 1,5-Pentanediol@PUF microcapsules were ground using a pestle and mortar and the ground material was drenched in acetone which effectively dissolve 1,5-Pentanediol and not PUF. The solvent was filtered off, the weight differences were then used to deduce the amount of cyclohexylamine present. Using this method 0.0416 ± 0.0032 g of 1,5-Pentanediol@PUF was crushed and drenched in acetone, after filtering and drying the mass of the residue was 0.0231 ± 0.0022 g.

This method showed that the amount of 1,5-pentanediol present in the shell was 59.01 ± 3.40%. This value was different but close to the 22.21 ± 9.02% obtained when using SEM data, showing us that there was less bubble entrapment during emulsification.

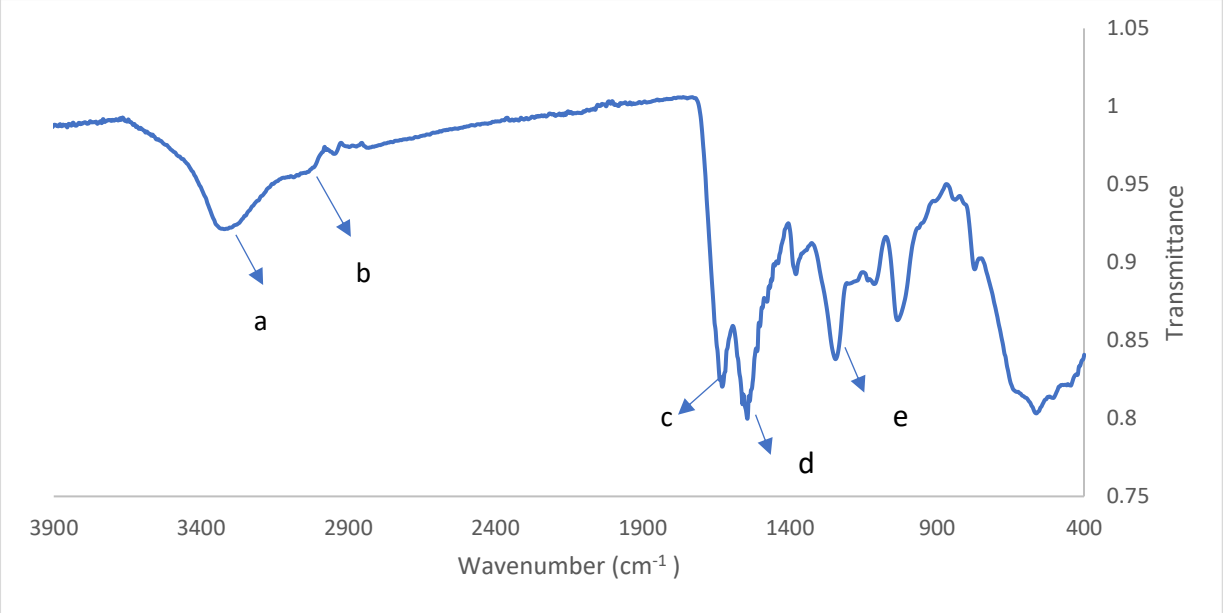

Figure 4.26: FTIR spectroscopy of PUF

The FTIR spectrum of PUF indicates the details of functional groups present in the synthesized PUF (**Figure 4.26**). The peak **a** ranging from 3400 cm^{-1} was due to the presence of NH and OH groups. A dull broad peak at point **b** appeared due to the presence of the ester C-O stretching vibration. The peak **c** at 1650 cm^{-1} can be explained as the C=O (ester bond) stretching vibration while peak **d** at 1550 cm^{-1} was due to an N-H stretch. The band **e** from 1420 cm^{-1} was due to the bending of C-H.

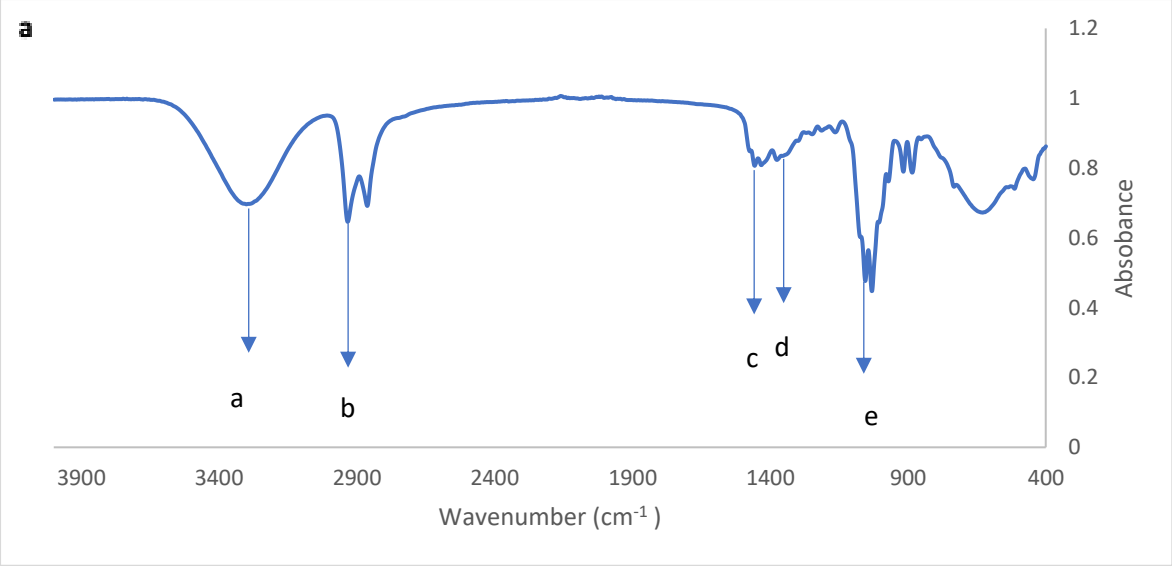

Figure 4.27: FTIR spectroscopy of 1,5-pentanediol

Figure 4.27 shows 1,5-pentanediol FTIR were **a** is a broad peak which represents the OH vibrations, while **b** was due to aliphatic C-H stretching. Peak **c** represents C=C stretching vibration, while peak **d** was due to C-H bending. C-O stretching is denoted by peak **e**.

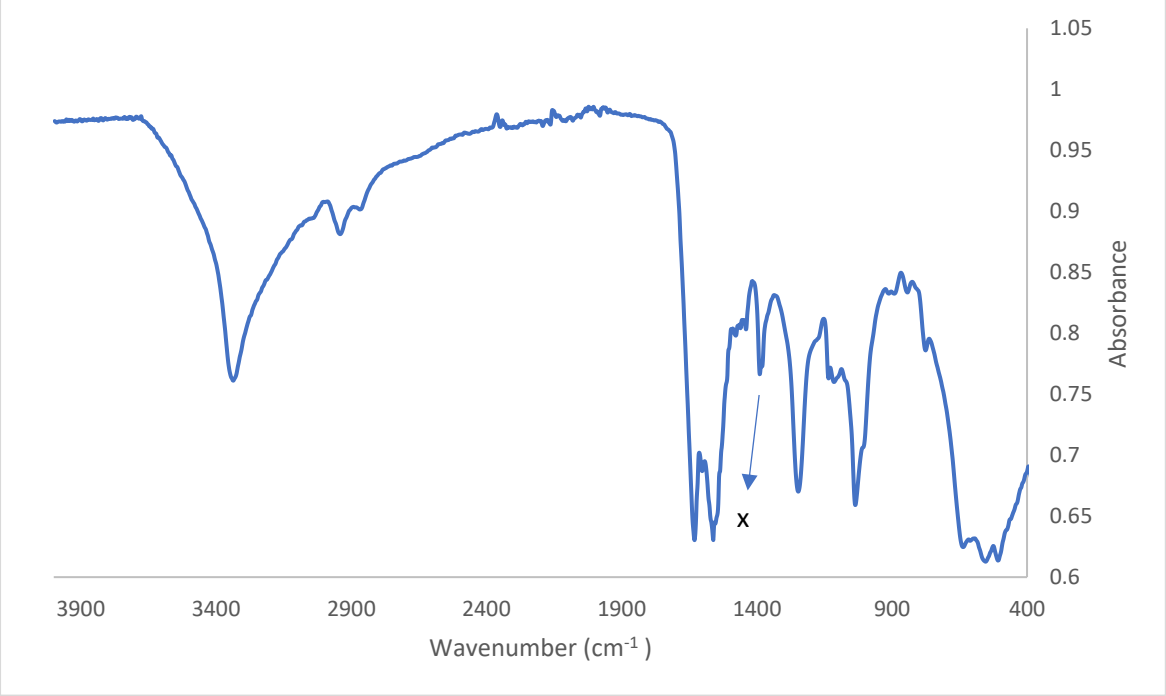

Figure 4.28: FTIR spectroscopy of 1,5-Pentanediol@PUF.

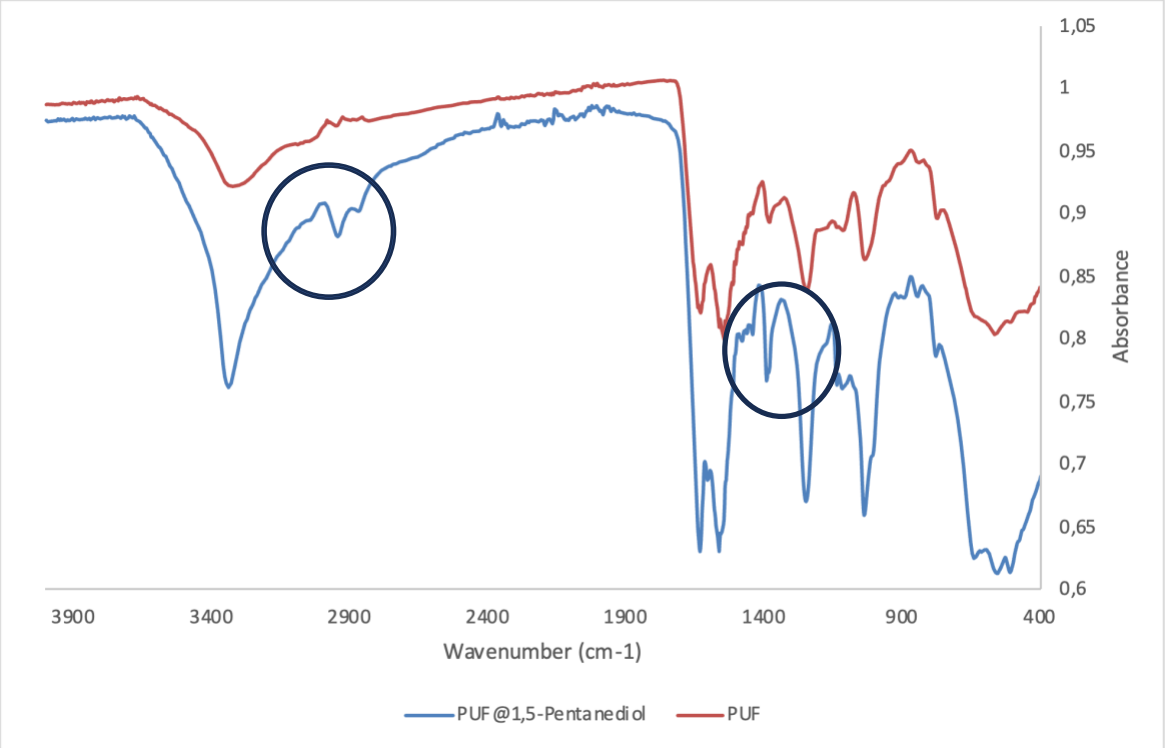

Figure 4.29: Comparison between PUF and 1,5-Pentanediol@PUF

The peaks circled in **Figure 4.29** shows the unique ones that would correspond to 1,5-Pentanediol which confirms the presence of 1,5-Pentanediol in 1,5-Pentanediol@PUF.

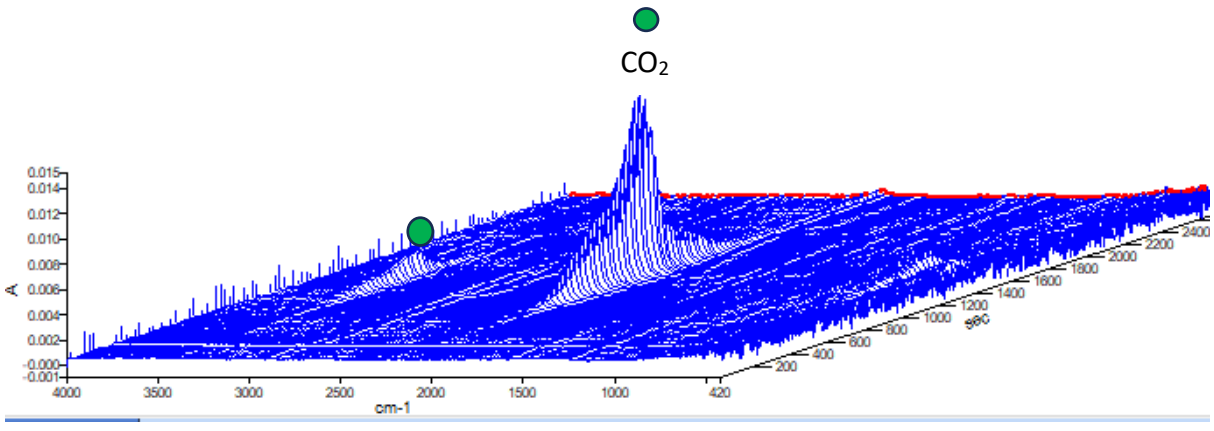

Figure 4.30: TGA-FTIR spectra of PUF. A time of 2600 seconds corresponds to a temperature of 430 ºC, at the heating ramp rate of 10 ºC/min.

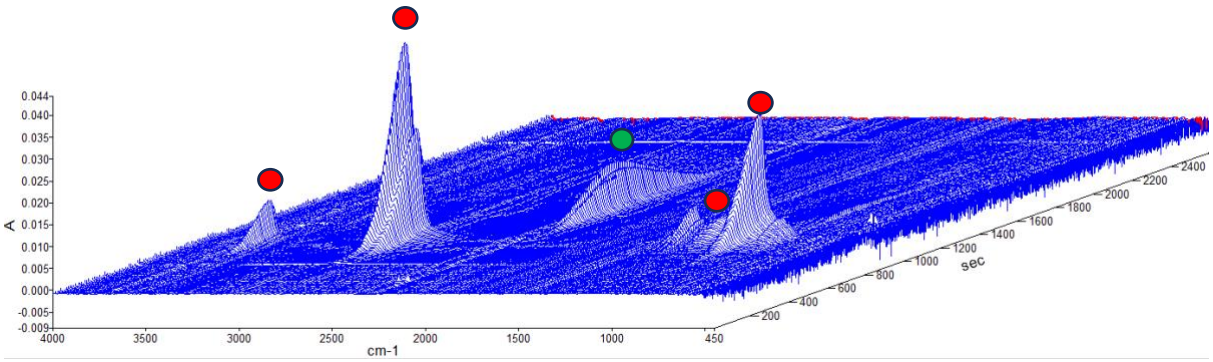

Figure 4.31: TGA-FTIR spectra of 1,5-Pentanediol@PUF. A time of 2600 seconds corresponds to a temperature of 430 °C, at the heating ramp rate of 10 °C/min.

The graphs data shown in **Figures 4.30 and 4.31** suggest that in 1,5-Pentanediol@PUF sample, there is a second decomposition other than PUF shown by the red markers. The emergence of FTIR peaks linked to 1,5-Pentanediol first before PUF peaks (green markers) suggest that 1,5-Pentanediol is not stable inside the PUF shells and 1,5-Pentanediol decomposition ends before PUF starts to decompose.

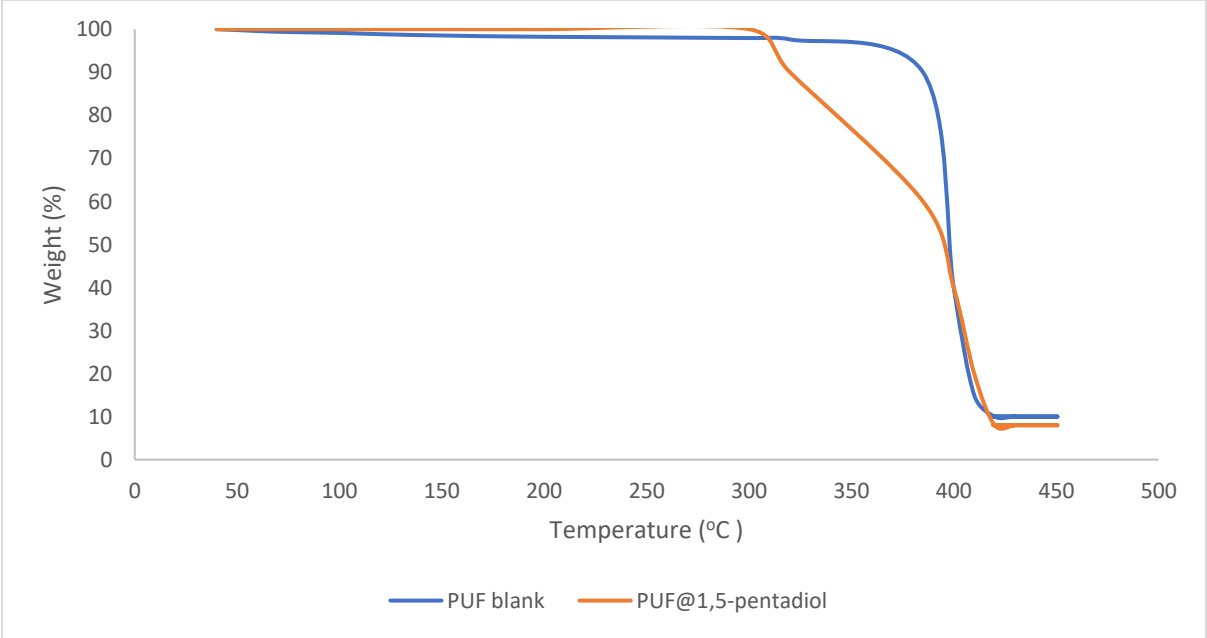

Figure 4.32:TGA thermograms of pure PUF and 1,5-Pentanediol@PUF capsules.

The two-stage decomposition observed in 1,5-Pentanediol@PUF indicates that the thermal stability of the PUF matrix is affected by the presence of 1,5-pentanediol. The decomposition graph in **Figure 4.32** shows that PUF blank decomposed in one step where >90% of its weight was lost at temperatures above 350 ^{o}C, while 1,5-Pentanediol@PUF sample showed a two-step decomposition were the 1st step started around 280 ^{o}C which might be due to the 1,5-pentanediol decomposition occurring with about 30% of its mass loss. The 2nd decomposition would be due to the decomposition of the PUF at temperature >350 ^{o}C where around 40% of the sample mass was lost. The TGA data in **Figure 4.32** suggests that 1,5-Pentanediol is unstable inside PUF microcapsules. Hence, its loss and decomposition occurred before PUF decomposition commenced.

4.4 Cell capacities

Lithium-ion Coin Cell capacity studies were done in order to determine the effect of adding either 1,5-Pentanediol@PUF or Cyclohexylamine@PMMA microcapsules on the electrochemical performance.

Since the LFP cells are in a discharged state, after assembly, the first step was to charge them to a voltage limit of 4.2 V. The cells were subsequently capacity cycled by discharging and charging them at voltages limits of 2.5 V to 4.2 V, respectively, and all units of capacity were demonstrated in mAh/g of the active material (cathode). The average amount of additive within the capsules that were added was determined based on the study done in **section 4.2 and 4.3**. The amount of LFP-en-ad added to the stock electrolyte solution for the cells was 10 wt% of the encapsulated active resulting in an amount of about 6.5 wt% of cyclohexylamine and 7 wt% of 1,5-

Pentanediol in the electrolyte if released upon a heating event respectively. For all the comparative studies done, all cells were charged and discharged at 0.1 C.

Figure 4.33 shows the capacities obtained for 3 different 2032 LFP coin cells. The initial discharge capacities of the 3 tested blank coin cells was 139.5 mAh/g, 137.3 mAh/g and 137.7 mAh/g respectively and were within the range most literature would report on.[105,106] Based on the theoretical capacity of 170 mAh/g, the average of the three coin cells built was 81.2% of the suggested theoretical value.

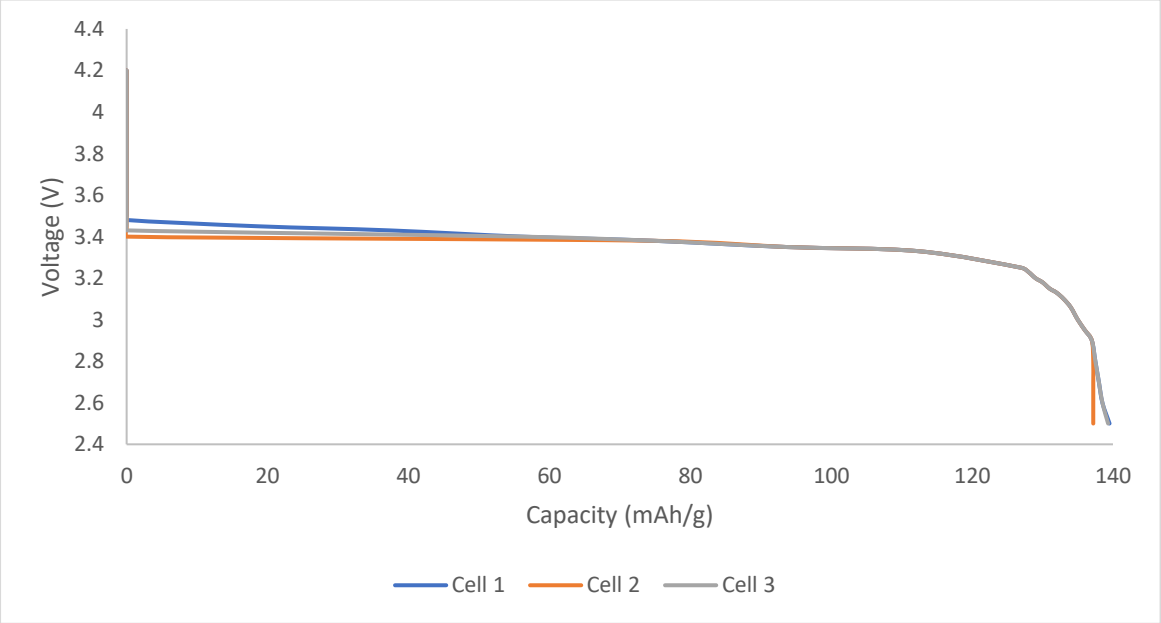

Figure 4.33: Discharge curves for LFP cells without any additives or capsules.

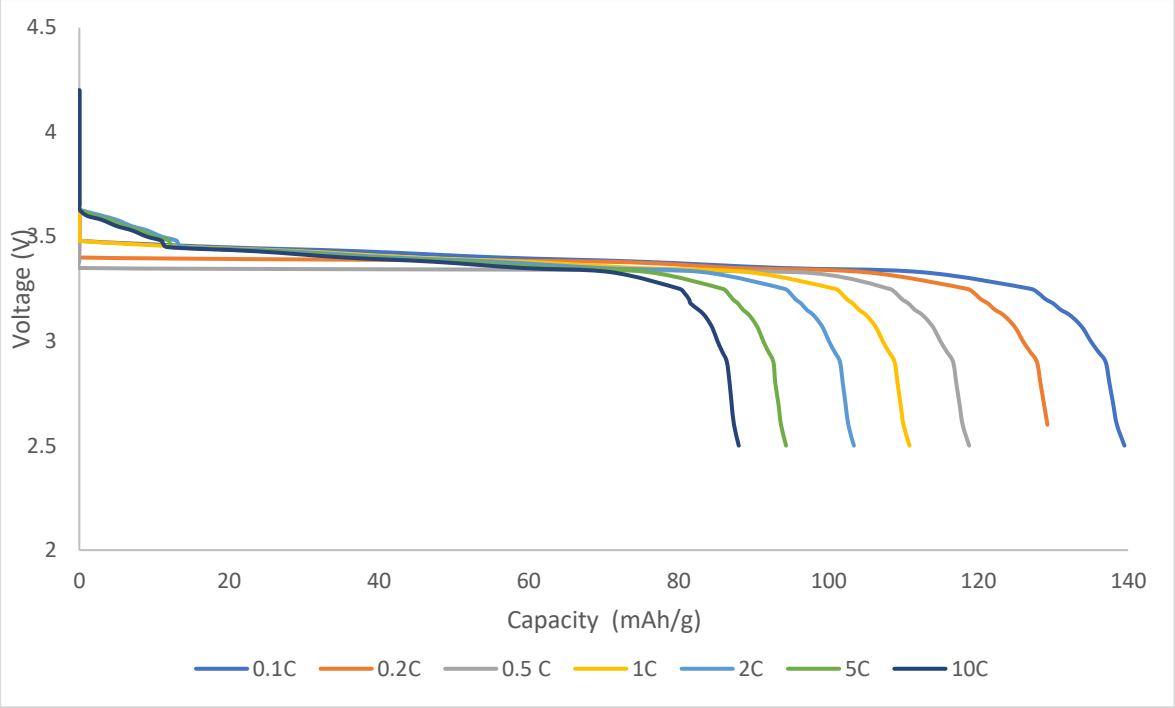

Figure 4.34: Discharge capacity results of LFP cells at different C-rates

The results in **Figure 4.34** show that as the discharge C-rate increases the effective capacity within the coin cell decreases, which follows literature suggestions because at higher C-rates there is higher internal resistance within the battery, polarization effects within the battery increase due to sped up electrochemical reactions and lithium diffusion rate becomes a limiting factor as electrolyte may not deliver ions quickly to meet the high demand hence the reduced capacity.[107–109]

Figure 4.35 shows the discharge capacity curves for a commercial LFP cell over 10 cycles capacity cycles.

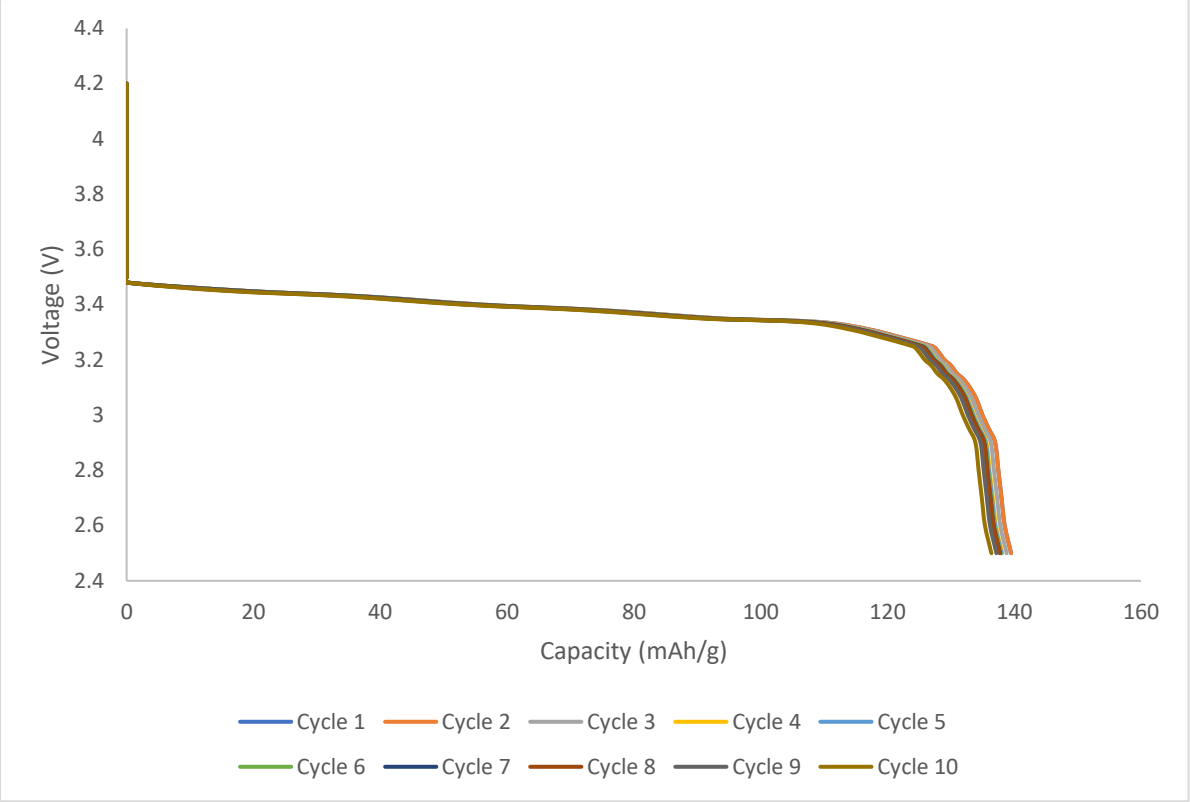

Figure 4.35: Capacity cycling on the LFP coins cells over 10 cycles.

The above figure shows that as the number of cycles increase the effective capacity decreases slightly and can be due to several factors:

i. As capacity cycling takes place the active material on the electrodes experiences some expansion and contraction that damages the electrode / electrolyte interface.[110]

ii. Lithium plating and stripping will allow formation of dendrites on the negative electrodes which affects the number of lithium-ions available for charge transfer hence the capacity fade.[107]

In this study, capacity cycling over 10 cycles showed a specific capacity drop of 2% (**Table 4.6).**

The effect of PMMA microcapsules with and without the active ingredient cyclohexylamine on coin cell capacity is shown in **Figure 4.36**

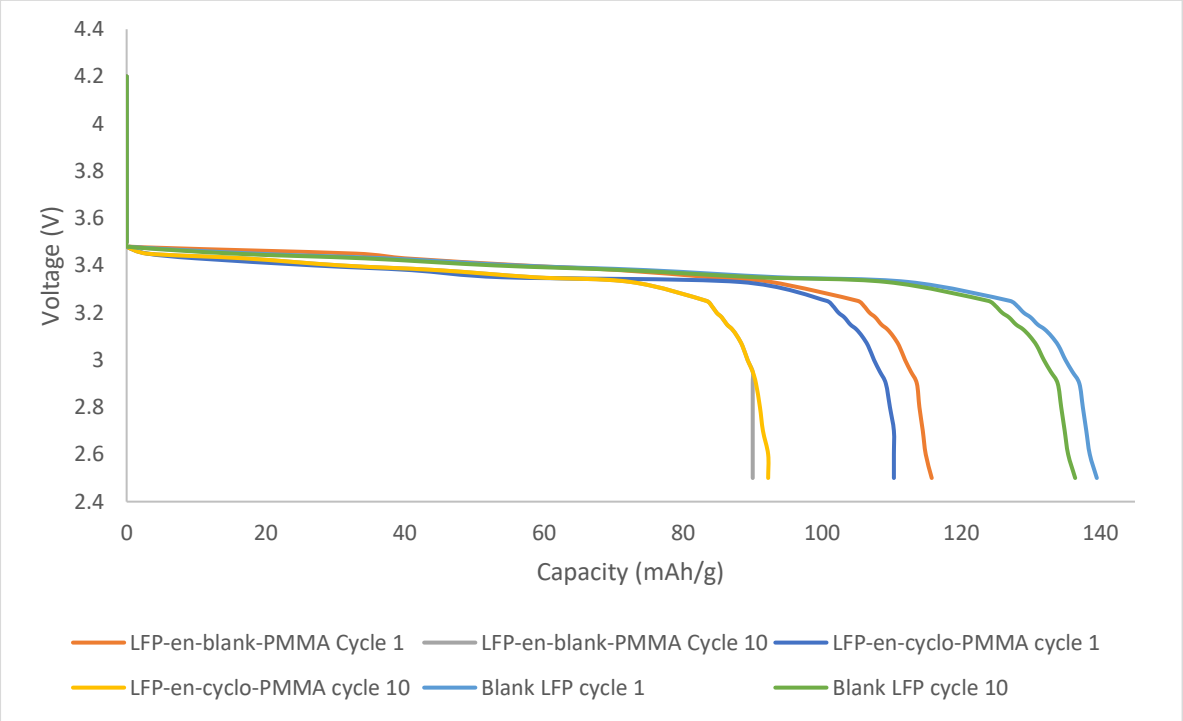

Figure 4.36: Effect of PMMA microcapsules and microencapsulated cyclohexylamine on battery capacity

The results showed that the addition of microcapsules to the coin cell system significantly affects the capacity and capacity retention. This is summarized in **Table 4.6** and could be due to the increase of the internal resistance of the capsules hindering the mobility of lithium ions. However, the addition of the microcapsules did not seem to influence the capacity cycle ability significantly, cells still showed relatively good capacity after 10 successive cycles. Similarly, the effect of the PUF microcapsules with and without the active ingredient pentanediol on battery capacity is shown in **Figure 4.38**

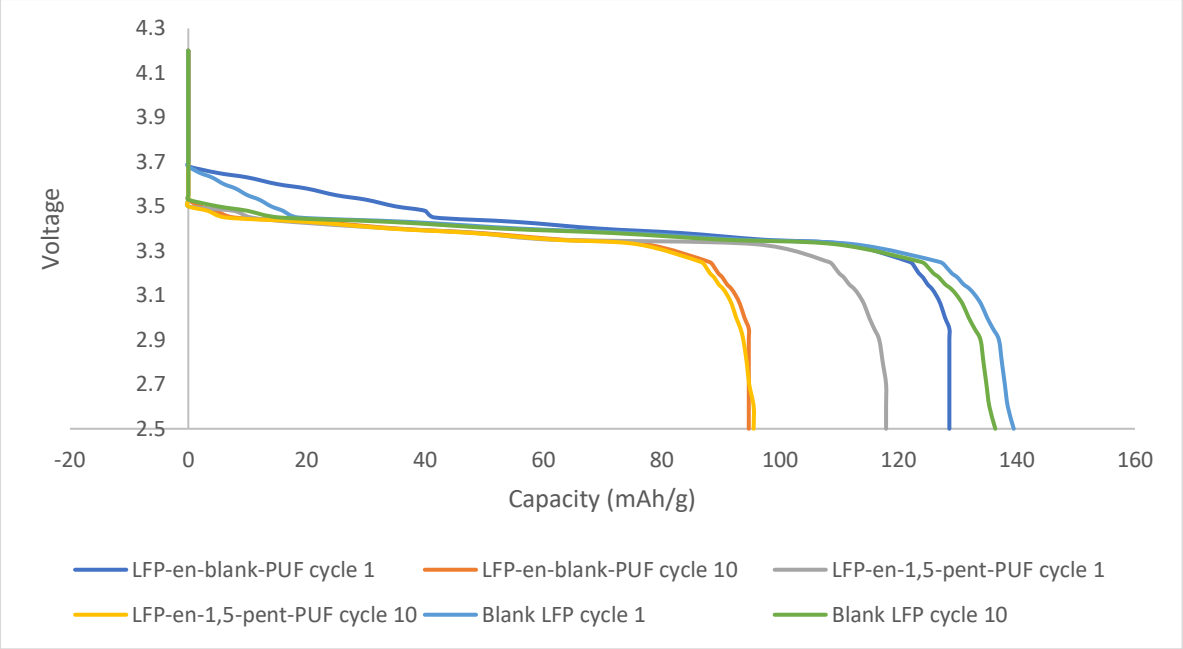

Figure 4.38: Effect of PUF microcapsules and microencapsulated 1,5-pentanediol on the LFP coin cell capacity.

The results are summarized in **Table 4.6** showing the respective loss in capacity for each of the respective LFP cells studied with and without the addition of the PMMA and PUF microcapsules.

Table 4.6: Summary of discharge capacities of initial and final cycle

Sample	Initial capacity (mAh/g)	10^{th} cycle capacity (mAh/g)	Capacity retention (%)
LFP blank 1	139.51	136.11	97.6
LFP blank 2	137.20	132.51	96.6
LFP blank 3	139.31	135.08	96.9
LFP-en-blank-PMMA	115.77	90.02	77.8
LFP-en-cyclo-PMMA	110.33	92.25	83.2
LFP-en-blank-PUF	121.37	94.72	78.7
LFP-en-1,5-pent-PUF	117.93	95.55	81.0

The results showed that there was reasonable capacity repeatability for LFP blank coin cells that were fabricated with about 82% of the expected theoretical capacity. By the addition of the empty (blank) capsules of PMMA and PUF respectively, the capacity

the first cycle dropped to 68% and 71% of the theoretical capacity. This shows that even the empty capsules by themselves would negatively influence the capacity performance of the cells capacity, which in part could be ascribed to an increase in the internal resistance and a decrease in the lithium ion mobility. Similar to the addition of the blank or empty capsules of PMMA and PUF, the addition of the filled capsules showed a decrease in the initial capacity when compared to the theoretical capacity. For the “LFP-en-cyclo-PMMA" and "LFP-en-1,5-pent-PUF" the cells showed only 65% and 69% of the theoretical capacity respectively. Notably, the LFP cells with the additives all showed a relatively higher capacity loss over the 10 cycle test when compared to the cells without any additives. The exact reasons for this phenomena would be difficult to determine where further studies would be required to look at the in-situ effect of the capsules on the active material during capacity cycling.

4.5 Effectiveness of additives

To test the effectiveness of the additives to the 2032 coin cells that contained the encapsulated additives, the cells were submerged in mineral oil and heated to 300^{o}C for 10 minutes. Their respective cell voltages were recorded before and after heating and the results are summarized in **Table 4.7**.

Table 4.7: Summary of cell voltages before and after heating in mineral oil at 300 °C respectively.

Sample	Initial voltage (V)	Voltage after heating (V)
LFP blank 1	3.23	2.11
LFP blank 2	3.33	2.00
LFP blank 3	3.19	1.75
LFP-en-blank-PMMA	3.0	1.0
LFP-en-cyclo-PMMA	3.14	0.32
LFP-en-blank-PUF	2.99	1.52
LFP-en-1,5-pent-PUF	3.13	0.66

The results showed that when blank LFP cells are subjected to heat, there is only a small drop in the voltage that could be ascribed to the partial decomposition of some cell components such as the loss in electrolyte and membrane shrinkage. These cells would remain partially functional but not subjected to any charge or discharge tests due to the high possibility that a thermal event could occur due to an internal short and the decomposition of the electrolyte would spark a fire. Cells made with either PMMA and PUF microcapsules only showed a significant decrease in the coin cell voltage. Notably, the coin cells that contained the encapsulated additives showed the largest decrease in the cell voltage, implying that the capsules in the cell would have released the additives that interacted with the electrolyte to suppress any significant ion mobility. None of these cells were subjected to any further capacity charge or discharge tests due to the safety concerns of the experimental conditions. Such cells would have to be tested in dedicated flame and explosion proof chambers. However, the large decrease in observed cell voltage does imply that both the cyclohexylamine and 1,5-pentanediol that were encapsulated showed to have its intended effect after heating, thereby reducing the ionic movement and rendering the cell chemistry safe from possible thermal runaway events.

4.6 EIS studies before and after capacity cycling

AC-impedance involves application of a known AC signal with a known amplitude, which spans over a wide frequency range and has an effect on the 2032-coin cell electrochemical system. The resistance values recorded are a response to the amplitude and phase change of the current relative to the voltage. Resistance (R) is a function of voltage/current hence R_{int} refers to the internal resistance posed by inner components of the coin cells which include the separator, electrolyte and additives. Additives such as microcapsules and blank liquids affect this type of resistance. R_{cath} refers to the resistance caused by charge transfer on the cathode specifically due to the cathode-electrolyte interface, since the 2032-coin cells that were built contained lithium metal as anode. Only one semi-circle was observed because lithium metal has a negligible resistance effect on the EIS plot. The results are typical Nyquist plots that showed semi-circle at high frequencies. For illustration purposes, an example of fitting the equivalent circuit model (ECM) to two scans are shown in **Figure 4.39.** After fitting a suitable ECM to the data, the results are summarized in **Table 4.8** and the graphs are shown in **Figure 4.40 and 4.41** respectively**.**

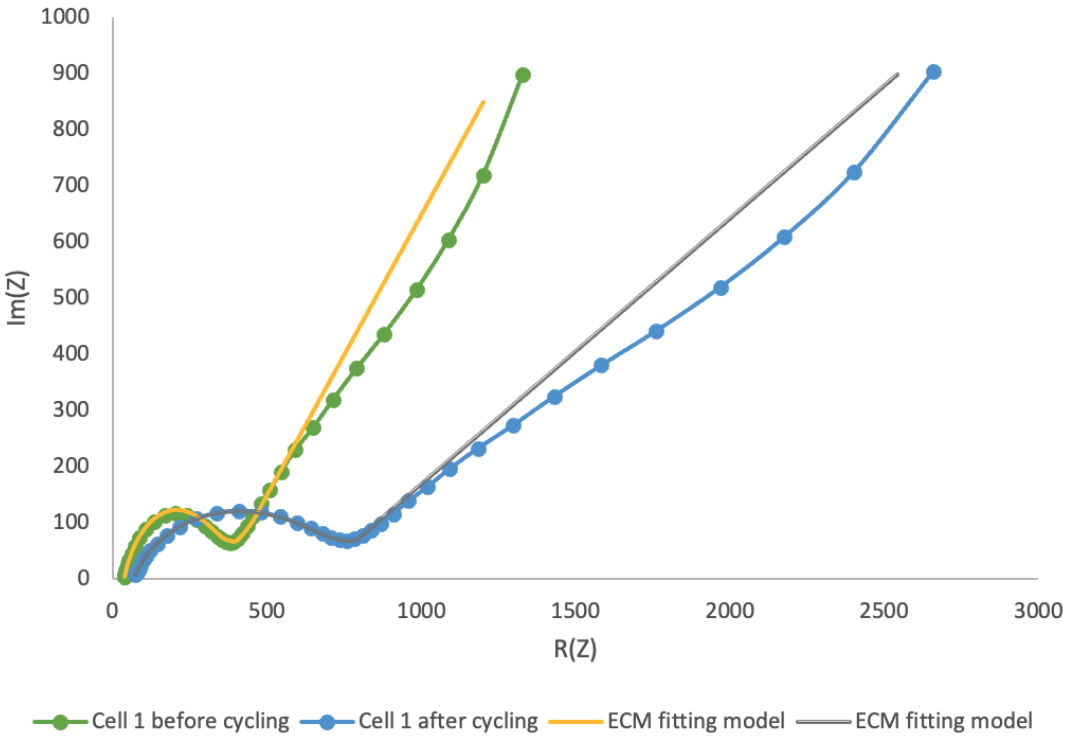

Figure 4.39: EIS results obtained for Blank LFP coin cells before and after capacity cycling with the ECM fitting model

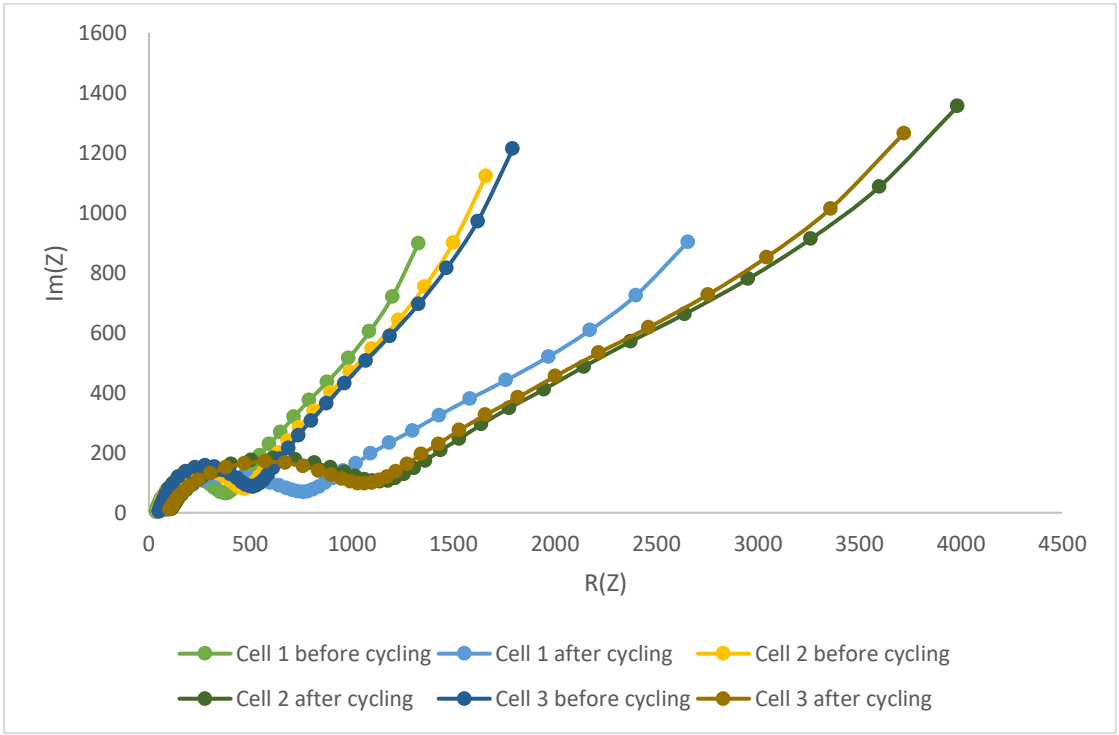

Figure 4.40: EIS results obtained for Blank LFP coin cells before and after capacity cycling

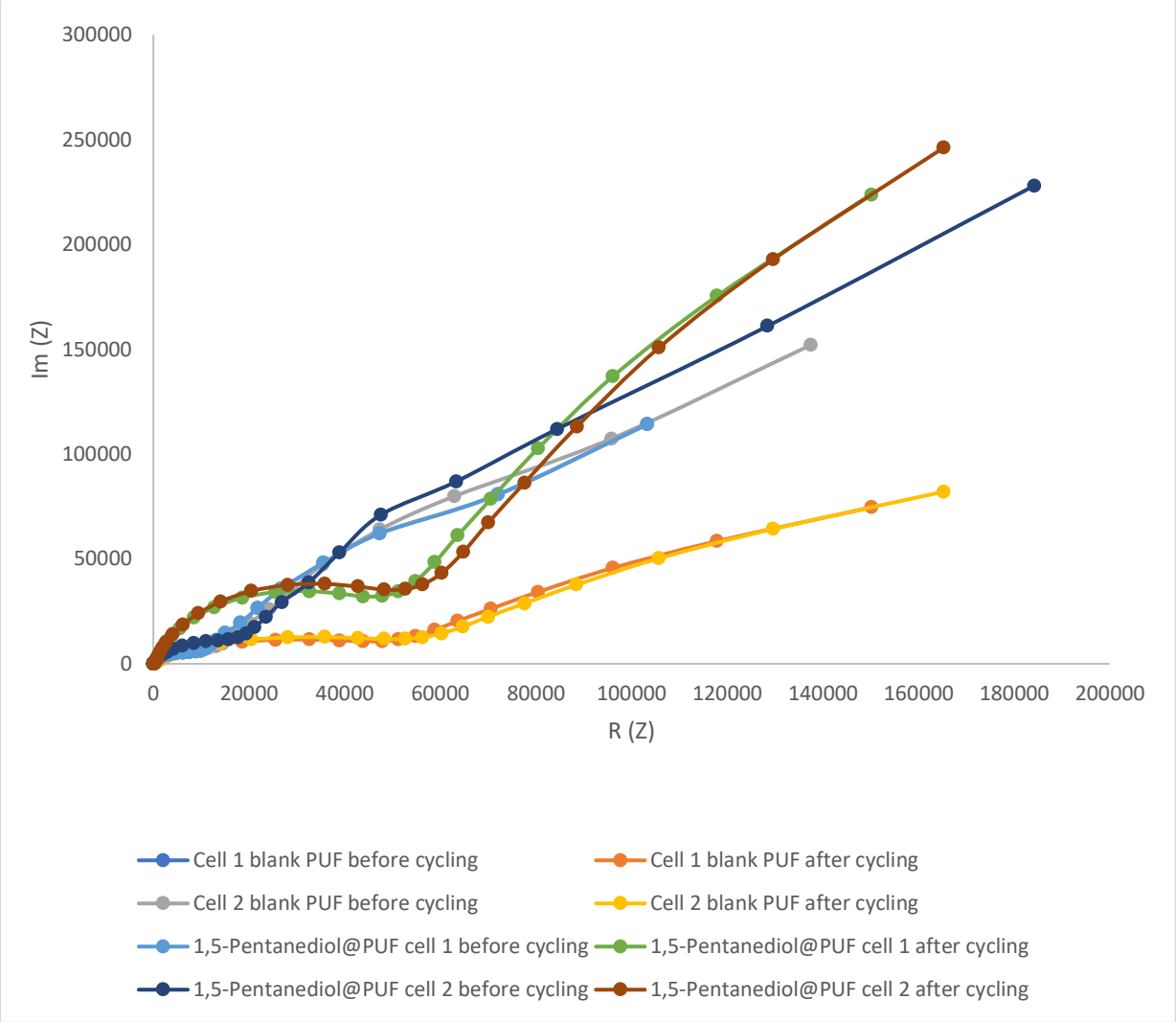

Figure 4.41: EIS results obtained for LFP coin cells containing PUF blank and filled with 1,5 Pentanediol before and after capacity cycling

Table 4.8: Summary of EIS data obtained for all coin cells that contained PMMA/PUF microcapsules and their derivatives before and after capacity cycling. The respective R and Zw values were obtained from the fitting of the Equivalent Circuit Model described in **Figure 3.10**

Sample name		$R_{internal}$ (Ω)	$R_{cathode}$ (Ω)	Z_w (Ohm/$s^{-1/2}$)
Blank LFP 2032-coin cell (before cycling)	Cell 1	13.44	375.23	234
	Cell 2	15.45	435.56	129
	Cell 3	13.99	390.44	334
Blank 2032-coin cell (after cycling)	Cell 1	19.87	654.33	173
	Cell 2	22.34	527.98	180
	Cell 3	29.45	657.55	181
PMMA blank 2032-coin cell (before cycling)	Cell 1	23.43	11065	5400
	Cell 2	25.67	12098	3400
PMMA blank 2032-coin cell (after cycling)	Cell 1	60.97	34080	6000
	Cell 2	57.54	35670	3200
Cyclohexylamine@PMMA 2032-coin cell (before cycling)	Cell 1	26.77	21090	9978
	Cell 2	29.56	10080	9870
Cyclohexylamine@PMMA 2032-coin cell (after cycling)	Cell 1	69.78	26090	2300
	Cell 2	66.77	32000	3400
PUF blank 2032-coin cell (before cycling)	Cell 1	30.33	13001	5000
	Cell 2	21.34	10111	4218
PUF blank 2032-coin cell (after cycling)	Cell 1	74.21	39000	6320
	Cell 2	69.33	34567	4443
1,5-Pentanediol@PUF 2032-coin cell (before cycling)	Cell 1	36.77	24500	9978
	Cell 2	29.56	23456	9345
1,5-Pentanediol@PUF 2032-coin cell (after cycling)	Cell 1	69.78	29090	3200
	Cell 2	66.77	31900	4300

The results summarized in **Table 4.8** indicated that shows both the $R_{internal}$ and $R_{cathode}$ resistances for Blank LFP coin cells increased after capacity cycling implying that some ageing effect had occurred at the electrode interfaces with the electrolyte. In part, this could be due to the formation and growth of the SEI layer that is formed on the electrode surfaces due to the reactions between the electrolyte and the electrodes. While this layer is critical for battery operation, with time and capacity cycling it can increase the internal resistance by impeding ion transport between electrodes.

The results also showed that by the addition of microcapsules, the $R_{cathode}$ value increased significantly with only a slight increase or change in $R_{internal.}$ Hence, the added microcapsules seem to alter the functionality of the cathode active materials surface reducing the free lithium-ion movement within the cell and electrolyte. Hence, further studies will be required to reduce this effect of the microcapsules on the cathode's active material.

5: Conclusion and further work

5.1 Conclusion

The research aimed at investigating a wide array of R-diols and R-amines as potential additives to reduce the negative effects of a thermal runaway in LIB. These additives would react with the LIB electrolyte component (EMC) to form a gel like product. This would form a physical barrier between anode and cathode to prevent short circuiting and reduce ion mobility. Six chemicals were investigated namely cyclohexylamine, dicyclohexylamine, benzylamine, ethanediol, 1,2-propanediol and 1,5-pentanediol respectively. The two best performing additives were cyclohexylamine and 1,5-pentanediol that were observed to reduce the conductivity of the electrolyte significantly by using EIS measurements. Cyclohexylamine and 1,5-pentanediol showed significant increases in resistance after heating that also suggests that cyclohexylamine and 1,5-pentanediol might undergo chemical changes or decomposition when exposed to excessive heat. Both Cyclohexylamine and 1,5-pentanediol were then encapsulated in PMMA and PUF microcapsules respectively which were then incorporated into LIB. These capsules seem to influence the capacity performance of the cells and the respective EIS measurements suggest that they

increase the surface resistance of the cathode active material. However, the microcapsules seem to retain the active ingredients over at least 10 capacity cycles showing only a slight decrease in respective capacity performances. Upon heating these coin cells in an oil bath to 300 ^{o}C, a large decrease in the cell voltage was observed implying that the heat had triggered the release of the aforementioned additives thereby gelling with the electrolyte and potentially hindering further internal cell thermal events.

Cyclohexylamine was successfully encapsulated with PMMA to form Cyclohexylamine@PMMA microcapsules that appeared as spherical shape microcapsules with a smooth surface. Other techniques such as TGA-FTIR was used to deduce successful encapsulation. The TGA results showed the degradation patterns of PMMA which had a 1 stage decomposition showing presence of only 1 substance while Cyclohexylamine@PMMA decomposed in 2 stages and the first decomposition is due to cyclohexylamine.

1,5-Pentanediol was encapsulated with PUF to form 1,5-Pentanediol@PUF microcapsules that showed to have spherical shape capsules with a smooth surface finish. TGA-FTIR again showed the successful encapsulation of the additive where the TGA results showed the degradation of the PUF and 1,5-Pentanediol@PUF to be different.

Coin cell, voltage and EIS studies show that addition of microcapsules to LFP 2032-coin cells decreases the cell capacity due to them increasing the internal resistance within the LFP 2032-coin cells. Both cyclohexylamine and 1,5-pentadiol showed their ability to hinder ionic transfer within LFP 2032-coin cells in scenarios where normal

LFP 2032-coin cells operational temperatures are exceeded thereby limiting the chance of thermal runaway occurring.

5.2 Further Work

In order to expand on the current research work, the following studies would contribute to the scaling and possible application of the technology to commercial LIB cells.

- A more detailed reaction study of the proposed additives and the final products for both the cyclohexylamine and 1,5-pentanediol would elucidate the mechanisms.
- Study the effects of varying the concentrations of cyclohexylamine on the LIB electrolyte at room temperature and pressure.
- Investigate other R-diols and R-amines and their effect on LIB electrolyte and to elucidate possible reaction kinetic mechanism of the R-diols or R-amines with the LIB electrolyte.
- Study the mechanism for the increase in the cathode resistance upon adding microcapsules to the electrolyte. To study possible ways of limiting the movement of the microcapsules with the electrolyte to the regions of the separator only.
- Scale the additive of the microencapsulated material to significant amounts that can be incorporated into larger 18650 commercial LIB. These cells can then be subjected to safety and destructive testing according to the UN38.3 specification for the transportation of dangerous goods.

References

1. Jiang W, Zhang G, Deng J. Comparable Investigation of Phosphorus-Based Flame Retardant Electrolytes on LiFePO 4 Cathodes . *J Electrochem Soc*. 2022;169(5):050532. doi:10.1149/1945-7111/ac707e

2. Ye Y, Chou LY, Liu Y, et al. Ultralight and fire-extinguishing current collectors for high-energy and high-safety lithium-ion batteries. *Nat Energy*. 2020;5(10):786-793. doi:10.1038/s41560-020-00702-8

3. Wu B, Pei F, Wu Y, et al. An electrochemically compatible and flame-retardant electrolyte additive for safe lithium ion batteries. *J Power Sources*. 2013;227:106-110. doi:10.1016/j.jpowsour.2012.11.018

4. Garg MA, Garg A, Chhipa K, Kumar L. *M*icroencapsulation techniques in pharmaceutical formulation. Vol 199. https://www.researchgate.net/publication/359391954

5. Singh MN, Hemant KSY, Ram M, Shivakumar HG. *Microencapsulation: A Promising Technique for Controlled Drug Delivery*. Vol 5.; 2010.

6. Yang S, Gu Y, Qu Q, et al. Engineered Si@alginate microcapsule-graphite composite electrode for next generation high-performance lithium-ion batteries. *Electrochim Acta*. 2018;270:480-489. doi:10.1016/j.electacta.2018.03.039

7. Ribeiro De Souza L, Al-Tabbaa A. High throughput production of microcapsules using microfluidics for self-healing of cementitious materials. *Lab Chip*. 2021;21(23):4652-4659. doi:10.1039/d1lc00569c

8. Souza L, Al-Tabbaa A. Microfluidic fabrication of microcapsules tailored for self-healing in cementitious materials. *Constr Build Mater*. 2018;184:713-722. doi:10.1016/j.conbuildmat.2018.07.005

9. You X, Wang B, Xie S, et al. Microfluidic-assisted fabrication of monodisperse core–shell microcapsules for pressure-sensitive adhesive with enhanced performance. *Nanomaterials*. 2020;10(2). doi:10.3390/nano10020274

10. Rui X, Jiansong C, Shijiao Z, et al. Preparation of monodisperse ZrO2 ceramic microspheres (>200 μm) by co-axial capillary microfluidic device assisted internal gelation process. *Ceram Int*. 2019;45(16):19627-19634. doi:10.1016/j.ceramint.2019.06.210

11. Lee TY, Choi TM, Shim TS, Frijns RAM, Kim SH. Microfluidic production of multiple emulsions and functional microcapsules. *Lab Chip*. 2016;16(18):3415-3440. doi:10.1039/c6lc00809g

12. Vladisavljević GT, al Nuumani R, Nabavi SA. Microfluidic production of multiple emulsions. *Micromachines (Basel)*. 2017;8(3). doi:10.3390/mi8030075

13. Watanabe T, Sakai Y, Sugimori N, Ikeda T, Monzen M, Ono T. Microfluidic Production of Monodisperse Biopolymer Microcapsules for Latent Heat

Storage. *ACS Materials Au*. Published online 2021. doi:10.1021/acsmaterialsau.1c00068

14. Glomm WR, Molesworth PP, Yesiltas B, Jacobsen C, Johnsen H. Encapsulation of salmon oil using complex coacervation: Probing the effect of gum acacia on interfacial tension, coacervation and oxidative stability. *Food Hydrocoll*. 2023;140. doi:10.1016/j.foodhyd.2023.108598

15. Warner JT. *The Handbook of Lithium-Ion Battery Pack Design : Chemistry, Components, Types and Terminology*. *Elsevier*. 2015

16. Warner JT. *Lithium-Ion Battery Chemistries : A Primer*. *Elsevier*. 2019

17. Padhi AK, Nanjundaswamy K 5, Goodenough JB. *12. 5. Picart and E. Genies*. Vol 144. John Wiley & Sons, Inc; 1997.

18. Zubi G, Dufo-López R, Carvalho M, Pasaoglu G. The lithium-ion battery: State of the art and future perspectives. *Renewable and Sustainable Energy Reviews*. 2018;89:292-308. doi:10.1016/j.rser.2018.03.002

19. Warner JT. *The Handbook of Lithium-Ion Battery Pack Design*. *Elsevier*. 2015.

20. Golubkov AW, Fuchs D, Wagner J, et al. Thermal-runaway experiments on consumer Li-ion batteries with metal-oxide and olivin-type cathodes. *RSC Adv*. 2014;4(7):3633-3642. doi:10.1039/c3ra45748f

21. Love CT. Thermomechanical analysis and durability of commercial micro-porous polymer Li-ion battery separators. *J Power Sources*. 2011;196(5):2905-2912. doi:10.1016/j.jpowsour.2010.10.083

22. Schipper F, Aurbach D. A brief review: Past, present and future of lithium ion batteries. *Russian Journal of Electrochemistry*. 2016;52(12):1095-1121. doi:10.1134/S1023193516120120

23. Yu L, Zhang R, Jia R, et al. Consecutive engineering of anodic graphene supported cobalt monoxide composite and cathodic nanosized lithium cobalt oxide materials with improved lithium-ion storage performances. *J Colloid Interface Sci*. 2023;652:2017-2028. doi:10.1016/j.jcis.2023.09.025

24. Warner JT. *Lithium-Ion Battery Chemistries : A Primer*. Elsevier. 2018

25. Xie Q, Ma Y, Zhang X, Wang L, Yue G, Peng DL. ZnO/Ni/C composite hollow microspheres as anode materials for lithium ion batteries. *J Alloys Compd*. 2015;619:235-239. doi:10.1016/j.jallcom.2014.08.240

26. Liu J, Zhu M, Mu K, et al. Engineering a novel microcapsule of Cu9S5core and SnS2quantum dot/carbon nanotube shell as a Li-ion battery anode. *Chemical Communications*. 2021;57(98):13397-13400. doi:10.1039/d1cc05657c

27. Wu Y, Han T, Huang X, et al. A Ga-Sn liquid alloy-encapsulated self-healing microcapsule as high-performance Li-ion battery anode. *Journal of Electroanalytical Chemistry*. 2022;922. doi:10.1016/j.jelechem.2022.116789

28. Gross SJ, Hsieh MT, Mumm DR, Valdevit L, Mohraz A. Alleviating expansion-induced mechanical degradation in lithium-ion battery silicon anodes via morphological design. *Extreme Mech Lett*. 2022;54. doi:10.1016/j.eml.2022.101746

29. Deimede V, Elmasides C. Separators for Lithium-Ion Batteries: A Review on the Production Processes and Recent Developments. *Energy Technology*. 2015;3(5):453-468. doi:10.1002/ente.201402215

30. Zhao R, Zhang S, Liu J, Gu J. A review of thermal performance improving methods of lithium ion battery: Electrode modification and thermal management system. *J Power Sources*. 2015;299:557-577. doi:10.1016/j.jpowsour.2015.09.001

31. Yang M, Hou J. Membranes in lithium ion batterie. *Membranes (Basel)*. 2012;2(3):367-383. doi:10.3390/membranes2030367

32. Zheng J, Li X, Yu Y, Feng X, Zhao Y. Novel high phosphorus content phosphaphenanthrene-based efficient flame retardant additives for lithium-ion battery. *J Therm Anal Calorim*. 2014;117(1):319-324. doi:10.1007/s10973-014-3679-5

33. Aiello L, Hanzu I, Gstrein G, Ewert E, Ellersdorfer C, Sinz W. Analysis and investigation of thermal runaway propagation for a mechanically constrained lithium-ion pouch cell module. *Batteries*. 2021;7(3). doi:10.3390/batteries7030049

34. Balakrishnan PG, Ramesh R, Prem Kumar T. Safety mechanisms in lithium-ion batteries. *J Power Sources*. 2006;155(2):401-414. doi:10.1016/j.jpowsour.2005.12.002

35. Feng X, Ouyang M, Liu X, Lu L, Xia Y, He X. Thermal runaway mechanism of lithium ion battery for electric vehicles: A review. *Energy Storage Mater*. 2018;10:246-267. doi:10.1016/j.ensm.2017.05.013

36. Feng X, Zheng S, Ren D, et al. Investigating the thermal runaway mechanisms of lithium-ion batteries based on thermal analysis database. *Appl Energy*. 2019;246:53-64. doi:10.1016/j.apenergy.2019.04.009

37. Feng X, Ren D, He X, Ouyang M. Mitigating Thermal Runaway of Lithium-Ion Batteries. *Joule*. 2020;4(4):743-770. doi:10.1016/j.joule.2020.02.010

38. Ren D, Feng X, Liu L, et al. Investigating the relationship between internal short circuit and thermal runaway of lithium-ion batteries under thermal abuse condition. *Energy Storage Mater*. 2021;34:563-573. doi:10.1016/j.ensm.2020.10.020

39. Ren D, Hsu H, Li R, et al. A comparative investigation of aging effects on thermal runaway behavior of lithium-ion batteries. *eTransportation*. 2019;2. doi:10.1016/j.etran.2019.100034

40. Hou J, Wang L, Feng X, et al. Thermal Runaway of Lithium-Ion Batteries Employing Flame-Retardant Fluorinated Electrolytes. *Energy and Environmental Materials*. Published online January 1, 2021. doi:10.1002/eem2.12297

41. Balakrishnan PG, Ramesh R, Prem Kumar T. Safety mechanisms in lithium-ion batteries. *J Power Sources*. 2006;155(2):401-414. doi:10.1016/j.jpowsour.2005.12.002

42. Venugopal G. *Characterization of Thermal Cut-off Mechanisms in Prismatic Lithium-Ion Batteries*. *J Power Sources.* 2001:231-237

43. Balakrishnan PG, Ramesh R, Prem Kumar T. Safety mechanisms in lithium-ion batteries. *J Power Sources*. 2006;155(2):401-414. doi:10.1016/j.jpowsour.2005.12.002

44. Liu J, Song X, Zhou L, et al. Fluorinated phosphazene derivative – A promising electrolyte additive for high voltage lithium ion batteries: From electrochemical performance to corrosion mechanism. *Nano Energy*. 2018;46:404-414. doi:10.1016/j.nanoen.2018.02.029

45. See KW, Wang G, Zhang Y, et al. Critical review and functional safety of a battery management system for large-scale lithium-ion battery pack technologies. *Int J Coal Sci Technol*. 2022;9(1). doi:10.1007/s40789-022-00494-0

46. Dai H, Zhang X, Wei X, Sun Z, Wang J, Hu F. Cell-BMS validation with a hardware-in-the-loop simulation of lithium-ion battery cells for electric vehicles. *International Journal of Electrical Power and Energy Systems*. 2013;52(1):174-184. doi:10.1016/j.ijepes.2013.03.037

47. Wang W, Liao C, Liu L, et al. Comparable investigation of tervalent and pentavalent phosphorus based flame retardants on improving the safety and capacity of lithium-ion batteries. *J Power Sources*. 2019;420:143-151. doi:10.1016/j.jpowsour.2019.02.037

48. Jia H, Xu W. Nonflammable nonaqueous electrolytes for lithium batteries. *Curr Opin Electrochem*. 2021;30. doi:10.1016/j.coelec.2021.100781

49. Xiang HF, Jin QY, Chen CH, Ge XW, Guo S, Sun JH. Dimethyl methylphosphonate-based nonflammable electrolyte and high safety lithium-ion batteries. *J Power Sources*. 2007;174(1):335-341. doi:10.1016/j.jpowsour.2007.09.025

50. Dalavi S, Xu M, Ravdel B, Zhou L, Lucht BL. Nonflammable Electrolytes for Lithium-Ion Batteries Containing Dimethyl Methylphosphonate. *J Electrochem Soc*. 2010;157(10):A1113. doi:10.1149/1.3473828

51. Wu B, Pei F, Wu Y, et al. An electrochemically compatible and flame-retardant electrolyte additive for safe lithium ion batteries. *J Power Sources*. 2013;227:106-110. doi:10.1016/j.jpowsour.2012.11.018

52. Zhang S, Li S, Lu Y. Designing safer lithium-based batteries with nonflammable electrolytes: A review. *eScience*. 2021;1(2):163-177. doi:10.1016/j.esci.2021.12.003

53. Gu Y, Fang S, Yang L, Hirano SI. Tris(2,2,2-trifluoroethyl) Phosphate as a Cosolvent for a Nonflammable Electrolyte in Lithium-Ion Batteries. *ACS Appl Energy Mater*. 2021;4(5):4919-4927. doi:10.1021/acsaem.1c00503

54. Li X, Li W, Chen L, et al. Ethoxy (pentafluoro) cyclotriphosphazene (PFPN) as a multi-functional flame retardant electrolyte additive for lithium-ion batteries. *J Power Sources*. 2018;378:707-716. doi:10.1016/j.jpowsour.2017.12.085

55. Oh J, Lee HS, Kim MP, Lee YG, Hong SY, Kim KM. A trade-off-free fluorosulfate-based flame-retardant electrolyte additive for high-energy lithium batteries. *J Mater Chem A Mater*. Published online 2022. doi:10.1039/d2ta05854e

56. Shi Y, Noelle DJ, Wang M, et al. Role of Amines in Thermal-Runaway-Mitigating Lithium-Ion Battery. *ACS Appl Mater Interfaces*. 2016;8(45):30956-30963. doi:10.1021/acsami.6b10501

57. Xia L, Wang D, Yang H, Cao Y, Ai X. An electrolyte additive for thermal shutdown protection of Li-ion batteries. *Electrochem commun*. 2012;25(1):98-100. doi:10.1016/j.elecom.2012.09.038

58. Noelle DJ, Shi Y, Wang M, Le A V., Qiao Y. Aggressive electrolyte poisons and multifunctional fluids comprised of diols and diamines for emergency shutdown of lithium-ion batteries. *J Power Sources*. 2018;384:93-97. doi:10.1016/j.jpowsour.2018.02.068

59. Selva M, Caretto A, Noè M, Perosa A. Carbonate phosphonium salts as catalysts for the transesterification of dialkyl carbonates with diols. The competition between cyclic carbonates and linear dicarbonate products. *Org Biomol Chem*. 2014;12(24):4143-4155. doi:10.1039/c4ob00655k

60. Bah MG, Bilal HM, Wang J. Fabrication and application of complex microcapsules: A review. *Soft Matter*. 2020;16(3):570-590. doi:10.1039/c9sm01634a

61. Rule JD, Sottos NR, White SR. Effect of microcapsule size on the performance of self-healing polymers. *Polymer (Guildf)*. 2007;48(12):3520-3529. doi:10.1016/j.polymer.2007.04.008

62. Wang Y, Zhang L, Li T, et al. Zein coacervate as a new coating material for temperature-triggered microcapsule and fruit preservation. *Colloids Surf A Physicochem Eng Asp*. 2023;666:131255. doi:10.1016/j.colsurfa.2023.131255

63. Ganan-Calvo A Castro-Hernandez E, Flores-Mosquera, et al. Preparation of phase change microcapsules with high thermal storage and temperature sensitive for thermal management. *J Energy Storage.* 2023;64:1077003.doi.org/10.1016/j.est.2023.107003

64. Zhao B, Ni Y, Chen K, Lin Z, Jia Z, Qiu H. Double-shell lignin microcapsules were prepared by one - step method for fabric coatings with UV resistance and durable antibacterial activity. *Prog Org Coat*. 2023;179. doi:10.1016/j.porgcoat.2023.107518

65. Park S, Jo B. Novel surfactant-free microencapsulation of molten salt using TiO2 shell for high temperature thermal energy storage: Thermal performance and thermal reliability. *J Energy Storage*. 2023;63. doi:10.1016/j.est.2023.107016

66. Zhang D, Liu C, Yang Y, et al. Systematic investigation on preparation and characterization of silica shell microencapsulated phase change materials based on sodium silicate precursor. *Colloids Surf A Physicochem Eng Asp*. 2023;667. doi:10.1016/j.colsurfa.2023.131328

67. Berraquero-García C, Pérez-Gálvez R, Espejo-Carpio FJ, Guadix A, Guadix EM, García-Moreno PJ. Encapsulation of Bioactive Peptides by Spray-Drying and Electrospraying. *Foods*. 2023;12(10). doi:10.3390/foods12102005

68. Bakola 2018- Electrospray Encapsulation of Antithrombotic Drug into Poly (Llactic acid) Nanoparticles for Cardiovascular Applications

69. Shlyapnikov YM, Shlyapnikova EA, Morozov VN. Reversible and Irreversible Mechanical Damaging of Large Double-Stranded DNA upon Electrospraying. *Anal Chem*. 2016;88(14):7295-7301. doi:10.1021/acs.analchem.6b01642

70. Qin Y, Lu X, Que H, et al. Preparation and Characterization of Pendimethalin Microcapsules Based on Microfluidic Technology. *ACS Omega*. 2021;6(49):34160-34172. doi:10.1021/acsomega.1c05903

71. Dallinger D, Kappe CO. Why flow means green – Evaluating the merits of continuous processing in the context of sustainability. *Curr Opin Green Sustain Chem*. 2017;7:6-12. doi:10.1016/j.cogsc.2017.06.003

72. Canan-Calvo AM, Castro-Hernandez E, Flores-Mosquera Banderas L. Massive, Generic, and Controlled Microencapsulation by Flow Focusing: Some Physicochemical Aspects and New Applications. *J. Flow*. 2015;5:48-54

73. Dallinger D, Gutmann B, Kappe CO. The Concept of Chemical Generators: On-Site On-Demand Production of Hazardous Reagents in Continuous Flow. *Acc Chem Res*. 2020;53(7):1330-1341. doi:10.1021/acs.accounts.0c00199

74. Bae J. Fabrication of carbon microcapsules containing silicon nanoparticlescarbon nanotubes nanocomposite by solgel method for anode in lithium ion battery. *J Solid State Chem*. 2011;184(7):1749-1755. doi:10.1016/j.jssc.2011.05.012

75. Xu D, Chen W, Fan X. Experimental investigation of particle size effect on the self-healing performance of microcapsule for cemented coral sand. *Constr Build Mater*. 2020;256. doi:10.1016/j.conbuildmat.2020.119343

76. Gobert SRL, Segers M, Luca S, et al. Development of a continuous reactor for emulsion-based microencapsulation of hexyl acetate with a polyuria shell. *J Microencapsul*. 2019;36(4):371-384. doi:10.1080/02652048.2019.1633433

77. Polenz I, Weitz DA, Baret JC. Polyurea microcapsules in microfluidics: Surfactant control of soft membranes. *Langmuir*. 2015;31(3):1127-1134. doi:10.1021/la5040189

78. Polenz I, Datta SS, Weitz DA. Controlling the morphology of polyurea microcapsules using microfluidics. *Langmuir*. 2014;30(44):13405-13410. doi:10.1021/la503234z

79. Yim T, Park MS, Woo SG, et al. Self-Extinguishing Lithium Ion Batteries Based on Internally Embedded Fire-Extinguishing Microcapsules with Temperature-Responsiveness. *Nano Lett*. 2015;15(8):5059-5067. doi:10.1021/acs.nanolett.5b01167

80. Lou P, Zhang W, Han Q, et al. Fabrication of fire-response functional separators with microcapsule fire extinguishing agent for lithium-ion battery safety. *Nano Select*. 2022;3(5):947-955. doi:10.1002/nano.202100274

81. Baginska M, Sottos NR, White SR. Core-Shell Microcapsules Containing Flame Retardant Tris(2-chloroethyl phosphate) for Lithium-Ion Battery Applications. *ACS Omega*. 2018;3(2):1609-1613. doi:10.1021/acsomega.7b01950

82. Xu Z, Chen W, Wu T, Wang C, Liang Z. Thermal management system study of flame retardant solid–solid phase change material battery. *Surfaces and Interfaces*. 2023;36. doi:10.1016/j.surfin.2022.102558

83. Ma TK, Yang YM, Jiang JJ, Yang M, Jiang JC. Synergistic Flame Retardancy of Microcapsules Based on Ammonium Polyphosphate and Aluminum Hydroxide for Lithium-Ion Batteries. *ACS Omega*. 2021;6(33):21227-21234. doi:10.1021/acsomega.1c00598

84. Liu Z, Peng Y, Meng T, Yu L, Wang S, Hu X. Thermal-triggered fire-extinguishing separators by phase change materials for high-safety lithium-ion

batteries. *Energy Storage Mater*. 2022;47:445-452. doi:10.1016/j.ensm.2022.02.020

85. Watanabe S, Kinoshita M, Hosokawa T, Morigaki K, Nakura K. Capacity fading of LiAlyNi1-x-yCoxO 2 cathode for lithium-ion batteries during accelerated calendar and cycle life tests (effect of depth of discharge in charge-discharge cycling on the suppression of the micro-crack generation of LiAlyNi 1-x-yCoxO2 particle). *J Power Sources*. 2014;260:50-56. doi:10.1016/j.jpowsour.2014.02.103

86. Eleri OE, Huld F, Pires J, et al. Revealing mechanisms of activated carbon capacity fade in lithium-ion capacitors. *Electrochim Acta*. 2023;453:142359. doi:10.1016/J.ELECTACTA.2023.142359

87. Yu P, Ritter JA, White RE, Popov BN. *Ni-Composite Microencapsulated Graphite as the Negative Electrode in Lithium-Ion Batteries I. Initial Irreversible Capacity Study*. Vol 147.; 2000.

88. Han T, Wu Y, Ding Y, Zhong Y, Zhou P, Liu J. Encapsulating Tin Nanoflowers into Microcapsules for High-Rate-Performance Secondary Battery Anodes through In Situ Polymerizing Oil-in-Water Interface. *Energy Technology*. 2020;8(5). doi:10.1002/ente.201901404

89. Wu W, Wei Y, Chen H, et al. In-situ encapsulation of α-Fe2O3 nanoparticles into ZnFe2O4 micro-sized capsules as high-performance lithium-ion battery anodes. *J Mater Sci Technol*. 2021;75:110-117. doi:10.1016/j.jmst.2020.10.039

90. Zhao H, Gao Y, Wang J, et al. Egg yolk-derived phosphorus and nitrogen dual doped nano carbon capsules for high-performance lithium ion batteries. *Mater Lett*. 2016;167:93-97. doi:10.1016/j.matlet.2015.12.147

91. Yang J, Wang YX, Chou SL, et al. Yolk-shell silicon-mesoporous carbon anode with compact solid electrolyte interphase film for superior lithium-ion batteries. *Nano Energy*. 2015;18:133-142. doi:10.1016/j.nanoen.2015.09.016

92. Wang K, Pei S, He Z, et al. Synthesis of a novel porous silicon microsphere@carbon core-shell composite via in situ MOF coating for lithium ion battery anodes. *Chemical Engineering Journal*. 2019;356:272-281. doi:10.1016/j.cej.2018.09.027

93. Yu H, Gu F, Chen S, Du Y, Wang L, Song Y. A N-doped carbon nanocages@silicon nanoparticles microcapsules for high-performance Li-storage. *Compos B Eng*. 2022;247. doi:10.1016/j.compositesb.2022.110334

94. Jones PK, Stimming U, Lee AA. Impedance-based forecasting of lithium-ion battery performance amid uneven usage. *Nat Commun*. 2022;13(1). doi:10.1038/s41467-022-32422-w

95. Ovejas VJ, Cuadras A. Impedance characterization of an LCO-NMC/graphite cell: Ohmic conduction, sei transport and charge-transfer phenomenon. *Batteries*. 2018;4(3). doi:10.3390/batteries4030043

96. Barsoukov E, Macdonald Impedance Spectroscopy. *Front Matter. In: Wiley*; 2018. doi:10.1002/9781119381860.fmatter

97. Shi Y, Noelle DJ, Wang M, et al. Exothermic behaviors of mechanically abused lithium-ion batteries with dibenzylamine. *J Power Sources*. 2016;326:514-521. doi:10.1016/j.jpowsour.2016.07.034

98. Shi Y, Noelle DJ, Wang M, et al. Role of Amines in Thermal-Runaway-Mitigating Lithium-Ion Battery. *ACS Appl Mater Interfaces*. 2016;8(45):30956-30963. doi:10.1021/acsami.6b10501

99. Jégat C, Taverdet JL. *Stirring Speed Influence Study on the Microencapsulation Process and on the Drug Release from Microcapsules*. Vol 44.; 2000.

100. Beglarigale A, Eyice D, Seki Y, Yalçınkaya Ç, Çopuroğlu O, Yazıcı H. Sodium silicate/polyurethane microcapsules synthesized for enhancing self-healing ability of cementitious materials: Optimization of stirring speeds and evaluation of self-healing efficiency. *Journal of Building Engineering*. 2021;39. doi:10.1016/j.jobe.2021.102279

101. Carrara AE, Rodrigues VHDS, Dutra R de CL, Dutra JCN. Impact assessment of synthesis parameter stirring speed in final physicochemical properties of PU microcapsules incorporated into epoxy matrixes. *An Acad Bras Cienc*. 2023;95(2). doi:10.1590/0001-3765202320201518

102. Teeka P, Chaiyasat A, Chaiyasat P. Preparation of poly (methyl methacrylate) microcapsule with encapsulated jasmine oil. In: *Energy Procedia*. Vol 56. Elsevier Ltd; 2014:181-186. doi:10.1016/j.egypro.2014.07.147

103. Wilkie CA. *TGA/FTIR: An Extremely Useful Technique for Studying Polymer Degradation*. *Poly Degradation and Stability.* 1999. 66:301-306

104. Liu Z, Peng Y, Meng T, Yu L, Wang S, Hu X. Thermal-triggered fire-extinguishing separators by phase change materials for high-safety lithium-ion batteries. *Energy Storage Mater*. 2022;47:445-452. doi:10.1016/j.ensm.2022.02.020

105. Feng C, Chen Y, Liu D, Zhang P. Conductivity and electrochemical performance of LiFePO4 slurry in the lithium slurry battery. In: *IOP Conference Series: Materials Science and Engineering*. Vol 207. Institute of Physics Publishing; 2017. doi:10.1088/1757-899X/207/1/012076

106. Lung-Hao Hu B, Wu FY, Lin C Te, Khlobystov AN, Li LJ. Graphene-modified LiFePO4 cathode for lithium ion battery beyond theoretical capacity. *Nat Commun*. 2013;4. doi:10.1038/ncomms2705

107. Xu B, Diao W, Wen G, Choe SY, Kim J, Pecht M. Decoupling the thermal and non-thermal effects of discharge C-rate on the capacity fade of lithium-ion batteries. *J Power Sources*. 2021;510. doi:10.1016/j.jpowsour.2021.230390

108. Saxena S, Xing Y, Kwon D, Pecht M. Accelerated degradation model for C-rate loading of lithium-ion batteries. *International Journal of Electrical Power and Energy Systems*. 2019;107:438-445. doi:10.1016/j.ijepes.2018.12.016

109. Marin-Montin J, Zurita-Gotor M, Montero-Chacón F. Numerical Analysis of Degradation and Capacity Loss in Graphite Active Particles of Li-Ion Battery Anodes. *Materials*. 2022;15(11). doi:10.3390/ma15113979

110. Liu XM, Arnold CB. Effects of Cycling Ranges on Stress and Capacity Fade in Lithium-Ion Pouch Cells. *J Electrochem Soc*. 2016;163(13):A2501-A2507. doi:10.1149/2.1131610jes